Jül-4343

Institut für Kernphysik (IKP)

# Ion Trapping in the High-Energy Storage Ring HESR

*Frank Hinterberger*

*Helmholtz-Institut für Strahlen- und Kernphysik, University of Bonn, Germany*

Mitglied der Helmholtz-Gemeinschaft

JÜLICH
FORSCHUNGSZENTRUM

# Ion Trapping in the High-Energy Storage Ring HESR

*Frank Hinterberger*

*Helmholtz-Institut für Strahlen- und Kernphysik, University of Bonn, Germany*

Berichte des Forschungszentrums Jülich; 4343
ISSN 0944-2952
Institut für Kernphysik (IKP)
Jül-4343

Vollständig frei verfügbar im Internet auf dem Jülicher Open Access Server (JUWEL)
unter http://www.fz-juelich.de/zb/juwel

Zu beziehen durch: Forschungszentrum Jülich GmbH · Zentralbibliothek, Verlag
D-52425 Jülich · Bundesrepublik Deutschland
☎ 02461 61-5220 · Telefax: 02461 61-6103 · e-mail: zb-publikation@fz-juelich.de

# Ion Trapping in the High-Energy Storage Ring HESR

*Frank Hinterberger*
Helmholtz-Institut für Strahlen- und Kernphysik, University of Bonn, Germany

**Abstract**
The problem of ion trapping in the high-energy storage ring HESR is studied in the present report. Positive ions are trapped in the negative potential well of the antiproton beam. The ions are produced by the interaction between the antiproton beam and the residual gas. The adverse effects of ion trapping like tune shifts, tune spreads and coherent instabilities are reviewed. The ion production rate by ionization of the residual gas molecules is estimated. The negative potential well and the corresponding electric fields of the antiproton beam are evaluated in order to study the transverse and longitudinal motion of the ions and the accumulation in trapping pockets. The removal of ions can be achieved using clearing electrodes and under certain conditions resonant transverse beam shaking. Diagnostic tools and measurements of trapped ion effects are sketched.

**Contents**

## 1. Introduction

The High-Energy Storage Ring (HESR) of the future International Facility for Antiprotons and Ion Research (FAIR) at GSI in Darmstadt is designed as synchrotron and storage ring for antiprotons in the momentum range 1.5 – 15 GeV/c [1, 2]. Internal target experiments with antiprotons are planned by the PANDA collaboration [3]. In addition, two other collaborations (PAX [4, 5], ASSIA [6]) proposed spin physics experiments with polarized antiprotons. In the present work the problem of ion trapping by the antiproton beam is studied. In this context we mention that estimates of trapped ion effects were made in two previous reports [7, 8].

The effects of trapped ions and trapped electrons have been observed in many accelerators and storage rings [9, 10, 11, 12, 13, 14, 15, 16, 17, 18, 19, 20]. The beam particles interact with the molecules of the residual gas in the vacuum and produce positive ions and electrons. Electrons are trapped in positive particle beams while ions are trapped in negative particle beams. The trapped particles can cause emittance growth, instability and beam loss. The CERN Antiproton Accumulator (AA), the Fermilab Accumulator and the Fermilab Recycler Ring (RR) have observed the adverse effects of trapped ions, and have used various methods in order to remove the ions.

In the present report we evaluate the trapped ion effects which are caused by the circulating antiproton beam. The special effects due to the electron beam of the electron cooler (EC) are discussed in Sect. 14..

## 2. Beam Parameters and HESR Lattice

The layout of the HESR ring is shown in Fig. 1. In Fig. 2, the lattice functions $\beta_x$, $\beta_y$ and the horizontal dispersion $D_x$ of the standard HESR optics 'optic4' with $\gamma_{tr} = 6.2$, $Q_x = 7.5995$ and $Q_y = 7.6216$ are shown as a function of $s$ with $s = 0$ at the beginning of the upper arc. The beta functions amount to about 175 m in the region of the electron cooler and about 2 m in the region of the PANDA target. In Figs. 3 and 4, the beam envelopes, i.e. the 1-sigma values $\sigma_x$ and $\sigma_y$, are plotted as a function of $s$ for $1.0 \cdot 10^{11}$ antiprotons at 15 GeV/c.

For the calculation of the negative potential well of the antiproton beam we need the beam envelopes $\sigma_x$ and $\sigma_y$ as a function of $s$. We perform the calculations using the standard optics 'optic4' and the HESR List of beam parameters from July 2011 [21]. We calculate the envelopes assuming stochastic cooling. The effective target density of the PANDA target will be $4.0 \cdot 10^{15}$ hydrogen atoms per cm$^2$. The stochastic cooling will be adjusted such that the transverse emittance growth by the beam-target interactions is compensated and the highest-possible momentum resolution is achieved. Therefore, the transverse rms emittances stay constant and we can assume normalized rms emittances $\epsilon_x$ and $\epsilon_y$ as given by the RESR beam at HESR injection. The longitudinal emittance is characterized by a long bunch of constant length $L_1 = 0.9C$ and the relative rms momentum spread $\delta$. The rms values of $\delta$ which can be achieved with stochastic cooling are taken for the calculation of the envelopes. They are listed below. The corresponding momentum spreads are lesser than the momentum spreads at injection.

We assume the geometric rms emittances without cooling as given by the RESR beam at HESR injection. The kinetic energy at injection amounts to 3.0 GeV, the corresponding beam momentum is 3.825 GeV/c and $\beta\gamma = 4.077$. The normalized geometric rms emittances[1] $\epsilon_{x,y}^{normalized}$ amount to 1.0 mm mrad for $3.5 \cdot 10^{10}$ antiprotons in the ring. They scale as $(N_{\bar{p}}/3.5 \cdot 10^{10})^{4/5}$ with the number $N_{\bar{p}}$ of antiprotons. The relative rms momentum spread scales as

[1] $\epsilon_{x,y}^{normalized} = \epsilon_{x,y}\beta\gamma$

$(N_{\bar{p}}/3.5 \cdot 10^{10})^{2/5}$. Taking as reference values the emittances $\epsilon_3$ and relative beam spreads $\delta_3$ at injection energy $T_{\bar{p}} = 3.0$ GeV one has

- $N_{\bar{p}} = 1.0 \cdot 10^{11}$: $\epsilon_3 = 0.58$ mm mrad, $\delta_3 = 0.50 \cdot 10^{-3}$,
- $N_{\bar{p}} = 1.0 \cdot 10^{10}$: $\epsilon_3 = 0.090$ mm mrad $\delta_3 = 0.20 \cdot 10^{-3}$.

Accelerating or decelerating the injected beam yields geometric rms emittances $\epsilon = \epsilon_x = \epsilon_y$ and relative rms momentum spreads $\delta$ which scale according to the adiabatic damping law,

$$\begin{aligned} \epsilon &= \epsilon_3 \frac{\beta_3 \gamma_3}{\beta \gamma} \\ \delta &= \delta_3 \frac{\beta_3 \gamma_3}{\beta \gamma} \end{aligned} \tag{1}$$

As mentioned, these values are kept constant by stochastic cooling during the measurements with the PANDA target.

At the beginning, the HESR will be operated with the collector ring (CR) as injector. Then, the start rms emittance at 3 GeV will be $\epsilon_3 = 1.25$ mm mrad and the relative rms momentum spread $\delta_3 = 0.25 \cdot 10^{-3}$. We assume the barrier bucket mode of operation with a bunch length $L_1 = 0.9C$ and a beam free gap of length $L_2 = 0.1C$. The circumference $C$ amounts to 575.2 m.

Assuming Gaussian beam distributions the envelopes are represented by the one standard deviations $\sigma_x(s)$ and $\sigma_y(s)$,

$$\begin{aligned} \sigma_x &= \sqrt{\epsilon_x \beta_x + (D_x \delta)^2} \\ \sigma_y &= \sqrt{\epsilon_y \beta_y}. \end{aligned} \tag{2}$$

Here, $\epsilon_x$ and $\epsilon_y$ represent the geometrical rms emittances, $\beta_x$ and $\beta_y$ the horizontal and vertical beta-functions, $\delta$ the rms width of the relative momentum deviation and $D_x$ is the horizontal dispersion. The momentum range of the HESR ring is between 1.5 GeV/c and 15 GeV/c. Usually, four standard momenta are considered. Here, we list the beam parameters $\epsilon$ and $\delta$ which are used for the calculation of the envelopes assuming $10^{11}$ antiprotons in the HESR ring,

1. S1: $p = 1.5$ GeV/c, $T = 0.831$ GeV, $\epsilon = 1.48$ mm mrad, $\delta = 1.9 \cdot 10^{-4}$,
2. S2: $p = 3.825$ GeV/c, $T = 3.0$ GeV, $\epsilon = 0.58$ mm mrad, $\delta = 1.4 \cdot 10^{-4}$,
3. S3: $p = 8.889$ GeV/c, $T = 8.0$ GeV, $\epsilon = 0.28$ mm mrad, $\delta = 1.2 \cdot 10^{-4}$,
4. S4: $p = 15$ GeV/c, $T = 14.091$ GeV. $\epsilon = 0.148$ mm mrad, $\delta = 0.9 \cdot 10^{-4}$.

The corresponding list for $10^{10}$ antiprotons reads

1. S1: $p = 1.5$ GeV/c, $T = 0.831$ GeV, $\epsilon = 0.23$ mm mrad, $\delta = 1.1 \cdot 10^{-4}$,
2. S2: $p = 3.825$ GeV/c, $T = 3.0$ GeV, $\epsilon = 0.089$ mm mrad, $\delta = 5.1 \cdot 10^{-5}$,
3. S3: $p = 8.889$ GeV/c, $T = 8.0$ GeV, $\epsilon = 0.043$ mm mrad, $\delta = 5.4 \cdot 10^{-5}$,
4. S4: $p = 15$ GeV/c, $T = 14.091$ GeV. $\epsilon = 0.023$ mm mrad, $\delta = 3.9 \cdot 10^{-5}$.

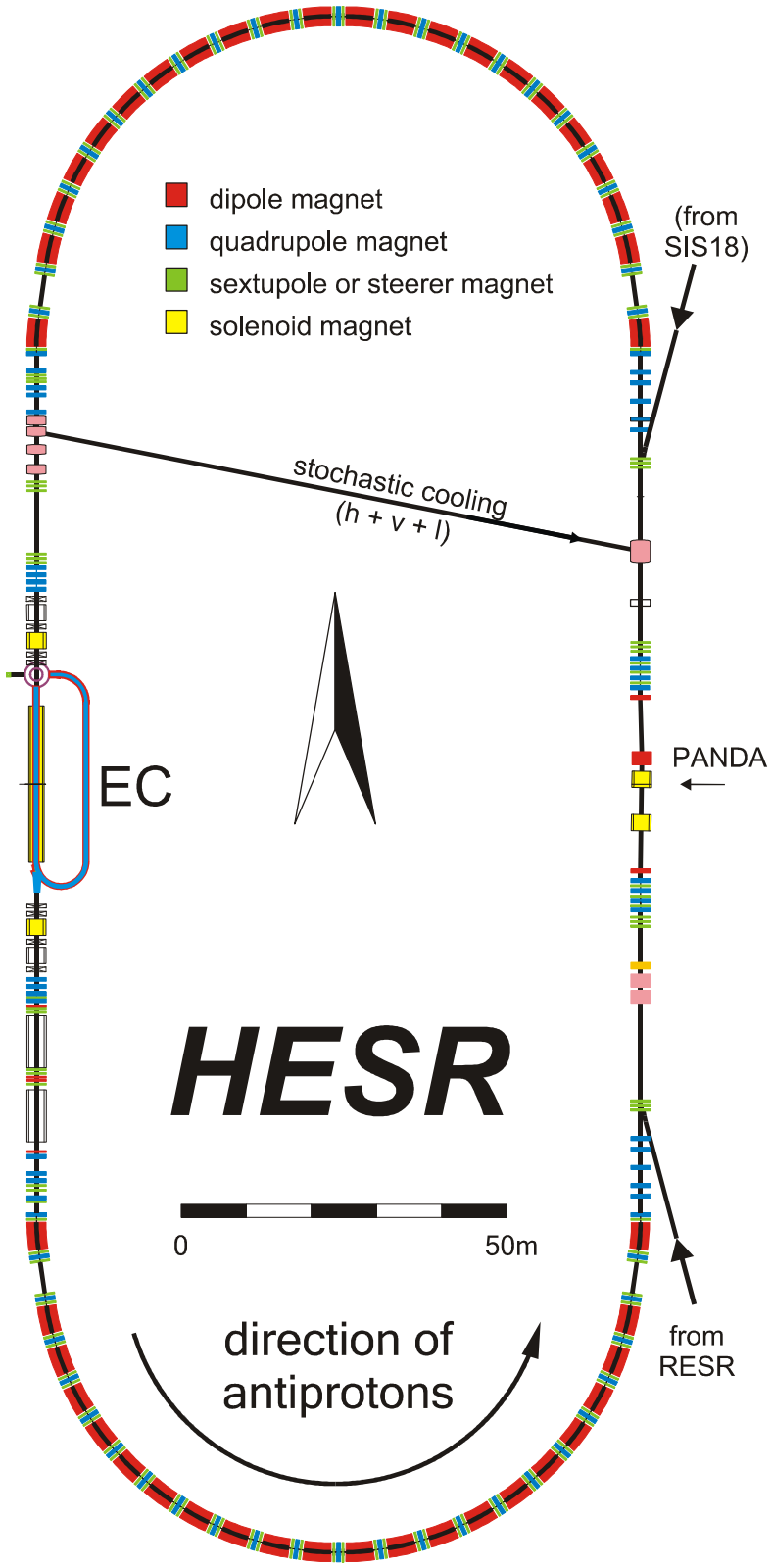


Fig. 1: Layout of the HESR ring.

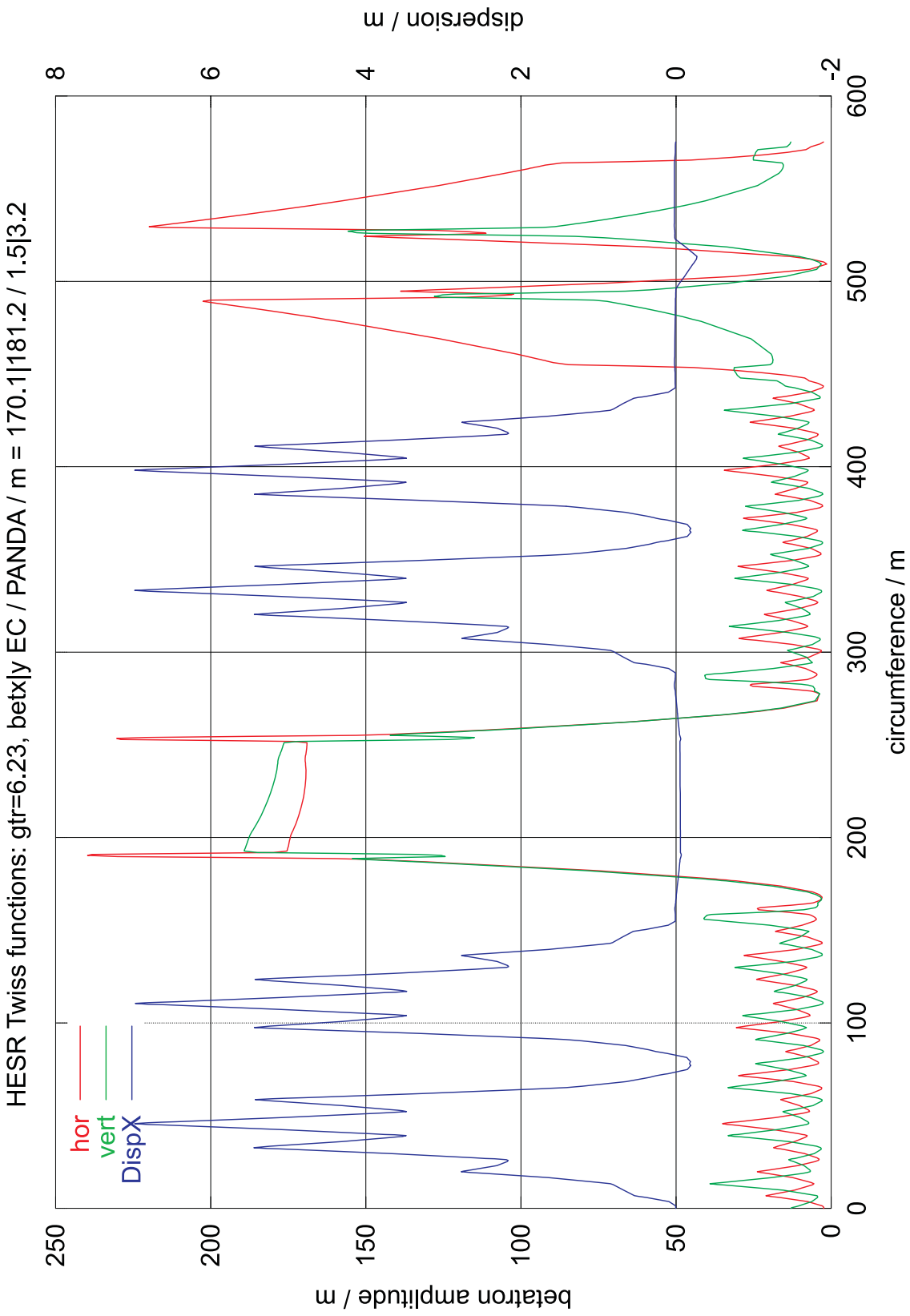


Fig. 2: The lattice functions $\beta_x$, $\beta_y$ and the dispersion $D_x$ of the standard HESR optics with $\gamma_{tr} = 6.2$.

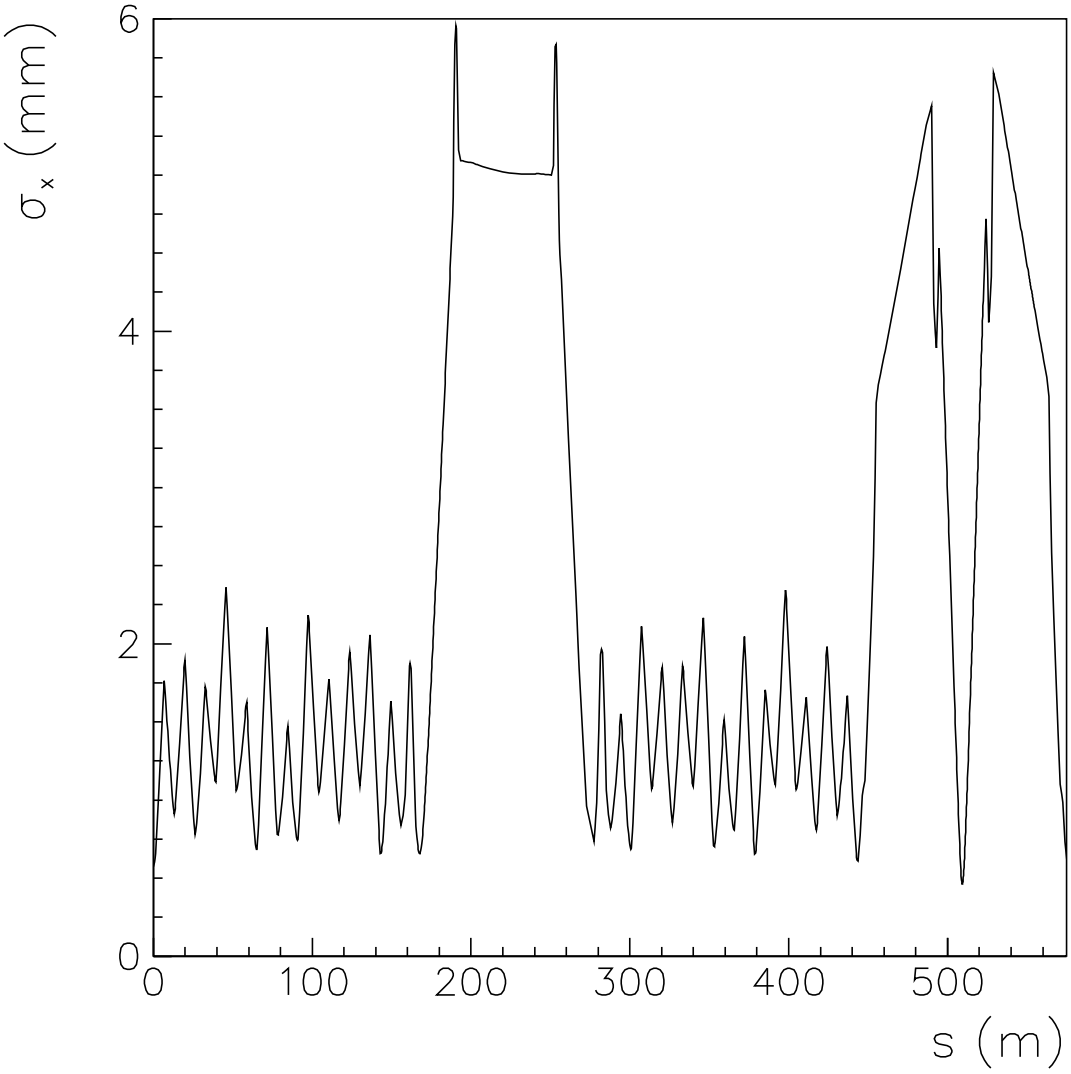


Fig. 3: Horizontal beam envelope $\sigma_x(s)$ for $1.0 \cdot 10^{11}$ antiprotons at 15 GeV/c. The electron cooler is located between $s = 207.390$ m and $s = 231.890$ m. The PANDA target is located at $s = 509.481$ m.

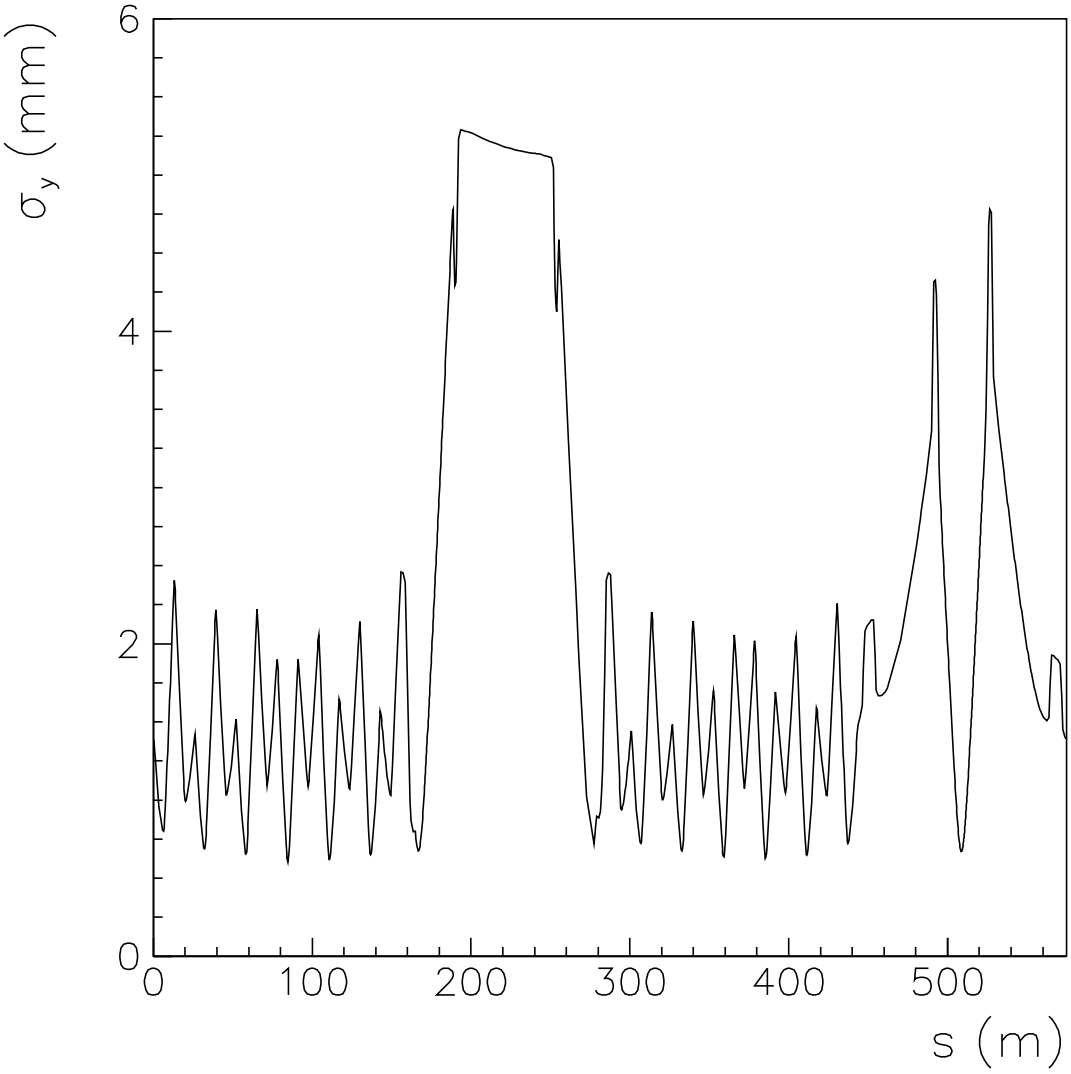


Fig. 4: Vertical beam envelope $\sigma_y(s)$ for $1.0 \cdot 10^{11}$ antiprotons at 15 GeV/c. The electron cooler is located between $s = 207.390$ m and $s = 231.890$ m. The PANDA target is located at $s = 509.481$ m.

## 3. Electric Field and Potential Well of the Antiproton Beam

### 3.1 Electric potential well

The potential well of the antiproton beam can be calculated for various particle distributions and beam pipe profiles. The simplest case is to assume a round beam pipe of radius $r_c$ and a round beam of constant density within the radius $a$. The linear charge density $\lambda$ is

$$\lambda = -\frac{N_{\bar{p}} e}{L_1}. \tag{3}$$

Here, $N_{\bar{p}}$ is the number of stored antiprotons, $e$ the elementary charge and $L_1$ the length of the barrier bucket bunches, e.g. $L_1 = 0.9C$. The potential $U(r)$, with the constraint $U(r_c) = 0$ at the surface of the beam pipe, is given by

$$\begin{aligned} U(r) &= \frac{\lambda}{2\pi\epsilon_0} \ln \frac{r_c}{r} \quad r \geq a, \\ U(r) &= \frac{\lambda}{2\pi\epsilon_0} \left[ \frac{1}{2} - \frac{r^2}{2a^2} + \ln\left(\frac{r_c}{a}\right) \right] \quad r \leq a. \end{aligned} \tag{4}$$

We note that $\lambda/(2\pi\epsilon_0) = -0.556$ V for $1.0 \cdot 10^{11}$ antiprotons in the ring. The corresponding electric field $E_r$ reads

$$\begin{aligned} E_r(r) &= \frac{\lambda}{2\pi\epsilon_0} \frac{1}{r} \quad r \geq a, \\ E_r(r) &= \frac{\lambda}{2\pi\epsilon_0} \frac{r}{a^2} \quad r \leq a. \end{aligned} \tag{5}$$

Note the minus sign in the definition of the linear charge density! Therefore, the potential $U(r)$ is negative and the electric field $E_r$ is directed to the beam center. The absolute value of the beam potential is maximal at the beam center $r = 0$,

$$U(0) = \frac{\lambda}{2\pi\epsilon_0} \left[ \frac{1}{2} + \ln\left(\frac{r_c}{a}\right) \right]. \tag{6}$$

Thus, the local depth of the beam potential depends on the ratio of the beam pipe radius $r_c$ and the beam radius $a$. The absolute value of the electric field is maximal at the beam edge $r = a$,

$$E_r(a) = \frac{\lambda}{2\pi\epsilon_0} \frac{1}{a}. \tag{7}$$

For a bi-Gaussian distribution of the beam particles with the rms values $\sigma_x$ and $\sigma_y$ and a round beam pipe with inner radius $r_c$, the potential U(x,y) can be calculated using the equations in the appendix of Zhou's PhD thesis [16]. We are only interested in the values $U(s)$ at the beam center $(x, y, s) = (0, 0, s)$ which can be calculated using

$$U(s) = U(0,0,s) = \frac{\lambda}{4\pi\epsilon_0} \left[ \gamma + \ln\left( \frac{2\, r_c^2}{(\sigma_x + \sigma_y)^2} \right) \right], \tag{8}$$

where $\gamma \approx 0.577$ is Euler's constant. The profile[2] of the beam pipe radius $r_c$ is shown in Fig. 5. The resulting values shown in Fig. 6 are calculated assuming the standard optics, $p_{\bar{p}} = 15$ GeV/c

[2] If the electron cooler is installed the radius $r_c$ amounts to 100 mm in the region of the electron cooler. The resulting modifications are discussed in Sect. 14..

and $N_{\bar{p}} = 1.0 \cdot 10^{11}$ and a continuous inner beam pipe radius of 44.5 mm outside of the PANDA target region (see Fig. 5). The potential distribution has minima at positions where the beam has sharp waists (more precisely where the ratio $r_c/(\sigma_x + \sigma_y)$ has a local maximum). The positive ions are accelerated in the longitudinal direction towards those potential minima which act as trapping pockets. These are the ideal locations for the clearing electrodes.

The magnitude of the potential $U(x, y, s)$ and the potential depth $U(s)$ depend strongly on the number $N_{\bar{p}}$ of stored antiprotons. Since $\lambda \propto N_{\bar{p}}$ we get $U(s) \propto N_{\bar{p}}$ if the dependence of $(\sigma_x + \sigma_y)$ on $N_{\bar{p}}$ in the logarithmic term in Eq. (8) is ignored. Thus for $N_{\bar{p}} = 1.0 \cdot 10^{10}$, the potential depth $U(s)$ is a factor of ten lesser. Taking the dependence of $(\sigma_x + \sigma_y)$ on $N_{\bar{p}}$ ($\sigma_{x,y} \propto N_{\bar{p}}^{2/5}$, see Sect. 2.) in the logarithmic term into account yields a reduction factor of about eight.

### 3.2 Transverse electric field components $E_x$ and $E_y$

The transverse electric field near the beam center, which is needed in order to estimate the oscillation frequency of the trapped ions, can be calculated using the following linear approximation

$$\begin{aligned} E_x(x, y) &= \frac{\lambda}{2\pi\epsilon_0} \frac{1}{(\sigma_x + \sigma_y)} \frac{x}{\sigma_x}, \\ E_y(x, y) &= \frac{\lambda}{2\pi\epsilon_0} \frac{1}{(\sigma_x + \sigma_y)} \frac{y}{\sigma_y}. \end{aligned} \tag{9}$$

The absolute value of the transverse electric field is maximal on the short axis of the elliptical beam distribution. For instance if $\sigma_y < \sigma_x$, the maximum is near $y = 1.6\sigma_y$ and can be calculated using the equation (2.6) in Zhou's thesis [16]. The electric fields of the clearing electrodes should be essentially larger than the maximum values of the transverse electric field in order to extract the positive ions out of the beam. Therefore we calculate a safe upper limit $E_{max}$ of the transverse electric field distribution using the following simple formula

$$E_{max} = \frac{|\lambda|}{2\pi\epsilon_0} \frac{1}{\sqrt{2}\sqrt{\sigma_x^2 + \sigma_y^2}}. \tag{10}$$

This equation holds true for the maximal transverse electric field component $|E_{y,max}|$ if $\sigma_y < \sigma_x$ and for the maximal transverse electric field component $|E_{x,max}|$ if $\sigma_x < \sigma_y$. The resulting values $E_{max}$ shown in Fig. 7 are calculated assuming the standard optics, $p_{\bar{p}} = 15$ GeV/c and $N_{\bar{p}} = 1.0 \cdot 10^{11}$. If positive ions are trapped within the negative antiproton beam the potentials and the electric fields are reduced by the factor $(1 - \eta)$ where $\eta$ is the neutralization factor.

If the electron cooler is installed the effects of the electron beam have to be taken into account. The resulting modifications are discussed in Sect. 14..

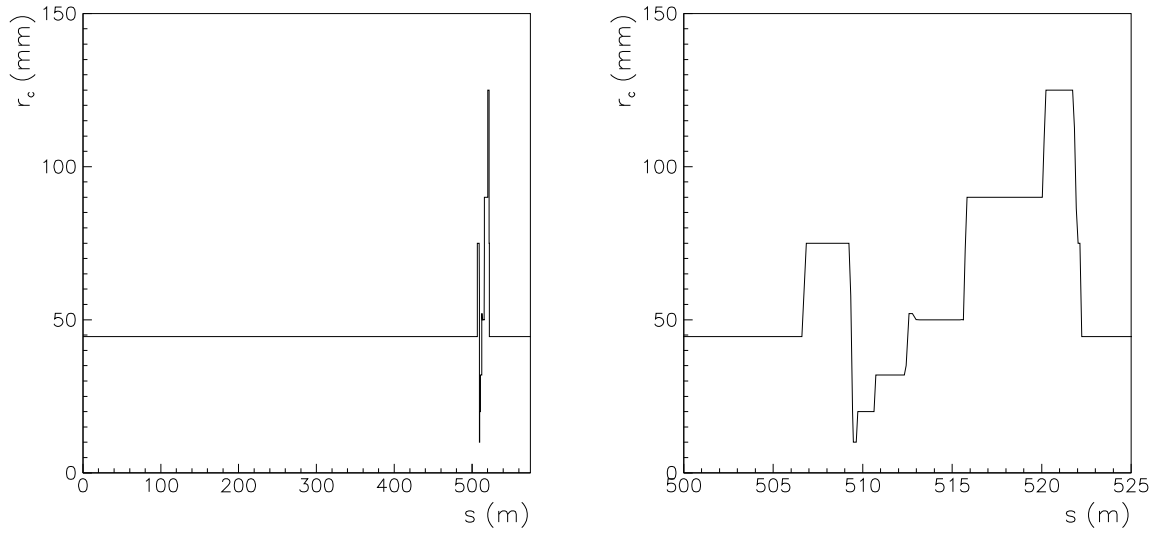


Fig. 5: Inner beam pipe radius $r_c(s)$ (without electron cooler). Left: the complete HESR ring from $s = 0$ m to $s = 575$ m. Right: the PANDA target region from $s = 500$ m to $s = 525$ m. The PANDA target is located at $s = 509.481$ m.

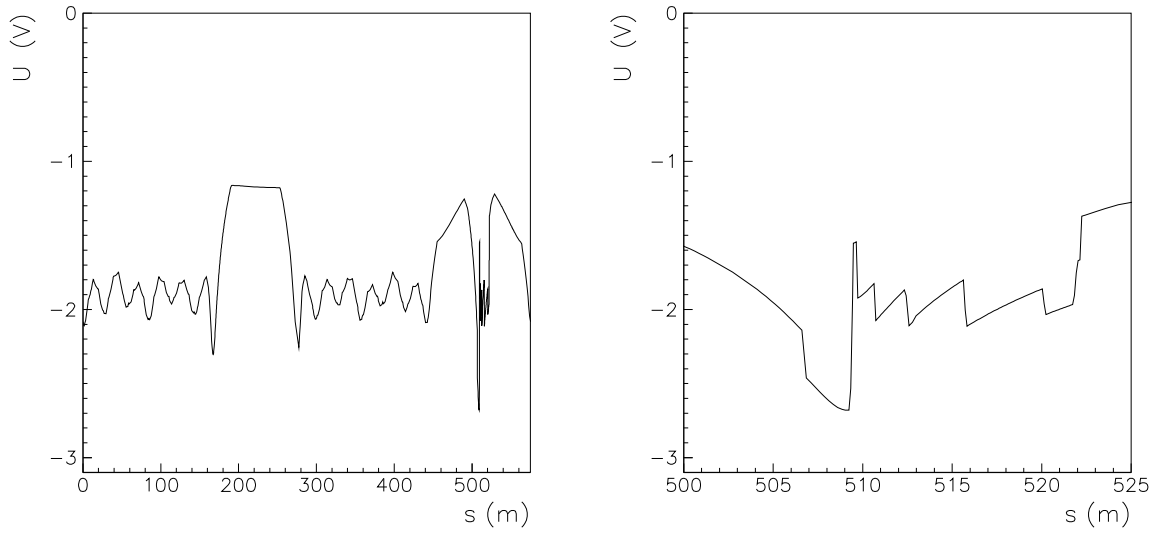


Fig. 6: Central beam potential $U(s)$ assuming the standard optics, $L_1 = 0.9C$, $p_{\bar{p}} = 15$ GeV/c, $N_{\bar{p}} = 1.0 \cdot 10^{11}$ and $\eta = 0$. Left: the complete HESR ring from $s = 0$ m to $s = 575$ m. Right: the PANDA target region from $s = 500$ m to $s = 525$ m.

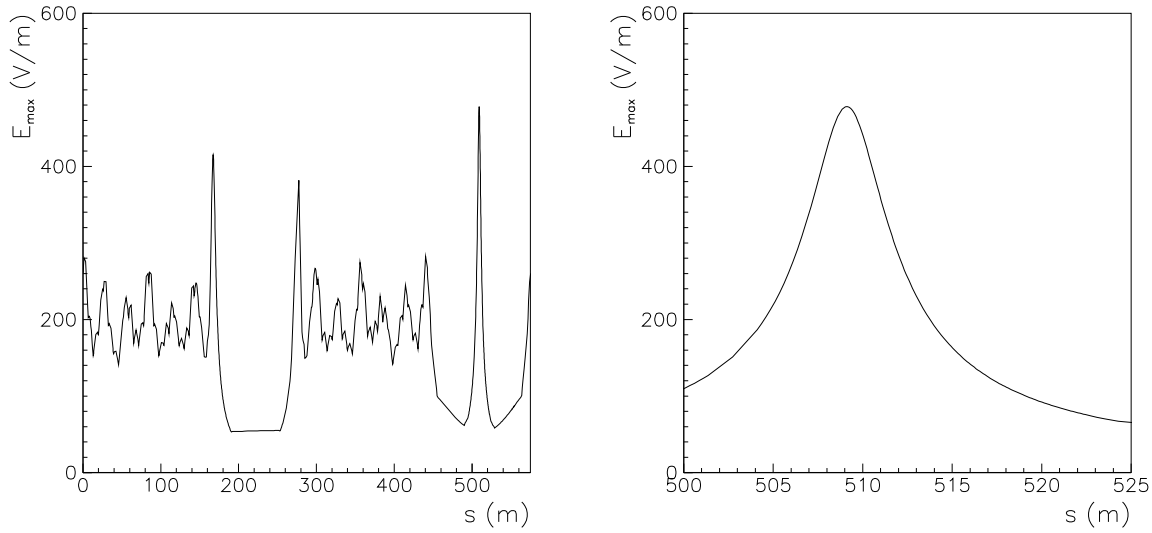


Fig. 7: Upper limit $E_{max}$ of the transverse electric field distribution of the antiproton beam assuming the standard optics, $L_1 = 0.9C$, $p_{\bar{p}} = 15$ GeV/c, $N_{\bar{p}} = 1.0 \cdot 10^{11}$ and $\eta = 0$. Left: the complete HESR ring from $s = 0$ m to $s = 575$ m. Right: the PANDA target region from $s = 500$ m to $s = 525$ m.

### 3.3 Longitudinal electric field components $E_s$

It is important to study the longitudinal electric field components $E_s$ of the antiproton beam. In drift spaces (and solenoids) the produced ions are accelerated in the longitudinal direction by those field components towards the potential minima. Knowing the central potential $U(s)$ in fine steps $s_i$ one can deduce numerically the longitudinal electric field component $E_s$,

$$E_s = -\frac{U_{i+1} - U_i}{s_{i+1} - s_i}. \tag{11}$$

The resulting longitudinal electric field along the beam axis is shown in Fig. 8. The longitudinal field $E_s$ is directed in the positive or negative direction depending on the local gradient of the central potential. The zero crossings mark the positions of maxima and minima of the beam potential $U(s)$. The longitudinal electric field components vary on the average between a few mV/m and about 100 mV/m. The peak-like structures near the PANDA target are due to sudden changes of the inner radius of the beam pipe which are listed in the following list.

1. Between $s = 506.606$ m and $s = 506.856$ m, the inner radius increases from 44.5 mm to 75 mm within 0.25 m yielding a longitudinal field excursion of up to +1.29 V/m which is large and has the same sign as the preceding longitudinal field of about +0.12 V/m.
2. Between $s = 509.231$ m and $s = 509.481$ m, the inner radius decreases from 75 mm to 10 mm within 0.25 m yielding a longitudinal field excursion of up to -7.5 V/m which is very large and has an opposite sign compared to the preceding longitudinal field values of about +0.01 V/m.
3. Between $s = 509.631$ m and $s = 509.731$ m, the inner radius increases from 10 mm to 20 mm within 0.10 m yielding a longitudinal field excursion of +3.79 V/m with an opposite sign with respect to the neighbouring field values of about -0.13 V/m.
4. Between $s = 510.631$ m and $s = 510.731$ m, the inner radius increases from 20 mm to 32 mm within 0.10 m yielding a longitudinal field excursion of +2.48 V/m with an opposite sign with respect to the neighbouring field values of about -0.13 V/m.
5. Between $s = 512.331$ m and $s = 512.581$ m, the inner radius increases from 32 mm to 52 mm within 0.25 m yielding a longitudinal field excursion of up to +1.35 V/m again with an opposite sign with respect to the neighbouring field values of about -0.12 V/m.
6. Between $s = 512.781$ m and $s = 513.181$ m, the inner radius decreases from 52 mm to 50 mm within 0.40 m yielding a longitudinal field excursion of up to -0.22 V/m in the same direction as the neighbouring field values of about -0.11 V/m.
7. Between $s = 515.631$ m and $s = 515.831$ m, the inner radius increases from 50 mm to 90 mm within 0.20 m yielding a longitudinal field excursion of up to +2.02 V/m with an opposite sign with respect to the neighbouring field values of about -0.08 V/m.
8. Between $s = 520.031$ m and $s = 520.231$ m, the inner radius increases from 90 mm to 125 mm within 0.20 m yielding a longitudinal field excursion of up to +1.01 V/m with an opposite sign with respect to the neighbouring field values of about -0.048 V/m.
9. Between $s = 521.731$ m and $s = 522.031$ m, the inner radius decreases from 125 mm to 75 mm within 0.30 m yielding a longitudinal field excursion of up to -1.52 V/m in the same direction as the neighbouring field values of about -0.0428 V/m.
10. Between $s = 522.131$ m and $s = 522.231$ m, the inner radius decreases from 75 mm to 44.5 mm within 0.10 m yielding a longitudinal field excursion of up to -2.94 V/m in the same direction as the neighbouring field values of about -0.042 V/m.

The longitudinal electric field components can be used in order to accelerate trapped ions towards clearing electrodes. This is possible in the region of straight sections which consist of drift spaces, quadrupole magnets, sextupole magnets and solenoids. However, it is not possible to use this effect in the region of dipole magnets. There, the ions gyrate around the magnetic field lines. Finally, we note that the longitudinal electric field components $E_s$ depend strongly on the number $N_{\bar{p}}$ of stored antiprotons. For $N_{\bar{p}} = 1.0 \cdot 10^{10}$, the potential depths and therewith the field components $E_s$ decrease by about a factor of eight, see discussion at the end of Subsect. 3.1.

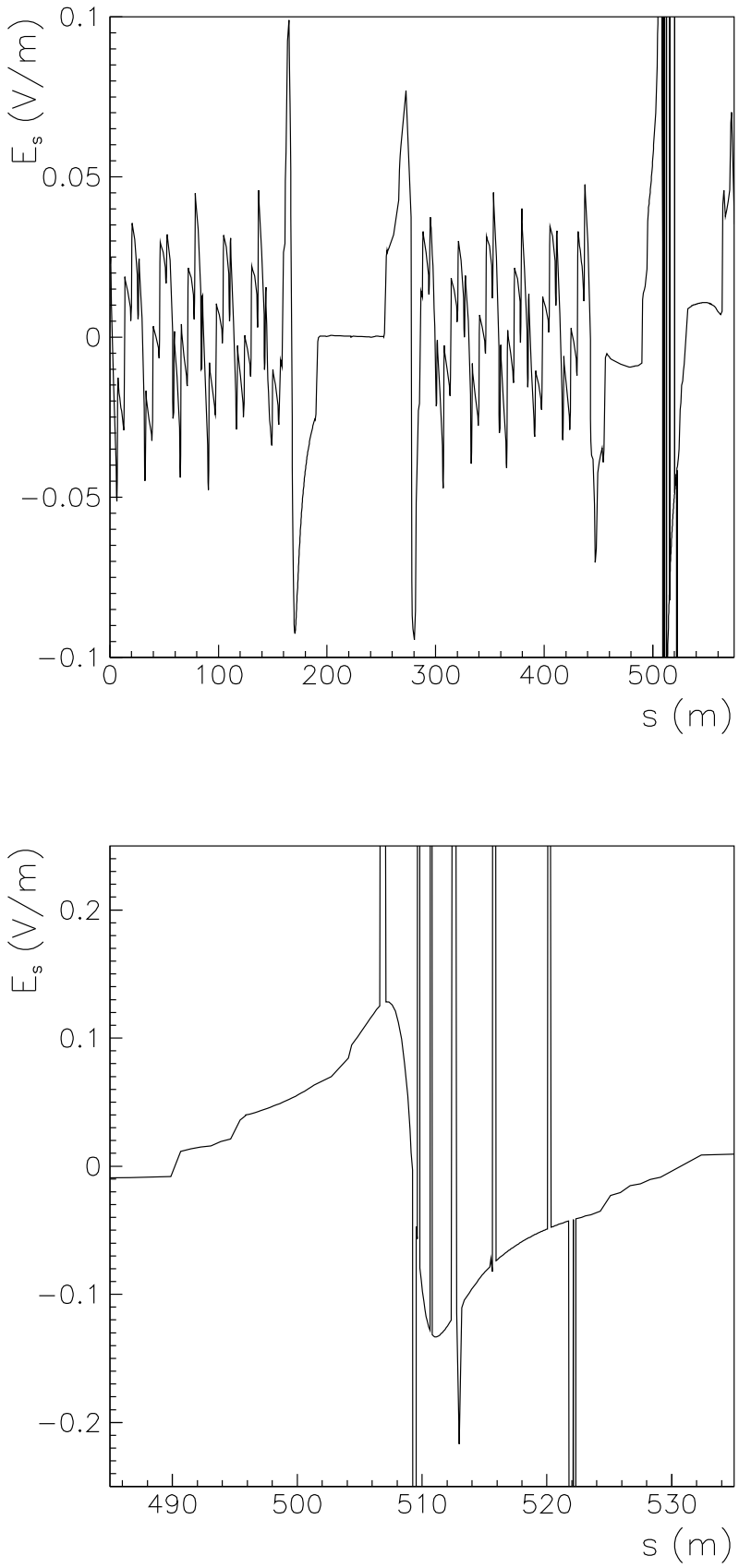


Fig. 8: Longitudinal electric field component $E_s$ of the antiproton beam assuming the standard optics, $L_1 = 0.9C$, $p_{\bar{p}} = 15$ GeV/c and $N_{\bar{p}} = 1.0 \cdot 10^{11}$.The modification of the beam potential by the neutralization $\eta$ is neglected. Top: the complete HESR ring from $s = 0$ m to $s = 575$ m. Bottom: the PANDA target region from $s = 485$ m to $s = 535$ m. The peak-like structures near the PANDA target are due to sudden changes of the inner radius of the beam pipe.

## 4. Residual Gas Pressure

In order to estimate the ionization of the residual gas molecules one needs the density $\rho_m = N_m/V$ of the residual gas molecules. Outside of the PANDA target region the UHV vacuum pressure amounts to $\leq 1.0 \cdot 10^{-9}$ mbar which can be achieved without heating the beam pipes. There is a large pressure bump in the region of the PANDA target where the pressure rises up to about $6 \cdot 10^{-5}$ mbar [22, 23]. The target is located at $s = 509.481$ m. The pressure as a function of the position $s$ in the ring is shown in Fig. 9. The residual gas contains mainly $H_2$ molecules. Therefore, the beam neutralization by trapped ions is dominated by $H_2^+$ ions. The interaction of the beam with trapped $H_2^+$ ions yields also a certain amount of trapped $H^+$ ions in the beam. In addition, there are always CO molecules present in the UHV. The CO molecules are produced by surface processes near gauges and pumps. Surface hydroxides are reduced by hot electrons or ions (in gauges and ion pumps) and liberate oxygen which combines with carbon on surfaces (which is always there also) [24].

In order to cure the adverse effects of trapped ions a very good UHV vacuum is needed. In this context, we mention a recommendation of Alain Poncet [24] who recommends the installation of bake-out jackets from the start (even if not used at the beginning "cheap" start with no power and control equipment for bake-out). The baked UHV vacuum system at the CERN Antiproton Accelerator was operated at pressures of about $1.3 \cdot 10^{-11}$ mbar! But the main problem of HESR is the huge pressure bump in the region of the PANDA target.

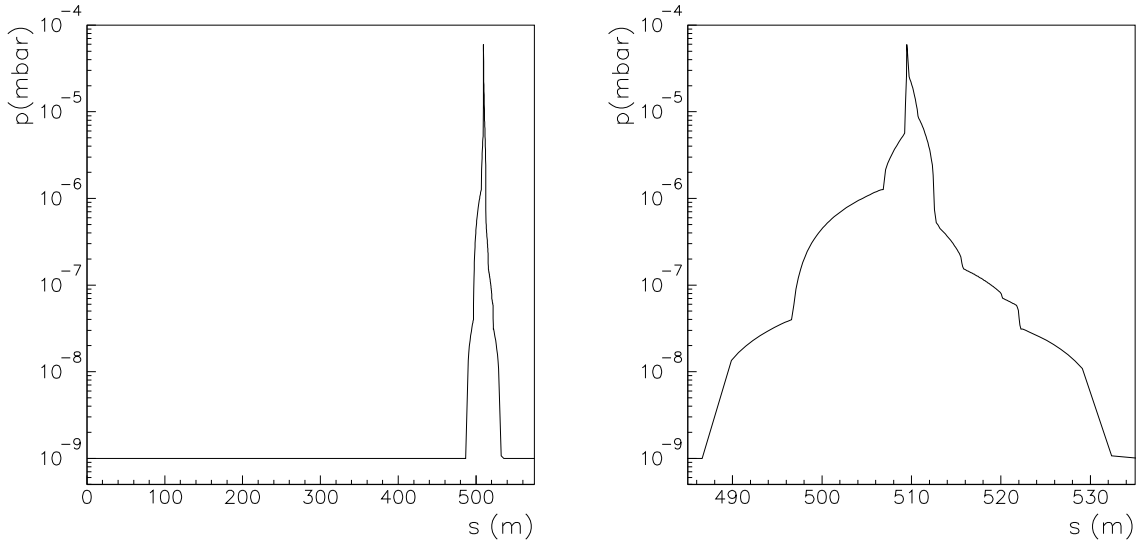


Fig. 9: Vacuum pressure $p(s)$. Left: the complete HESR ring from $s = 0$ m to $s = 575$ m. Right: the PANDA target region from $s = 485$ m to $s = 535$ m. The PANDA target is located at $s = 509.481$ m.

## 5. The Ionization Process

### 5.1 Energy transfer

The circulating antiprotons interact with the electrons of the residual gas molecules. The differential cross section for an ionization process with an energy transfer between $E$ and $E + \mathrm{d}E$ may be written

$$\frac{\mathrm{d}\sigma}{\mathrm{d}E} = 2\,\pi \frac{m_e c^2}{\beta^2} r_e^2 \frac{Z}{A} \left(1 \,-\, \beta^2 \frac{E}{E_{max}}\right) \frac{1}{E^2}. \tag{12}$$

Here, $Z/A$ refers to the residual gas molecule. The constants are the electron mass, $m_e c^2 = 0.511$ MeV, the classical electron radius, $r_e = 2.818 \cdot 10^{-13}$ cm and the maximum energy transfer $E_{max}$,

$$E_{max} = \frac{2\,m_e c^2 \beta^2 \gamma^2}{1 + 2\,\gamma (m_e/m) + (m_e/m)^2}. \tag{13}$$

Here, $m_e$ is the electron mass, $m$ the antiproton mass and $\beta$ and $\gamma$ depend on the beam energy. We get for instance for a kinetic energy of 8.0 GeV $\beta = 0.9945$, $\gamma = 9.526$ and $E_{max} = 91.7$ MeV. This numerical example shows that the energy transfer can be very high. But due to the $1/E^2$ dependence of the differential cross section, ionization events occur mainly at rather low transfer energies. It is interesting to evaluate the mean energy transfer $\bar{E}$,

$$\bar{E} = \int_I^{E_{max}} \frac{\mathrm{d}\sigma}{\mathrm{d}E} E \mathrm{d}E \,/\, \int_I^{E_{max}} \frac{\mathrm{d}\sigma}{\mathrm{d}E} \mathrm{d}E. \tag{14}$$

The minimum energy transfer is not zero. It is given by the mean excitation energy $I$ of the residual gas molecule. An ionization occurs only if the energy transferred to the electron is above the ionization potential. Solving (14), we get

$$\bar{E} = I \left(\ln \frac{E_{max}}{I} - \beta^2\right). \tag{15}$$

For $H_2$ gas molecules $I$ amounts to 19.2 eV. For an antiproton beam of 8.0 GeV kinetic energy and $H_2$ molecules we get a mean energy transfer

$$\bar{E} = 430 \text{ eV}. \tag{16}$$

This example shows that the mean electron energies from ionization processes are much larger than the mean thermal energy of 0.039 eV at 300 K. The corresponding rms velocity amounts to about $1.23 \cdot 10^7$ m/s. Thus, the electrons leave the potential well of the antiproton beam with rather high velocities.

In this context we mention that the energy transfer to the ion is negligibly small. Therefore, the rms velocities of the ions can be estimated using the mean thermal energy of 0.039 eV at 300 K, see Subsection 7..

### 5.2 Ionization cross section

The integrated ionization cross section depends on the molecules in the residual gas and the velocity $\beta = v/c$ of the beam particles. It does not depend on the charge and the mass of the beam particles. Using Bethe's formula it can be described by

$$\sigma = 4\pi \left(\frac{\hbar}{m_e c}\right)^2 \left\{ M^2 \left[\frac{1}{\beta^2} \ln \left(\frac{\beta^2}{1-\beta^2}\right) - 1\right] + \frac{C}{\beta^2} \right\}, \tag{17}$$

where

$$4\pi \left( \frac{\hbar}{m_e c} \right)^2 = 1.874 \cdot 10^{-24}\ \mathrm{m}^2. \tag{18}$$

The constants are listed in Table 1. The resulting ionization cross sections are listed in Table 2 for different molecules and four beam momenta. The cross sections for CO and $N_2$ are nearly equal.

Table 1: The constants $M^2$ and $C$ for the calculation of the ionization cross section.

| Molecule | $M^2$ | $C$ | $Z$ | $A$ |
|---|---|---|---|---|
| $H_2$ | 0.695 | 8.115 | 2 | 2 |
| $CH_4$ | 4.23 | 41.85 | 10 | 16 |
| $H_2O$ | 3.24 | 32.26 | 10 | 18 |
| $N_2$ | 3.74 | 34.84 | 14 | 28 |
| CO | 3.70 | 35.14 | 14 | 28 |
| $O_2$ | 4.20 | 38.80 | 16 | 32 |
| $CO_2$ | 5.75 | 55.92 | 22 | 44 |

Table 2: Ionization cross sections.

| $p_{\bar{p}}$ (GeV/c) | $\sigma(\mathrm{H_2})$ (m$^2$) | $\sigma(\mathrm{CH_4})$ (m$^2$) | $\sigma(\mathrm{H_2O})$ (m$^2$) | $\sigma(\mathrm{CO})$ (m$^2$) | $\sigma(\mathrm{O_2})$ (m$^2$) |
|---|---|---|---|---|---|
| 1.500 | $2.16 \cdot 10^{-23}$ | $1.12 \cdot 10^{-22}$ | $8.60 \cdot 10^{-23}$ | $9.37 \cdot 10^{-23}$ | $1.04 \cdot 10^{-22}$ |
| 3.825 | $1.87 \cdot 10^{-23}$ | $9.88 \cdot 10^{-23}$ | $7.61 \cdot 10^{-23}$ | $8.35 \cdot 10^{-23}$ | $9.27 \cdot 10^{-23}$ |
| 8.889 | $2.00 \cdot 10^{-23}$ | $1.07 \cdot 10^{-22}$ | $8.27 \cdot 10^{-23}$ | $9.11 \cdot 10^{-23}$ | $1.01 \cdot 10^{-22}$ |
| 15.000 | $2.12 \cdot 10^{-23}$ | $1.15 \cdot 10^{-22}$ | $8.84 \cdot 10^{-23}$ | $9.78 \cdot 10^{-23}$ | $1.09 \cdot 10^{-22}$ |

### 5.3 Ionization rate

The production of ions, i.e. the ionization rate $dN_{ion}/dt$, depends on the local density $N_m/V$ of the molecules in the residual gas of the beam pipe vacuum, the beam current, i.e. the number of stored antiprotons $N_{\bar{p}}$ times the revolution frequency $f$ and the ionization cross section $\sigma$. In order to get a rough estimate, we first calculate the ionization rate assuming a constant vacuum pressure of about $1.0 \cdot 10^{-9}$ mbar everywhere in the HESR ring. At this pressure the residual gas consists mainly of hydrogen molecules. Therefore, we assume a partial hydrogen pressure $p = 1.0 \cdot 10^{-9}$ mbar = $1.0 \cdot 10^{-7}$ Pa. The corresponding number of hydrogen molecules per volume $\rho_m = N_m/V$ reads

$$\rho_m = \frac{N_m}{V} = \frac{p}{kT}. \tag{19}$$

Here, $p$ is the partial pressure, $k$ the Boltzmann constant and T the absolute temperature. With $p = 1.0 \cdot 10^{-9}$ mbar = $1.0 \cdot 10^{-7}$ Pa and $T = 293$ K we get

$$\rho_m = 2.47 \cdot 10^{13}\ \mathrm{m}^{-3}. \tag{20}$$

The ionization rate of singly ionized molecules can be calculated using

$$\frac{dN_{ion}}{dt} = \sigma N_{\bar{p}} f \rho_m C = N_{\bar{p}} \sigma \rho_m \beta c. \tag{21}$$

Here, $N_{\bar{p}}$ is the number of antiprotons in the ring, $f$ the revolution frequency, $C$ the circumference and $\beta c$ the velocity, $\beta c = Cf$. Assuming the maximum momentum of 15 GeV/c we get for $H_2$ molecules ($\rho_m = 2.47 \cdot 10^{13}$ m$^{-3}$) with $C = 575.1894$ m, $f = 5.202 \cdot 10^5$ s$^{-1}$ and $N_{\bar{p}} = 1.0 \cdot 10^{11}$

$$\frac{dN_{ion}}{dt} = 1.57 \cdot 10^{10} \text{ s}^{-1}. \tag{22}$$

If there are no losses one has $1.0 \cdot 10^{11}$ positive ions in a very short time, i.e. within $6.4$ s and, taking the short time gap of the barrier bucket bunches into account, the negative space charge of the beam is fully neutralized within 7.1 s. In the region of the PANDA target, the residual gas pressure is much higher and the neutralization of the beam is achieved in a much shorter time.

Before we discuss the local ionization rate, we estimate the ionization rate of CO molecules assuming a typical partial pressure of $1.0 \cdot 10^{-10}$ mbar, i.e. 10 % of $1.0 \cdot 10^{-9}$ mbar. We note that the ionization cross section of the heavier molecules is larger than that of hydrogen. Thus, we get

$$\frac{dN_{ion}}{dt} = 0.70 \cdot 10^{10} \text{ s}^{-1}. \tag{23}$$

Taking such a contribution into account the total ionization rate increases by about 45 % and amounts to $2.27 \cdot 10^{10}$ s$^{-1}$. Without losses $1.0 \cdot 10^{11}$ positive ions would be produced within 4.4 s.

These first estimates show that it is mandatory to remove the ions quickly, i.e. to suppress the accumulation of ions in the potential well of the beam. This is necessary in view of the adverse effects of positive ions in the stored antiproton beam.

### 5.4 Local ionization rate, neutralization rate and neutralization time

The ionization rate depends on the local pressure of the residual gas molecules. In the region of the PANDA target the pressure is several orders of magnitude higher than $1.0 \cdot 10^{-9}$ mbar. Thus, the molecule density $\rho_m$ depends on the position $s$, $\rho_m = \rho_m(s)$. In order to describe the ionization rate as a function of the position $s$ in the ring, we define the ionization rate per length $d\dot{N}_{ion}/ds$ and write

$$\frac{d\dot{N}_{ion}}{ds} = \sigma N_{\bar{p}} f \rho_m(s). \tag{24}$$

Taking the effect of different molecules $i$ in the residual gas into account the local ionization rate may be written

$$d\dot{N}_{ion}/ds = \sum_{i=1}^{n} \sigma_i N_{\bar{p}} f \rho_{m,i}(s), \tag{25}$$

where $\sigma_i$ is the ionization cross section and $\rho_{m,i}$ the number of molecules $i$ per volume.

The local neutralization factor $\eta$ is defined as the number of positive elementary charges per meter $dN_{ion}/ds$ divided by the number of negative antiprotons per meter. Assuming that the ions are singly charged, we can write

$$\eta = \frac{dN_{ion}}{ds} \frac{L_1}{N_{\bar{p}}}. \tag{26}$$

If there is a build-up of multiply charged ions the last equation has to be modified accordingly. Neglecting losses, the corresponding local neutralization rate $\dot{\eta}$ may be written

$$\dot{\eta} = \frac{d\dot{N}_{ion}}{ds}\frac{L_1}{N_{\bar{p}}} = \sigma\rho_m(s)\beta c\frac{L_1}{C}. \tag{27}$$

Here, $L_1$ is the length of the barrier bucket bunch and $N_{\bar{p}}/L_1$ denotes the line density of the beam particles. It is interesting to note that the number of antiprotons cancels if neutralization rates $\dot{\eta}$ and the resulting neutralization $\eta$ are considered. In the literature, the corresponding neutralization time $T_n$ is defined as the time it takes to achieve full neutralization of the beam bunches, if one starts with $\eta = 0$ and ion losses are neglected. Then, the line density of antiprotons is compensated by a corresponding line density of positive ions. The neutralization time $T_n$ is given by

$$T_n = \frac{1}{\dot{\eta}} = \frac{1}{\sigma\rho_m(s)\beta c}\frac{C}{L_1}. \tag{28}$$

For a partial pressure of $1.0 \cdot 10^{-9}$ mbar for hydrogen molecules and $L_1/C = 0.9$ one gets

$$\dot{\eta} = 0.141\ \mathrm{s}^{-1}, \quad T_n = 7.1\ \mathrm{s} \quad (1.0 \cdot 10^{-9}\ \mathrm{mbar}). \tag{29}$$

For a partial pressure of $1.0 \cdot 10^{-5}$ mbar for hydrogen molecules one gets

$$\dot{\eta} = 1410\ \mathrm{s}^{-1}, \quad T_n = 7.1 \cdot 10^{-4}\ \mathrm{s} \quad (1.0 \cdot 10^{-5}\ \mathrm{mbar}). \tag{30}$$

That means, if losses are neglected, the local neutralization $\eta$ amounts to 14.1 % after 0.1 ms and the beam is fully neutralized in a very short time period of 0.71 ms. In Sect. 6.1 we define the so-called production time $T_p$. This quantity is equivalent to the neutralization time $T_n$, i.e. $T_p = T_n L_1/C$.

## 6. Production Time $T_p$, Clearing Time $T_c$ and Neutralization $\eta$

### 6.1 Production time $T_p$

In order to estimate the amount of neutralization we define the production time $T_p$, the production rate $R_p$, the clearing time $T_c$ and the clearing rate $R_c$. The production time $T_p$ refers to the ionization produced by one single antiproton in the beam. It is defined as the time which is needed to neutralize the negative elementary charge of the antiproton. The production rate $R_p$ is the inverse of $T_p$. Taking the effect of different molecules $i$ in the residual gas into account the production rate may be written

$$R_p = \sum_{i=1}^{n} \sigma_i \rho_{m,i} \beta c, \tag{31}$$

where $\sigma_i$ is the ionization cross section and $\rho_{m,i}$ the number of molecules $i$ per volume. If the ionization process is dominated by the production of singly charged $H_2^+$ ions we have $R_p = \sigma \rho_m \beta c$. The resulting ionization rate is given by the number $N_{\bar{p}}$ of antiprotons in the ring and the production rate $R_p$

$$\frac{dN_{ion}}{dt} = N_{\bar{p}} R_p. \tag{32}$$

Finally, we note

$$T_p = \frac{1}{R_p}. \tag{33}$$

We mention that the production time $T_p$ is proportional to the neutralization time $T_n$ defined in Eq. (28), i.e. $T_p = T_n L_1 / C$. Thus, the production time is simply the time which one single antiproton needs in order to produce one single ion (if singly charged ions dominate the ionization process). We note that the production time $T_p$ depends on the local partial densities

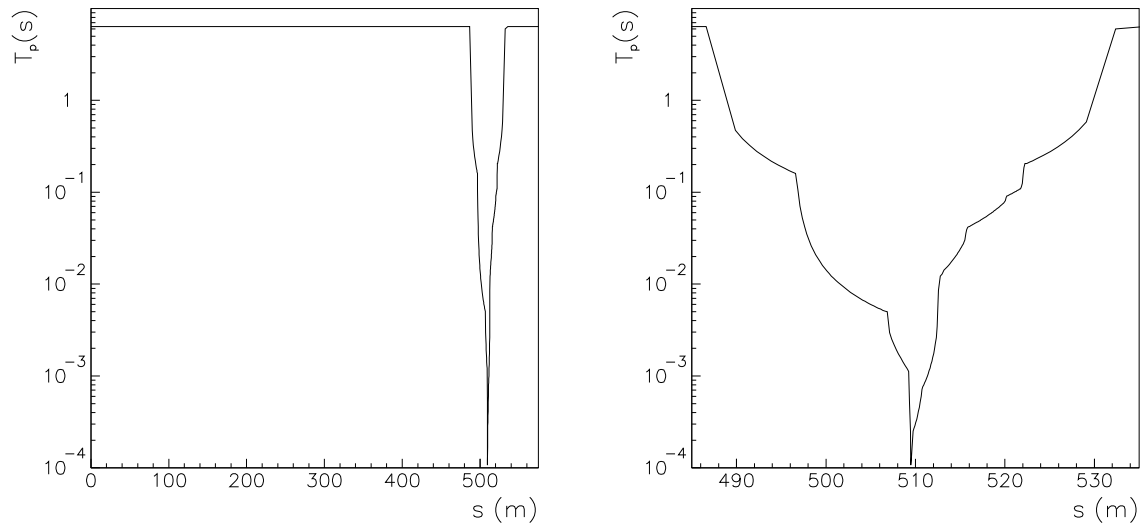


Fig. 10: Production time $T_p(s)$ for $H_2^+$ ions assuming the standard optics, $L_1 = 0.9C$, $p_{\bar{p}} = 15$ GeV/c and $N_{\bar{p}} = 1.0 \cdot 10^{11}$. Left: the complete HESR ring from $s = 0$ m to $s = 575$ m. Right: the PANDA target region from $s = 485$ m to $s = 535$ m. The PANDA target is located at $s = 509.481$ m.

$\rho_{m,i}(s)$ and therewith on the local partial pressures $p_i(s)$. Since the residual vacuum of the HESR ring is dominated by hydrogen molecules $H_2$ we assume in the following estimates only the effect of hydrogen molecules. In this context, we recall that other molecules like for instance $N_2$ and CO exhibit larger ionization cross sections (see Table 2). They should be taken into account if the partial pressure of those molecules is substantial. In Sects. 12. and 13. the effects of heavier molecules are estimated by assuming 20 % CO molecules, i.e. by assuming partial pressures of $0.2 \cdot 10^{-9}$ mbar for CO and $0.8 \cdot 10^{-9}$ mbar for $H_2$ molecules. Here we assume, that the partial pressure of $H_2$ molecules is practically equal to the total pressure, $p_{H_2} = p$. Then, the local production time $T_p(s)$ is inversely proportional to the local pressure $p(s)$. The vacuum pressure in the HESR ring will be $p = 1 \cdot 10^{-9}$ mbar. In the PANDA target region the pressure rises up to about $6 \cdot 10^{-5}$ mbar. In order to take this pressure bump into account the pressure profile $p(s)$ near the PANDA target [22, 23] has been taken into account in the following calculations. The pressure profile is shown in Fig. 9. The resulting production time $T_p(s)$ is shown in Fig. 10. In the PANDA target region, the production time has a marked dip with nearly $1 \cdot 10^{-4}$ s at the minimum. In regions with $1 \cdot 10^{-9}$ mbar, the production time amounts to 6.4 s (at 15 GeV/c).

### 6.2 Clearing time $T_c$

The clearing time $T_c$ refers to the time which is needed to remove one positive elementary charge out of the beam. If singly charged ions dominate it is the time needed to remove one single ion. In other words, the clearing time $T_c$ defines the mean lifetime of the positive ion in the beam. The clearing time is the inverse of the clearing rate,

$$T_c = \frac{1}{R_c}. \tag{34}$$

The clearing rate depends on many different clearing processes,

$$R_c = \sum_{i=1}^{m} R_{c,i}. \tag{35}$$

Now, we consider the differential equation of the number $N_{ion}$ in the beam (again assuming only singly charged ions),

$$\frac{dN_{ion}}{dt} = \frac{N_{\bar{p}}}{T_p} - \frac{N_{ion}}{T_c}. \tag{36}$$

The production (and the trapping) of ions is proportional to the number of antiprotons. The number of removed ions per second depends on the momentary number of ions in the beam. The solution may be written

$$N_{ion}(t) = N_{ion}(0)\exp(-\frac{t}{T_c}) + N_{\bar{p}}\frac{T_c}{T_p}[1 - \exp(-\frac{t}{T_c})]. \tag{37}$$

Normally, the number of ions $N_{ion}(0)$ at the beginning is zero and the number of ions in the beam tends asymptotically towards $N_{\bar{p}}T_c/T_p$. That means the number of produced ions is equal to the number of cleared ions and we have in the steady state

$$N_{ion} = N_{\bar{p}}\frac{T_c}{T_p} = N_{\bar{p}}\frac{R_p}{R_c}. \tag{38}$$

This steady state is quickly reached after a few time periods $T_c$.

### 6.3 Neutralization

The resulting neutralization $\eta$ of the beam may be written

$$\eta = \frac{N_{ion}}{C}\frac{L_1}{N_{\bar{p}}} = \frac{L_1}{C}\frac{T_c}{T_p} = \frac{L_1}{C}\frac{R_p}{R_c}. \tag{39}$$

These equations can be generalized in order to describe the local neutralization $\eta(s)$,

$$\frac{dN_{ion}}{ds} = \frac{N_{\bar{p}}}{C}\frac{T_c(s)}{T_p(s)} = \frac{N_{\bar{p}}}{C}\frac{R_p(s)}{R_c(s)}, \tag{40}$$

$$\eta(s) = \frac{dN_{ion}}{ds}\frac{L_1}{N_{\bar{p}}} = \frac{L_1}{C}\frac{T_c(s)}{T_p(s)} = \frac{L_1}{C}\frac{R_p(s)}{R_c(s)}. \tag{41}$$

Thus, one has to estimate the local clearing time $T_c(s)$ and the local production time $T_p(s)$ in order to estimate the local neutralization $\eta(s)$. We note that $L_1/C = 0.9$ for the barrier bucket mode of the HESR. Thus, we get $\eta(s) = 0.9\,T_c(s)/T_p(s)$ for the HESR.

## 7. Mean Thermal Energy and Mean Thermal Velocity

Since the momentum transfer during the ionization process is negligibly small the mean energy of the ions at the moment of ionization is equal to the mean thermal energy of the molecules,

$$\bar{W}_i = \frac{3}{2}kT. \tag{42}$$

For $T = 300$ K we get $\bar{W}_i = 0.039$ eV. This mean thermal energy of the positive ions is small compared to the typical well depth of the antiproton beam (1 V - 3 V). Therefore, the positive ions can be trapped by the antiproton beam.

The corresponding mean velocities are the rms velocity $v_{rms}$

$$v_{rms} = \sqrt{\frac{3kT}{m_i}}, \tag{43}$$

and the mean value of the magnitude of the velocities in one direction $\bar{v}_{\parallel}$,

$$\bar{v}_{\parallel} =< |v_x| >=< |v_y| >=< |v_z| >= \sqrt{\frac{2kT}{\pi m_i}}. \tag{44}$$

They are listed in Tab. 3.

Table 3: Mean thermal velocities ($T = 300$ K, $\bar{W}_i = 0.039$ eV).

| Particle | A | $v_{rms}$ (m/s) | $\bar{v}_{\parallel}$ (m/s) |
|---|---|---|---|
| e | 1/1836 | $1.17{\cdot}10^5$ | $5.38{\cdot}10^4$ |
| H | 1 | $2.73{\cdot}10^3$ | $1.26{\cdot}10^3$ |
| $H_2$ | 2 | $1.93{\cdot}10^3$ | $8.89{\cdot}10^2$ |
| $CH_4$ | 16 | $6.81{\cdot}10^2$ | $3.14{\cdot}10^2$ |
| $H_2O$ | 18 | $6.42{\cdot}10^2$ | $2.96{\cdot}10^2$ |
| $CO/N_2$ | 28 | $5.15{\cdot}10^2$ | $2.37{\cdot}10^2$ |
| $O_2$ | 32 | $4.82{\cdot}10^2$ | $2.22{\cdot}10^2$ |
| $CO_2$ | 44 | $4.11{\cdot}10^2$ | $1.89{\cdot}10^2$ |

## 8. Ion Motion in Dipole, Quadrupole and Sextupole Magnets

### 8.1 Cyclotron motion of trapped ions in bending magnets

The motion of an ion in the vertical direction along the magnetic field $\vec{B} = (0, B_y, 0)$ of the bending magnets is like in a field free drift space. Thus, the vertical ion oscillations due to the vertical component $E_y$ of the electric field of the beam are not influenced by the magnet field. In order to extract ions out of the beam one should install clearing electrodes yielding external electric fields in the vertical $y$-direction.

The motion of the ions in the transverse $x$- and the longitudinal $z$-direction is far from being free. An ion with a velocity $v_\perp$ perpendicular to the uniform magnetic field of a bending magnet performs the well known cyclotron motion around the magnetic field lines. The angular frequency $\omega_i$ (cyclotron frequency) is given by

$$\omega_i = \frac{q_i B}{m_i}. \tag{45}$$

The radius of the gyration around the magnetic field depends on the velocity $v_i$ perpendicular to the field lines,

$$r_i = \frac{m_i v_i}{q_i B}. \tag{46}$$

In the following Tables we list for some typical magnetic fields $B$ the angular frequency $\omega_i$, the revolution frequency $f_i = \omega_i/(2\pi)$, the revolution time $T_i = 1/f_i$ and the cyclotron radius $r_i = v_i/\omega_i$ for $H^+$ and $H_2^+$ ions. For $v_i$, we take the mean thermal velocity in one direction, $\bar{v}_\parallel = \sqrt{2kT/(\pi m_i)}$, with $T = 300$ K (see Table 3). We mention that the cyclotron frequencies $f_i$ of the ions are generally quite high, and the radii $r_i$ for mean thermal velocities $\bar{v}_\parallel$ are very small.

Table 4: Cyclotron motion of thermal $\mathbf{H^+}$ **ions** ($T = 300$ K): magnetic field $B$, angular frequency $\omega_i$, cyclotron frequency $f_i$, revolution time $T_i$, radius $r_i$.

| $B$ (T) | $\omega_i$ ($s^{-1}$) | $f_i$ (Hz) | $T_i$ (s) | $\bar{r}_i$ (m) |
|---|---|---|---|---|
| 3.0 | $2.87 \cdot 10^8$ | $4.57 \cdot 10^7$ | $2.19 \cdot 10^{-8}$ | $4.37 \cdot 10^{-6}$ |
| 2.0 | $1.91 \cdot 10^8$ | $3.05 \cdot 10^7$ | $3.29 \cdot 10^{-8}$ | $6.56 \cdot 10^{-6}$ |
| 1.7 | $1.63 \cdot 10^8$ | $2.59 \cdot 10^7$ | $3.86 \cdot 10^{-8}$ | $7.71 \cdot 10^{-6}$ |
| 1.5 | $1.44 \cdot 10^8$ | $2.29 \cdot 10^7$ | $4.37 \cdot 10^{-8}$ | $8.74 \cdot 10^{-6}$ |
| 0.2 | $1.92 \cdot 10^7$ | $3.05 \cdot 10^6$ | $3.28 \cdot 10^{-7}$ | $6.55 \cdot 10^{-5}$ |
| 0.17 | $1.63 \cdot 10^7$ | $2.59 \cdot 10^6$ | $3.86 \cdot 10^{-7}$ | $7.71 \cdot 10^{-5}$ |
| 0.03 | $2.87 \cdot 10^6$ | $4.57 \cdot 10^5$ | $2.19 \cdot 10^{-6}$ | $4.37 \cdot 10^{-4}$ |
| 0.02 | $1.92 \cdot 10^6$ | $3.05 \cdot 10^5$ | $3.28 \cdot 10^{-6}$ | $6.55 \cdot 10^{-4}$ |
| 0.01 | $0.96 \cdot 10^6$ | $1.52 \cdot 10^5$ | $6.57 \cdot 10^{-6}$ | $1.31 \cdot 10^{-3}$ |

Table 5: Cyclotron motion of thermal $\mathbf{H}_2^+$ **ions** ($T = 300$ K): magnetic field $B$, angular frequency $\omega_i$, cyclotron frequency $f_i$, revolution time $T_i$, radius $r_i$.

| $B$ (T) | $\omega_i$ (s$^{-1}$) | $f_i$ (Hz) | $T_i$ (s) | $\bar{r}_i$ (m) |
|---|---|---|---|---|
| 3.0 | $1.44 \cdot 10^8$ | $2.29 \cdot 10^7$ | $4.37 \cdot 10^{-8}$ | $6.18 \cdot 10^{-6}$ |
| 2.0 | $9.60 \cdot 10^7$ | $1.53 \cdot 10^7$ | $6.54 \cdot 10^{-8}$ | $9.27 \cdot 10^{-6}$ |
| 1.7 | $8.14 \cdot 10^7$ | $1.30 \cdot 10^7$ | $7.72 \cdot 10^{-8}$ | $1.09 \cdot 10^{-5}$ |
| 1.5 | $7.18 \cdot 10^7$ | $1.14 \cdot 10^7$ | $8.75 \cdot 10^{-8}$ | $1.24 \cdot 10^{-5}$ |
| 0.2 | $9.58 \cdot 10^6$ | $1.52 \cdot 10^6$ | $6.56 \cdot 10^{-7}$ | $9.27 \cdot 10^{-5}$ |
| 0.17 | $8.14 \cdot 10^6$ | $1.30 \cdot 10^6$ | $7.72 \cdot 10^{-7}$ | $1.09 \cdot 10^{-4}$ |
| 0.03 | $1.44 \cdot 10^6$ | $2.29 \cdot 10^5$ | $4.37 \cdot 10^{-6}$ | $6.18 \cdot 10^{-4}$ |
| 0.02 | $9.58 \cdot 10^5$ | $1.52 \cdot 10^5$ | $6.56 \cdot 10^{-6}$ | $9.27 \cdot 10^{-4}$ |
| 0.01 | $4.79 \cdot 10^5$ | $7.60 \cdot 10^4$ | $1.31 \cdot 10^{-5}$ | $1.85 \cdot 10^{-3}$ |

### 8.2 $\vec{E} \times \vec{B}/B^2$ cross-field drift velocity in dipole magnets

Now, we discuss the combined effect of an electric field $\vec{E}$ and a magnetic field $\vec{B}$, the so-called cross-field drift velocity $\vec{v}_D$. The cross-field drift velocity $\vec{v}_D$ arises, if $\vec{E}$ is perpendicular to $\vec{B}$,

$$\vec{v}_D = \frac{\vec{E} \times \vec{B}}{B^2}. \tag{47}$$

Thus, for an electric field $\vec{E} = (E_x, 0, 0)$ directed in the positive/negative $x$-direction and a magnetic field in the $y$-direction, $\vec{B} = (0, B_y, 0)$, the cross-field drift velocity $\vec{v}_D$ is directed into the positive/negative $z$-direction and amounts to

$$v_z = \frac{E_x}{B_y}. \tag{48}$$

The illustrative explanation of the cross-field drift velocity is shown in Fig. 11. An ion created

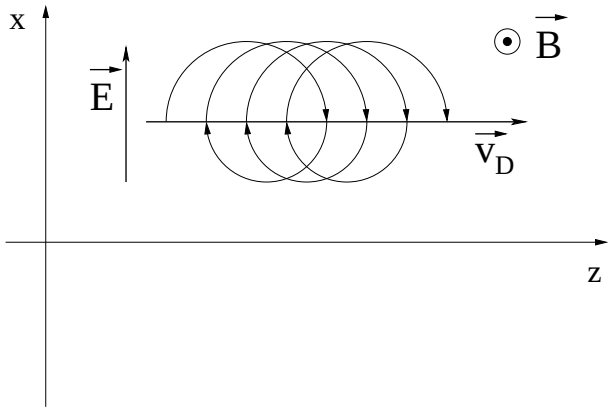


Fig. 11: Illustrative explanation of the cross-field ($\vec{E} \times \vec{B}$) drift velocity $\vec{v}_D$ of a positive ion.

with the start velocity $v_\perp$ moves on a cyclotron-like trajectory around the magnetic field lines.

During the time where the ion moves in the direction of the electric field $E_x$ it is accelerated and the radius of it's trajectory is increased. During the time where the ion moves against the direction of the electric field it is decelerated and the radius of it's trajectory is decreased. As a consequence, a mean drift velocity $\vec{v}_D$ perpendicular to the $\vec{B}$- and $\vec{E}$ fields arises. The drift velocity $\vec{v}_D$ is independent of the start velocity $v_\perp$, the charge $q_i$, the sign of the charge $q_i$ and the mass $m_i$ of the ion. Thus, ions (of whatever mass and charge) and electrons move in the same direction at the same velocity $\vec{v}_D$.

We note that the electric field $E_x(x)$ is not constant. Near the beam axis $E_x$ depends linearly on $x$, $E_x = \frac{\lambda}{2\,\pi\epsilon_0}\frac{1}{\sigma_x+\sigma_y}\frac{x}{\sigma_x}$. Therefore, Eq. (48) only applies if the variation of the electric field $E_x$ over the cyclotron motion is small, i.e. if

$$|r_i \partial E_x/\partial x| \ll |E_x(x)|. \tag{49}$$

This condition is fulfilled if the Larmor radius $r_i$ of the ions is very small and if the ions are created at a certain distance $x$ from the central axis with

$$|x| \gg r_i. \tag{50}$$

For instance, the Larmor radius of $H_2^+$ ions at $B_y = 1.7$ T amounts to about 11 $\mu$m, see Table 5. Thus, one can apply Eq. (48) for transverse distances $x$ with $|x| \gg 11$ $\mu$m.

The cross-field drift velocities due to the electric field components $E_x$ of the antiproton beam are largest near the edge of the beam. The absolute value of the electric field component $|E_x|$ of a bi-Gaussian beam distribution with $\sigma_x \approx \sigma_y$ has a maximum at $|x| = 1.585\,\sigma_x$. For $\lambda/(2\pi\epsilon_0) = -0.556$ V ($1.0 \cdot 10^{11}$ antiprotons) and $\sigma_x = 1.5$ mm at 15 GeV/c we get $|E_x| = 167$ V/m. This yields with $B_y = 1.7$ T

$$|v_D| \approx 98 \text{ m/s}. \tag{51}$$

We note that the cross-field drift velocity along the beam is in opposite directions on either side of the central beam axis. On the right side it is directed in the forward direction, on the left side in the backward direction. The electric field components $E_x$ and therewith the drift velocities fall to very low values for ions born near the center of the beam. They are even zero at the beam center. Therefore, high ion concentrations and high neutralization levels can exist in bending magnets, if only the mean cross-field drift velocity (see Subsects. 8.3 and 10.4) is used in order to extract the ions in the longitudinal direction. In Subsects. 10.5, 10.6 and 10.7 three different methods are presented in order to reduce the neutralization in dipole magnets substantially.

There is another cross-field drift velocity component $v_x = E_s/B_y$ due to the longitudinal electric field $E_s$ of the beam (see Fig. 8). It is directed in the transverse $x$-direction. In dipole magnets, the longitudinal electric field components $E_s$ together with the transverse magnetic field component $B_y$ yield drift velocities $v_x = E_s/B_y$ which are much too small to extract the ions in the transverse $x$-direction. We get for a typical longitudinal electric field of about 0.01 V/m $|v_x| = 0.006$ m/s at 15 GeV/c.

Magnetic mirror effects occur for ions drifting from field-free regions towards the fringe field of magnets. The longitudinal gradient of the magnetic field can reverse the ion motion thus creating a barrier. Therefore, it is also important to install clearing electrodes in the field-free sections between the magnets.

### 8.3 Estimate of the mean cross-field drift velocity in dipole magnets

Here, we evaluate the mean cross-field drift velocities $\bar{v}_D$ in dipole magnets for $x > 0$, i.e. for ions created on the left side of the beam axis and drifting in the backward direction. Ions created on the right side of the beam axis drift in the forward direction. They experience the same mean cross-field drift velocity in opposite direction, i.e. $\bar{v}_D(x \leq 0) = -\bar{v}_D(x \geq 0)$. We assume bi-Gaussian beam distributions with $\sigma_x = \sigma_y = \sigma$ in the region of the dipole magnets. The transverse electric field $E_x$ due to the beam charge is given by

$$E_x(x,y) = \frac{\lambda}{2\pi\epsilon_0}\left(1 - \exp -\frac{x^2+y^2}{2\sigma^2}\right)\frac{x}{x^2+y^2} \tag{52}$$

with $\lambda/(2\pi\epsilon_0) = -0.556$ V for $1.0 \cdot 10^{11}$ antiprotons. The absolute value of $E_x$ is zero at the beam center and rises linearly for small $x$. It has a maximum near $x = 1.585\,\sigma$, $y = 0$. The normalized transverse beam distribution function $f(x,y)$ is given by

$$f(x,y) = \frac{1}{2\pi\sigma^2}\exp -\frac{x^2+y^2}{2\sigma^2}. \tag{53}$$

The mean value $\bar{E}_x$ of the electric field components $E_x(x,y)$ on the left side of the beam distribution, i.e. for $x \geq 0$, is obtained by folding $E_x(x,y)$ with $f(x,y)$,

$$\bar{E}_x = \frac{\int_{-\infty}^{+\infty}\int_{0}^{+\infty} E_x(x,y)f(x,y)\mathrm{d}x\mathrm{d}y}{\int_{-\infty}^{+\infty}\int_{0}^{+\infty} f(x,y)\mathrm{d}x\mathrm{d}y}. \tag{54}$$

The folding can be done analytically. It yields the mean value $\bar{E}_x$,

$$\bar{E}_x = \frac{\lambda}{2\pi\epsilon_0}\,\frac{1}{\sqrt{2\pi}\sigma}\,\frac{2-\sqrt{2}}{\pi}. \tag{55}$$

The absolute value of the mean drift velocity $|\bar{v}_D|$ in longitudinal direction reads

$$|\bar{v}_D| = \frac{|\bar{E}_x|}{B_y}. \tag{56}$$

The length $L$ of the dipole magnets amounts to 4.2 m. Now, we assume that the ions are captured by clearing electrodes with clearing fields $E_y$ at the entrance and exit of a dipole magnet. We assume that the clearing electrodes are located outside of the dipole magnets and that the distance between them amounts to about 4.5 m. Thus, the mean drift distance is $L/2 = 2.25$ m and the mean clearing time $T_c$ is given by

$$T_c = \frac{L}{2|\bar{v}_D|}. \tag{57}$$

This equation holds true for ions created at $x \geq 0$ as well as $x \leq 0$. We note that the beam width $\sigma$ scales like $1/\sqrt{p}$ according to the adiabatic damping law with $\sigma \approx 1.5$ mm at 15 GeV/c. This scaling is taken into account in the evaluation of $\bar{E}_x$. The transverse magnetic field $B_y$ scales linearly with the beam momentum $p$. In Table 6, we list the mean cross-field drift velocity $|\bar{v}_D|$ and the mean clearing time $T_c$ for $L/2 = 2.25$ m. We recall that the cross-field drift velocity does not depend on the mass and charge of the ions. Thus, $CO^+$ ions experience the same drift velocity as $H_2^+$ ions.

Table 6: Mean cross-field drift velocity $|\bar{v}_D|$ and mean clearing time $T_c$ for $1.0 \cdot 10^{11}$ antiprotons and $L = 4.5$ m.

| $p$ GeV/c | $\|\bar{v}_D\|$ (m/s) | $T_c$ (s) |
|---|---|---|
| 1.5 | 51.3 | 0.0439 |
| 3.825 | 32.1 | 0.0701 |
| 8.889 | 21.1 | 0.107 |
| 15.0 | 16.2 | 0.139 |

The mean cross-field drift velocities $|\bar{v}_D|$ are rather small. This is due to the fact that the electric field $E_x$ and therewith the cross-field drift velocity $v_D$ drops down to zero at the beam center. Therefore, ions created near the beam center are practically not cleared and the resulting mean cross-field drift velocities are rather low in dipole magnets when averaged over the Gaussian beam profile. As a consequence, the resulting clearing times $T_c$ are rather high.

In addition, the mean electric fields and therewith the mean cross-field drift velocities depend critically on the number $N_{\bar{p}}$ of stored protons. The linear charge density $\lambda$ is proportional to $N_{\bar{p}}$, and the beam width $\sigma$ is proportional to $N_{\bar{p}}^{2/5}$ (see Sect. 2.). Therefore, the mean cross-field drift velocity $\bar{v}_D$ is proportional to $N_{\bar{p}}^{3/5}$. Compared to $1.0 \cdot 10^{11}$ antiprotons the mean cross-field drift velocities for $1.0 \cdot 10^{10}$ antiprotons are by a factor of $10^{3/5}$=3.98 lesser and the mean clearing times $T_c$ are by a factor of $10^{3/5}$=3.98 larger than the values listed in Table 6.

### 8.4 Gradient and curvature drift velocity in quadrupole magnets

Now, we discuss the so-called gradient and curvature drift velocity which occurs in the magnetic field of a quadrupole. The gradient drift velocity depends on the ion velocity $v_\perp$ perpendicular to the magnetic field lines. We have already seen that

$$v_\perp = r_i \frac{qB}{m_i} = r_i \omega_i. \tag{58}$$

Here, we discuss the effect for an ion in the magnetic midplane making revolutions due to the local magnetic field component $B_y$ with a periodic variation of the horizontal displacement, $x = r_i \cos \omega_i t$. The radius $r_i$ is a very small quantity due to the low thermal velocities of the ions. Denoting the magnetic field at $x_0$ by $B_y(x_0)$, the magnetic field in the neighbourhood of $x_0$, i.e. at $x_0 + x$ may be written

$$B_y = B_y(x_0) + \frac{\partial B_y}{\partial x}\, x. \tag{59}$$

The projection of the velocity on z is given by

$$v_z = v_\perp \cos \omega_i t = r_i \frac{q_i B_y}{m_i} \cos \omega_i t = \left[ r_i \frac{q_i B_y(x_0)}{m_i} \right] \cos \omega_i t + \left[ r_i \frac{q_i}{m_i} \frac{\partial B_y}{\partial x} \left( r_i \cos \omega_i t \right) \right] \cos \omega_i t. \tag{60}$$

The averaging over the time yields zero for the first term but nonzero for the second term. Thus, the longitudinal drift velocity $v_D$ is given by the mean longitudinal velocity $< v_z >$,

$$v_D = < v_z > = \frac{1}{2} r_i^2 \frac{q_i}{m_i} \frac{\partial B_y}{\partial x}. \tag{61}$$

This derivation only applies if the field variation over the cyclotron motion is small, i.e. if

$$r_i \partial B_y/\partial x \ll B_y(x_0). \tag{62}$$

This condition is fulfilled if the ion is created at a certain distance $x_0$ from the quadrupole axis with $x_0 > r_i$. For instance, a typical magnetic field gradient of 10 T/m and $x_0 = 2$ mm yields $B_y(x_0) = 0.02$ T and the corresponding Larmor radii $r_i$ of $H^+$ and $H_2^+$ ions are very small ($r_i < 1$ mm) at thermal velocities, see Tables 4 and 5.

The gradient drift velocity can also be written

$$v_D = \frac{m_i}{2} v_\perp^2 \frac{1}{q_i B^2} \frac{\partial B_y}{\partial x}. \tag{63}$$

An alternative form [25] independent of the choice of coordinates is

$$\vec{v}_D = \frac{m_i}{2} v_\perp^2 \frac{1}{q_i B^2} (\vec{B} \times \vec{\nabla}_\perp B) = \frac{\omega_i r_i^2}{2B^2} (\vec{B} \times \vec{\nabla}_\perp B). \tag{64}$$

Here, $\omega_i$ is the gyration frequency and $r_i$ the gyration radius as defined in Eqs. (45) and (46). The sense of the drift velocity for positive particles is given by (64). For negative particles the sign of the drift velocity is opposite. The change of sign comes from the charge $q_i$ or the definition of $\omega_i$. The gradient drift velocity can be understood by considering the variation of the radius $r_i$ in the inhomogeneous quadrupole field as the particle moves in and out of regions of larger than average and lesser than average field strength. The gradient drift velocity can be illustrated just like the $\vec{E} \times \vec{B}$ cross-field drift velocity (see Fig. 11).

The gradient of the magnetic field in a quadrupole implies automatically a curvature of the magnetic field lines. An ion with a velocity component $v_\parallel$ follows adiabatically the field lines. The resulting centripetal force acting perpendicular to the magnetic field $\vec{B}$ yields an additional contribution to the drift velocity, the so-called curvature drift velocity. In other words, the curvature radius $R$ of the field lines yields an additional drift velocity in the longitudinal direction. The curvature drift velocity can be written

$$v_D = m_i v_\parallel^2 \frac{1}{q_i B^2} \frac{\partial B_y}{\partial x}. \tag{65}$$

Combining the gradient drift velocity and the curvature drift velocity in one equation yields

$$v_D = (m_i v_\parallel^2 + \frac{m_i}{2} v_\perp^2) \frac{1}{q_i B^2} \frac{\partial B_y}{\partial x}. \tag{66}$$

Thus, the ion drift velocity in a quadrupole magnet depends on two velocity components in the $(x, y)$ plane perpendicular to $\vec{B}$, i.e. on the velocity $v_\perp$ perpendicular to the magnetic field lines and the velocity $v_\parallel$ parallel to the field lines.

Introducing the kinetic energy terms $W_\parallel = (m_i/2) v_\parallel^2$ and $W_\perp = (m_i/2) v_\perp^2$ yields

$$v_D = (2W_\parallel + W_\perp) \frac{1}{q_i B^2} \frac{\partial B_y}{\partial x}. \tag{67}$$

An alternative form [25] independent of the choice of coordinates is

$$\vec{v}_D = (m_i v_\parallel^2 + \frac{m_i}{2} v_\perp^2) \frac{1}{q_i B^2} (\vec{B} \times \vec{\nabla}_\perp B). \tag{68}$$

Expressing $\vec{v}_D$ in terms of the radius vector $\vec{R}$ of the field line curvature yields [25]

$$\vec{v}_D = \frac{(2W_\parallel + W_\perp)}{q_i R\, B} \frac{\vec{R} \times \vec{B}}{R\, B}. \tag{69}$$

This equation can also be written as

$$\vec{v}_D = \frac{(v_\parallel^2 + v_\perp^2/2)}{\omega_i R} \frac{\vec{R} \times \vec{B}}{R\, B} = \frac{(v_\parallel^2 + v_\perp^2/2)}{v_\perp} \frac{r_i}{R} \frac{\vec{R} \times \vec{B}}{R\, B}. \tag{70}$$

The direction of the drift velocity is specified by the vector product, in which $\vec{R}$ is the radius vector from the effective center of curvature to the position of the ion. The direction is appropriate for positive ion charges. For negative ions, the opposite sign arises. We note that the two-dimensional field of a quadrupole yields

$$\frac{\vec{R} \times \vec{B}}{R\, B} = -\,\vec{e}_z \tag{71}$$

where $\vec{e}_z$ is the unit vector along the $z$ axis. Thus, we can write

$$\vec{v}_D = -\,\frac{(2W_\parallel + W_\perp)}{q_i R\, B} \vec{e}_z. \tag{72}$$

The local curvature radius $R$ of the field lines in a quadrupole is given by

$$R = R(x, y) = \frac{(x^2 + y^2)^{3/2}}{y^2 - x^2}. \tag{73}$$

In order to illustrate the gradient and curvature drift velocity we give an example taking the mean thermal energies of the ions into account. We take from the optic4 Mad-file as typical $k$-value for the quadrupoles $k = 0.3$ m$^{-2}$. The $k$ value is defined as $k = (\partial B_y/\partial x)/(B\rho)$. The maximum $B\rho$ value amounts to 50 Tm at 15 GeV/c. Thus, we get typical gradients like $(\partial B_y/\partial x) = 15$ T/m at 15 GeV/c, $(\partial B_y/\partial x) = 10$ T/m at 10 GeV/c and so on. We assume a quadrupole with a positive gradient, $g = \partial B_y/\partial x = +10$ T/m, a positive ion produced at $x_0 = 10$ mm, $y_0 = 0$ mm thus $B(x_0) = 0.10$ T. Concerning the temperature $T$, we assume $T = 300$ K. The mean thermal energy with velocities perpendicular to the magnetic field lines is given by

$$< W_\perp >= \frac{m}{2}(< v_x^2 > + < v_z^2 >) = \frac{1}{2}kT + \frac{1}{2}kT = 0.0259 \text{ eV} \tag{74}$$

and the mean thermal energy with velocities parallel to the magnetic field lines is given by

$$< W_\parallel >= \frac{m}{2} < v_y^2 >= \frac{1}{2}kT = 0.0129 \text{ eV}. \tag{75}$$

The drift velocity for singly charged ions is directed in the positive z-direction and amounts to

$$v_D = +52 \text{ m/s}. \tag{76}$$

We note that the equations (64) and (72) can only be used for rather large $x$-values, i.e. $x \geq 10$ mm. For small $x$-values the condition (62) is not fulfilled.

We emphasize that positive ions created near the $x$-axis in a quadrupole with a positive gradient $\partial B_y/\partial x > 0$ drift in the positive $z$-direction. Those created near the $y$-axis drift in the negative $z$-direction. The drift velocities are maximal along the $x$- and $y$-axis. They are zero along the diagonals where $(y^2 - x^2) = 0$, see Eqs. (72) and (73).

### 8.5 $\vec{E} \times \vec{B}/B^2$ cross-field drift velocity in quadrupole magnets

Now, we consider the $\vec{E} \times \vec{B}/B^2$ cross-field drift velocity in quadrupole magnets which occurs due to the electric field of the antiproton beam when passing the quadrupole magnet. We mention the technical note of Macek and Pivi [26] where the formalism of the $\vec{E} \times \vec{B}/B^2$ cross-field drift velocity in quadrupole magnets is described. We assume a long bunch with a line density of the beam charges $\lambda$ as prepared by the barrier-bucket mode of operation. The transverse beam distribution is described by an elliptical bi-Gaussian distribution. Near the beam axis we have in first-order approximation the following expression for the electric field vector $\vec{E}$

$$\vec{E} = \frac{\lambda}{2\pi\epsilon_0} \frac{1}{\sigma_x + \sigma_y} \begin{pmatrix} x/\sigma_x \\ y/\sigma_y \\ 0 \end{pmatrix}. \tag{77}$$

The magnetic field vector $\vec{B}$ of the quadrupole is given by

$$\vec{B} = g \begin{pmatrix} y \\ x \\ 0 \end{pmatrix}. \tag{78}$$

Here, $g = \partial B_y/\partial x$ is the magnetic field gradient. The resulting cross-field drift velocity is given by

$$\vec{v}_D = \frac{\vec{E} \times \vec{B}}{B^2} = \frac{\lambda}{2\pi\epsilon_0} \frac{1}{\sigma_x + \sigma_y} \frac{1}{g(x^2 + y^2)} \begin{pmatrix} 0 \\ 0 \\ x^2/\sigma_x - y^2/\sigma_y \end{pmatrix}. \tag{79}$$

The cross-field drift velocities in quadrupoles are exclusively directed in the longitudinal direction. Depending on the azimuth angle $\varphi$, the ions move in the forward or backward direction. We note that the magnitude of the drift velocities is highest if the ions are produced near the $x$- and $y$-axes. Ions produced near the axes with $(x^2/\sigma_x - y^2/\sigma_y) = 0$ experience zero drift velocities, $\vec{v}_D = 0$. Ions starting in the quadrants near the $x$-axis move into the negative $z$-direction and ions starting in the quadrants near the $y$-axis move into the positive $z$-direction if the field gradient $g = \partial B_y/\partial x$ is positive (and vice versa if the field gradient is negative). We note that the cross-field drift velocities and the curvature and gradient drift velocities have opposite directions in quadrupoles.

In order to estimate the drift velocity we give a numerical example. With $N_{\bar{p}} = 1 \cdot 10^{11}$ antiprotons and a bunch length $L_1 = 517.5$ m we have $\lambda = -3.10 \cdot 10^{-11}$ C/m and $\lambda/(2\pi\epsilon_0) = -0.556$ V. Assuming for the maximum momentum 15 GeV/c the typical values $g = +15$ T/m, $\sigma_x = 1.5$ mm, $\sigma_y = 1.5$ mm yields for ions created along the $x$-axis ($x > 0$ mm and $y = 0$)

$$\vec{v}_D = \begin{pmatrix} 0 \\ 0 \\ -8\,237 \text{ m/s} \end{pmatrix}. \tag{80}$$

This example shows that rather high cross-field drift velocities would be reached. The corresponding kinetic energies would be 0.71 eV for $H_2^+$ ions and 9.9 eV for $CO^+$ ions. These kinetic energies would have to be provided by the potential well of the antiproton beam. We note that the depth of the beam potential well is rather weak (about 2 V for $1.0 \cdot 10^{11}$ and 0.2 V for $1.0 \cdot 10^{10}$ antiprotons in the ring). In addition, the potential well has a shallow minimum near the beam axis and the electric field $E_x$ of the beam decreases to zero near $x = 0$. Thus,

the estimated cross-field drift velocities will never be reached and Eqs. (79) and (80) cannot be applied [12]. Therefore, the longitudinal ion motion in quadrupoles is dominated by the mean thermal velocities in one direction $\bar{v}_{\parallel}$ and/or the longitudinal acceleration $a_s$ due to longitudinal electric fields $E_s$ of the antiproton beam.

### 8.6 $\vec{E} \times \vec{B}/B^2$ cross-field drift velocity in sextupole magnets

Here, we consider the $\vec{E} \times \vec{B}/B^2$ cross-field drift velocity in sextupole magnets which occurs due to the electric field of the antiproton beam when passing a sextupole magnet. We derive the equations in a similar way as in the preceding subsection. We assume a long bunch with a line density of the beam charges $\lambda$ as prepared by the barrier-bucket mode of operation. The transverse beam distribution is described by an elliptical bi-Gaussian distribution. Near the beam axis we have in first-order approximation the following expression for the electric field vector $\vec{E}$

$$\vec{E} = \frac{\lambda}{2\pi\epsilon_0} \frac{1}{\sigma_x + \sigma_y} \begin{pmatrix} x/\sigma_x \\ y/\sigma_y \\ 0 \end{pmatrix}. \tag{81}$$

The magnetic field vector $\vec{B}$ of the sextupole is given by

$$\vec{B} = g_s \begin{pmatrix} xy \\ (x^2 - y^2)/2 \\ 0 \end{pmatrix}. \tag{82}$$

Here, $g_s = \partial^2 B_y/\partial x^2 = \partial^2 B_x/\partial y^2 = 2\,B_0/a^2$ is the characteristic sextupole parameter as given by the pole-tip field $B_0$ and the pole-tip radius $a$. The resulting drift velocity is given by

$$\vec{v}_D = \frac{\vec{E} \times \vec{B}}{B^2} = \frac{\lambda}{2\pi\epsilon_0} \frac{1}{\sigma_x + \sigma_y} \frac{2}{g_s} \frac{1}{(x^2 + y^2)^2} \begin{pmatrix} 0 \\ 0 \\ \frac{x(x^2-y^2)}{\sigma_x} - \frac{2\,xy^2}{\sigma_y} \end{pmatrix}. \tag{83}$$

This equation may be written with $x = r\cos\varphi$, $y = r\sin\varphi$ and the unit vector $\vec{e}_z$ in $z$-direction

$$\vec{v}_D = \frac{\lambda}{2\pi\epsilon_0} \frac{1}{\sigma_x + \sigma_y} \frac{2}{g_s} \frac{1}{r} \left( \frac{\cos^3\varphi - \cos\varphi \sin^2\varphi}{\sigma_x} - \frac{2\,\cos\varphi \sin^2\varphi}{\sigma_y} \right) \vec{e}_z. \tag{84}$$

The ion drift velocities are directed in the longitudinal direction. Depending on the azimuth angle $\varphi$, the ions move in the forward or backward direction. As in the case of quadrupole magnets very high cross-field drift velocities would be reached. This is due to the fact that the magnitude of the magnetic field $B$ is very low near the beam axis. The corresponding kinetic energies would never be reached and Eqs. (83) and (84) cannot be applied [12]. Therefore, the longitudinal ion motion in sextupoles is also dominated by the mean thermal velocity $\bar{v}_{\parallel}$ and the longitudinal acceleration $a_s = q\,E_s/m$ due to the electric field of the beam.

## 9. Ion Motion in Solenoids

A speciality of the HESR ring are solenoids which are used for special purposes. (i) The electron cooler (EC) uses a 'cold' electron beam in order to cool the circulating antiproton beam. It consists of a long solenoid of about 24.0 m length which guides the electron beam along the axis of the antiproton beam. The solenoid field amounts to 0.2 T yielding a solenoid strength of 4.8 Tm. The electron beam is injected and extracted using merging modules which consist of dipole magnets and bent solenoids. (ii) In addition, there are two compensation solenoids of about 5.0 m length with a maximum solenoid field $B = 1.5$ T and a maximum solenoid strength of 7.5 Tm. They are located upstream and downstream near by the EC solenoid. (ii) In the region of the PANDA target the spectrometer magnet consists of a superconducting solenoid with external iron return yoke which allows to achieve a uniform longitudinal field of 2.0 T and keep enough space for detectors surrounding the interaction point. The maximum solenoid strength is about 7.0 Tm. (iv) In addition, there is one compensation solenoid of about 5.0 m length with a maximum solenoid field of 1.5 T and a maximum solenoid strength of 7.5 Tm in front of the target solenoid.

Here, we discuss first the mean thermal ion drift along the longitudinal magnetic fields of the EC-solenoid and the EC-compensation solenoids, and we estimate the resulting clearing times $T_c$. Then, we discuss the modified cyclotron motion and the magnetron motion of trapped ions in solenoids.

### 9.1 Cyclotron motion of trapped ions in solenoids

First, we discuss the situation in the beam-free time gaps. An ion which is created inside of a solenoid cannot escape in the transverse direction. The Lorentz force $q_i\vec{v}_i \times \vec{B}$ causes each ion to spiral around a magnetic field line. We assume that the ion has a certain thermal velocity with velocity components perpendicular and parallel to the magnetic field, $v_\perp$ and $v_\parallel$. In the transverse direction (i.e. in the plane perpendicular to the magnetic field direction) the ion performs a cyclotron motion around the magnetic field lines of the solenoid. In the longitudinal direction the ion moves freely along the magnetic field line of its guiding center. The cyclotron frequency $\omega_i$ depends on the magnetic field strength $B$, $\omega_i = q_i B/m_i$. The cyclotron radius $r_i$ depends on the transverse thermal velocity $v_\perp$, $r_i = (m_i v_\perp)/(q_i B)$. Typical values of $\omega_i$ and $r_i$ are listed in subsection 8.1 in the Tables 4 and 5.

### 9.2 Adiabatic motion of trapped ions in the fringe field of solenoids

Again, we discuss first the situation during the beam-free time gaps. Inside of the solenoid the magnetic field is nearly uniform yielding a nearly constant radius $r_i$ of the cyclotron motion around the magnetic field line and a constant distance $R_i$ of the guiding center from the solenoid axis. In the longitudinal direction ($z$-direction) the ion moves freely according to the start velocity $v_\parallel$ towards the fringe field of the solenoid.

The slow thermal ion motion can be considered as an adiabatic motion if the relative change of the magnetic field component $B_z$ is small during one cyclotron revolution period $T_i$, i.e. if

$$\left| \frac{v_z T_i}{B_z} \frac{\partial B_z}{\partial z} \right| = \left| \frac{2\pi m_i v_z}{q_i B_z^2} \frac{\partial B_z}{\partial z} \right| \ll 1. \tag{85}$$

The thermal velocities of the ions are so low that the adiabatic condition (85) is well fulfilled.

In the fringe field of the solenoid a slow ion (i.e. the guiding center of the ion) follows adiabatically the expanding field lines. Thus, the cyclotron radius $r_i$ and the distance $R_i$ of the guiding center from the solenoid axis increase according to

$$B_z r_i^2 = const, \quad B_z R_i^2 = const. \tag{86}$$

The last two equations follow directly from Busch's theorem, i.e. the magnetic flux through the cyclotron orbit with radius $r_i$ and the magnetic flux through a circle around the $z$-axis with radius $R_i$ are conserved. Thus, $r_i$ and $R_i$ increase in the fringe field like

$$r_i(z) = \sqrt{\frac{B_z(z_0)}{B_z(z)}} r_i(z_0), \quad R_i(z) = \sqrt{\frac{B_z(z_0)}{B_z(z)}} R_i(z_0). \tag{87}$$

Another consequence of the adiabatic motion is the fact that the velocity component $v_\perp$ perpendicular to the field line decreases slowly in the fringe field while the velocity component $v_\parallel$ parallel to the field line increases,

$$v_\perp(z) = \sqrt{\frac{B_z(z)}{B_z(z_0)}} v_\perp(z_0), \tag{88}$$

$$v_\parallel(z) = \sqrt{v^2 - v_\perp^2(z)}, \tag{89}$$

where $v^2 = v_\perp^2 + v_\parallel^2 = const$. The last equation is due to the conservation of kinetic energy.

### 9.3 Magnetron motion and modified cyclotron motion in solenoids due to the electric field of the beam

Ions which are created by the interaction of the antiproton beam with the residual gas molecules of the UHV vacuum cannot escape in the transverse direction due to the electric field $\vec{E}$ of the antiproton beam. There is an additional trapping effect in solenoids due to the cyclotron motion around the longitudinal magnetic field $\vec{B}$. This trapping effect is also present in the beam-free time gaps. But the situation is more complicated during the passage of the antiproton beam.

The superposition of the radial electric field $\vec{E}$ and the longitudinal magnetic field $\vec{B}$ yields a modified cyclotron motion and a slow motion around the solenoid axis. The latter motion is due to the $\vec{E} \times \vec{B}$ drift in azimuthal direction. It is called magnetron motion since it has been first observed during the development of the magnetron [28]. This motion has also been analyzed during the development of the Penning traps [29]. The modified cyclotron motion and the resulting magnetron motion is illustrated in the left panel of Fig. 12. The figure shows the projection of the ion motion upon the (x,y) plane. The cyclotron motion due to the longitudinal magnetic field is modified by the radial acceleration and deceleration. If the ion moves in the direction of the electric field it is accelerated and the radius of the trajectory is increased. If the ion moves against the direction of the electric field it is decelerated and the radius of the trajectory is decreased. As a consequence a mean drift velocity in the azimuthal direction arises. The rotational direction of the magnetron motion ($\omega_-$) is opposite to that of the cyclotron motion. This is due to the fact that the electric field $\vec{E}$ of the antiproton beam is directed radially towards the central axis. The resultant motion can be described by an epicycloid, i.e. the superposition of a slow circular magnetron motion with radius $r_-$ and angular velocity $\omega_-$ and a modified cyclotron motion with radius $r_+$ and angular velocity $\omega_+$, see right panel of Fig. 12.

The fast cyclotron motion with a small radius $r_+$ is carried along by the slow magnetron motion with a large radius $r_-$. As to the equations of motion, we refer to review articles by Brown and Gabrielse [30] and Blaum [31]. The detailed solution of the equations of motion is presented in the Appendix.

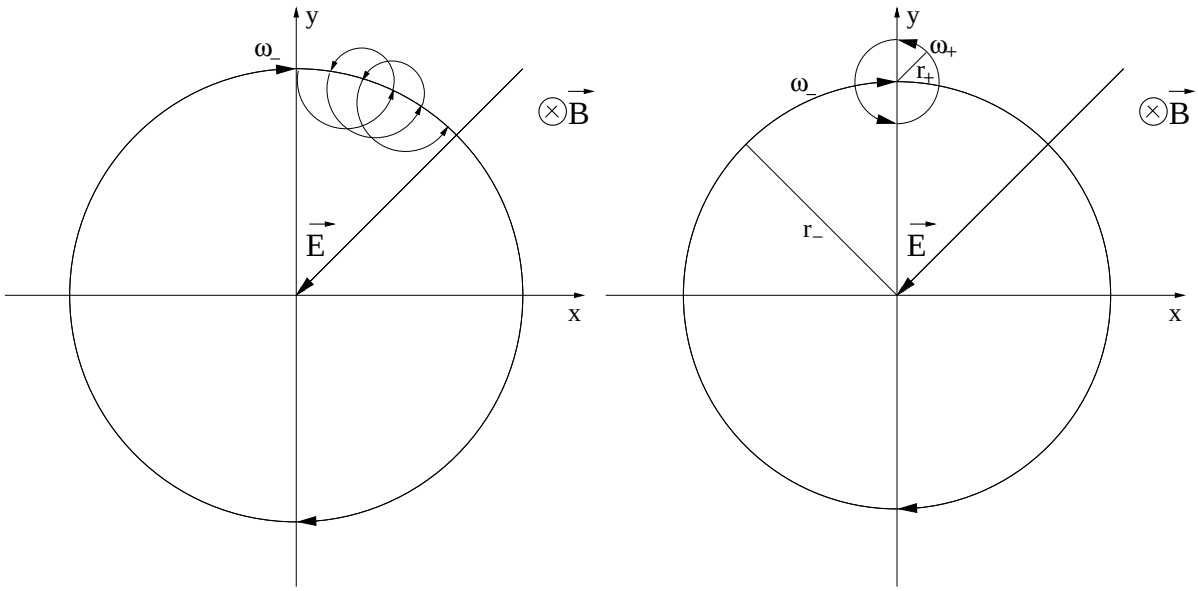


Fig. 12: Left: Illustration of the motion of trapped ions in a solenoid. The cyclotron motion is modified by the acceleration and deceleration due to the electric field $\vec{E}$ of the antiproton beam. The resulting magnetron motion ($\omega_-$) is opposite to the cyclotron motion ($\omega_+$). Right: The motion can be described as an epicycloid that is the superposition of a slow circular magnetron motion with radius $r_-$ and angular velocity $\omega_-$ and a modified cyclotron motion with radius $r_+$ and angular velocity $\omega_+$.

Here, we sketch the solution. We use a Cartesian coordinate system $(x, y.z)$ which corresponds to the standard coordinate system $(x, y, s)$ of accelerator physics. The $z$-axis is the central axis of the solenoid. The ion motion is described radially by $\vec{\rho} = (x, y)$ and axially by $z$. The equations of motion read

$$m\ddot{\vec{\rho}} = q(\vec{E}_\rho + \dot{\vec{\rho}} \times \vec{B}), \tag{90}$$

$$m\ddot{z} = qE_z. \tag{91}$$

We assume a linear approximation of the radially attractive electric field

$$\vec{E}_\rho = -E_0\vec{\rho}. \tag{92}$$

We note that $E_0 = |\lambda|/(2\pi\epsilon_0 a^2)$ for a round beam with constant density within the radius $a$, see Eq. 5. We introduce the angular frequency $\omega_b = \sqrt{qE_0/m}$ in order to take the electric field strength into account,

$$\omega_b^2 = \frac{q}{m}\frac{|\lambda|}{2\pi\epsilon_0}\frac{1}{a^2}. \tag{93}$$

We assume that the magnetic field is oriented in the negative $z$-direction

$$\vec{B} = -(0, 0, B). \tag{94}$$

The magnetic field strength is represented by the angular frequency $\omega_c = qB/m$ of the free cyclotron motion (i.e. for $\vec{E}_\rho = 0$). The solution of the radial equation (90) may be written

$$\vec{\rho} = \vec{r}_+ + \vec{r}_-, \tag{95}$$

$$\vec{r}_+ = r_+(\cos(\omega_+ t + \alpha_+), \sin(\omega_+ t + \alpha_+)), \tag{96}$$

$$\vec{r}_- = r_-(\cos(\omega_- t + \alpha_-), \sin(\omega_- t + \alpha_-)), \tag{97}$$

where

$$\omega_+ = \frac{\omega_c}{2} + \sqrt{\left(\frac{\omega_c}{2}\right)^2 + \omega_b^2}, \tag{98}$$

$$\omega_- = \frac{\omega_c}{2} - \sqrt{\left(\frac{\omega_c}{2}\right)^2 + \omega_b^2}. \tag{99}$$

The radial motion of an ion is characterized by the superposition of two motions: (i) the modified cyclotron motion with angular frequency $\omega_+$ and radius $r_+$ and (ii) the magnetron motion with angular frequency $\omega_-$ and radius $r_-$. The angular velocity $\omega_+$ is positive whereas the angular velocity $\omega_-$ is negative. This is due to the radially attractive electric potential, see Fig. 12. The parameters $r_+$, $r_-$, $\alpha_+$ and $\alpha_-$ are constants of integration determined by the initial position and velocity of the ion in the moment of ionization.

It is interesting to evaluate the velocity $v_- = r_-\omega_-$ of the magnetron motion. If $\omega_b^2 \ll (\omega_c/2)^2$ we get

$$r_-\,\omega_- = -r_-\,\frac{\omega_b^2}{\omega_c} = -r_-\frac{E_0}{B} = -\frac{|\vec{E}|}{B} = \frac{\vec{E}\times\vec{B}}{B^2}. \tag{100}$$

That means, the velocity $v_-$ of the magnetron motion is given by the $\vec{E}\times\vec{B}$ cross-field velocity.

### 9.4 Magnetron motion and modified cyclotron motion in the fringe field of solenoids

As stated in the preceding subsection, the radial motion of an ion is characterized by the superposition of the modified cyclotron motion with angular frequency $\omega_+$ and radius $r_+$ and the slow magnetron motion around the central axis with angular frequency $\omega_-$ and radius $r_-$. The radius $r_+$ corresponds to the radius $r_i$ and the radius $r_-$ corresponds to the radius $R_i$ introduced in subsection 9.2. The radius $r_-$ denotes the distance of the center of the cyclotron motion from the symmetry axis $z$ of the solenoid.

The motion of trapped ions in the fringe field of a solenoid can be considered as an adiabatic motion since the longitudinal velocity of the trapped ions is very low and the relative change of the magnetic field component $B_z$ is very small during one cyclotron revolution period $T_+ = 2\pi/\omega_+$ of the modified cyclotron motion. Therefore, the radii $r_+$ and $r_-$ increase like

$$r_\pm(z) = \sqrt{\frac{B_z(z_0)}{B_z(z)}}\,r_\pm(z_0) \tag{101}$$

at the entrance and exit of a solenoid due to the decreasing magnetic field strength $B_z(z)$.

Simultaneously, the modified cyclotron frequency $\omega_+$ and the magnetron frequency $\omega_-$ decrease slowly in the fringe field of the solenoid. This is due to the fact that the characteristic quantities $\omega_c = qB/m$ and $\omega_b^2$ decrease in the fringe field, see Eqs. (98) and (99). Concerning

$\omega_b^2$, we know that the electric field strength $|E_\rho|$ decreases as $1/\rho$ outside of the antiproton beam. Therefore, the electric field outside of the antiproton beam may be written

$$\vec{E} = \frac{\lambda}{2\pi\epsilon_0} \frac{\vec{r}_+ + \vec{r}_-}{(\vec{r}_+ + \vec{r}_-)^2} \approx \frac{\lambda}{2\pi\epsilon_0} \frac{\vec{r}_+ + \vec{r}_-}{r_-^2}. \tag{102}$$

This approximation is possible if $r_+ \ll r_-$. Thus, the characteristic quantity $\omega_b^2$ decreases in the fringe field and we get instead of Eq. (93)

$$\omega_b^2 = \frac{q}{m} \frac{|\lambda|}{2\pi\epsilon_0} \frac{1}{r_-^2}. \tag{103}$$

Summarizing, the radii $r_+$ and $r_-$ increase and the modified cyclotron frequency $\omega_+$ and the magnetron frequency $\omega_-$ decrease slowly in the fringe field of the solenoid.

### 9.5 Fringe field of solenoids

The inside magnetic field of a long solenoid is nearly uniform. The field strength $B_z$ along the axis may be written with $B_0 = \mu_0 N I$

$$B_z(z) = \frac{B_0}{2} \left( \frac{L+z}{\sqrt{(L+z)^2 + a^2}} - \frac{z}{\sqrt{z^2 + a^2}} \right). \tag{104}$$

Here, $\mu_0$ is the magnetic field constant, $N$ the number of windings per meter, $I$ the current, $L$ the length, $a$ the radius of the solenoid coil and $z$ the longitudinal position with $z = 0$ at the exit of the solenoid. Thus, the extent of the fringe field depends on the radius $a$. We have for instance $B_z = 0.985\, B_0$ at $z = -4\, a$ and $B_z = 0.015\, B_0$ at $z = +4\, a$.

The PANDA spectrometer solenoid [32] consists of three large coils in a large iron yoke. The inner radius of the coils amounts to 0.930 m and the total coil length amounts to about 2.8 m. The magnetic field distribution has been calculated with the program TOSCA [32]. The solenoid strength amounts to about 7.0 Tm. The longitudinal field distribution along the solenoid axis can be approximated using a trapezoidal model with a minor basis of 1.5 m and a major basis (at zero field) of about 5.5 m. The minor basis, i.e. the central part, exhibits a highly uniform magnetic field $B_0 = 2.0$ T. It is about 1.5 m long. The upstream and downstream fringe fields extend to about $l = 2.0$ m. The magnetic field $B_z(z)$ in the fringe field region $0 \leq |z| \leq l$ can be approximated using

$$B_z(z) \approx B_0 \left( 1 - \frac{|z|}{l} \right), \quad 0 \leq |z| \leq l. \tag{105}$$

The total length of the trapezoidal field distribution amounts to about 5.5 m.

The equations (104) and (105) together with (101) may be used in order to calculate the increasing radii $r_+$ and $r_-$ of trapped ions at the entrance and exit of the solenoids.

### 9.6 Mean thermal ion drift and clearing times $T_c$ in solenoids

In the longitudinal direction, the ions move freely along the magnetic field lines of the solenoids. Here, we estimate the resulting clearing times $T_c$ if the ions are moving with their mean thermal velocity in the longitudinal direction and are captured by clearing electrodes at the entrance and

exit of the solenoids. These estimates are only valid if the longitudinal electric fields $E_s$ of the beam are negligibly small. Such a situation occurs for $1.0 \cdot 10^{11}$ antiprotons in the region of the EC-solenoid and the EC-compensation solenoids, see $E_s$ in Fig. 8 between $s = 190$ m and $s = 250$ m. For $1.0 \cdot 10^{10}$ antiprotons, the longitudinal electric field components of the beam are negligibly small everywhere in the ring. The mean thermal velocity in one direction, $\bar{v}_{\|}$, amounts to 889 m/s for $H_2^+$ ions and 238 m/s for $CO^+$ ions. We assume as mean path length the half length of a solenoid, i.e. $\bar{l} = L/2 = 12$ m for the electron cooler solenoid and $\bar{l} = L/2 = 2.5$ m for the compensation solenoids The resulting mean clearing times are given by

$$T_c = \bar{l}/\bar{v}_{\|}. \tag{106}$$

They are listed in Table 7 for various molecules.

Table 7: Mean thermal ion drift velocity $\bar{v}_{\|}$ in one direction and clearing times $T_c$ in solenoids.

| Molecule | A | $v_{\|}$ (m/s) | $T_c$ (s), EC solenoid | $T_c$ (s), compensation solenoid |
|---|---|---|---|---|
| H | 1 | $1.2{\cdot}10^3$ | $10{\cdot}10^{-3}$ | $2.1{\cdot}10^{-3}$ |
| $H_2$ | 2 | $8.9{\cdot}10^2$ | $13{\cdot}10^{-3}$ | $2.8{\cdot}10^{-3}$ |
| $CH_4$ | 16 | $3.1{\cdot}10^2$ | $37{\cdot}10^{-3}$ | $7.9{\cdot}10^{-3}$ |
| $H_2O$ | 18 | $3.0{\cdot}10^2$ | $40{\cdot}10^{-3}$ | $8.3{\cdot}10^{-3}$ |
| $CO/N_2$ | 28 | $2.4{\cdot}10^2$ | $50{\cdot}10^{-3}$ | $10{\cdot}10^{-3}$ |
| $CO_2$ | 44 | $1.9{\cdot}10^2$ | $63{\cdot}10^{-3}$ | $13{\cdot}10^{-3}$ |

## 10. Ion Clearing Using Clearing Electrodes

### 10.1 Clearing electrodes

Since the energy transfer is negligibly small in ionization processes ions are produced with a kinetic energy similar to the thermal energy which is about 0.04 eV at 300 K. The thermal rms velocity amounts to 1900 m/s for $H_2^+$ ions and 520 m/s for $CO^+$ ions. Therefore the positive ions are trapped in the negative potential well of the antiproton beam which is in the order of -2 V for $1.0 \cdot 10^{11}$ antiprotons (see Fig. 6). The ions start to perform transverse oscillations in the potential well. In addition they are accelerated longitudinally in the direction to the potential minima. We mention that the typical depth of the potential well is only -0.25 V for $1.0 \cdot 10^{10}$ antiprotons.

The positive ions can be extracted by clearing electrodes if the external electric fields are larger than the electric fields created by the antiproton beam, see Fig. 7. Thus, isolated electrodes near the inner surface of the beam pipe (inner diameter: 89 mm) providing sufficiently large electric fields of more than 500 V/m can be used in order to extract the produced ions. For instance, clearing electrodes mounted on the inner surface of a beam pipe yield electric fields of about 2250 V/m with a clearing voltage of -200 V. The electrodes of the beam position monitors in the ring can also be used to extract the positive ions out of the antiproton beam.

The number of clearing electrodes should be as large as possible. Ideal locations are the minima of the beam potential which act as trapping pockets. In principle it is mandatory to locate clearing electrodes near the potential minima in order to avoid trapping pockets. Ions which are produced inside the bending magnets can be extracted with electric fields in the vertical direction, i.e. in the direction of the magnetic field lines, see Subsect. 10.5. It is also possible to extract the ions in the longitudinal direction using the $\vec{E} \times \vec{B}/B^2$ cross-field drift velocity, see Subsects. 10.4 and 10.6.

Clearing electrodes can also provide valuable diagnostic information if the clearing current on each electrode can be measured using fast picoamperemeters [16]. For instance such measurements yield a relatively good measurement of the local neutralization time $T_n(s)$ which is equivalent to the so-called production time $T_p(s)$ and depends on the local pressure $p(s)$. Switching on and off of certain clearing electrodes or groups of clearing electrodes allows to study the local effects of trapped ions.

Finally, we mention that the closed orbit distortions by the transverse electric fields of the clearing electrodes are negligibly small.

### 10.2 Ion clearing in straight sections by mean thermal velocities

For $1.0 \cdot 10^{10}$ stored antiprotons the longitudinal electric fields $E_s$ are so weak that the ion drift is dominated by the mean thermal velocity $\bar{v}_\parallel$ in the longitudinal direction. We assume that the distance $L$ between neighbouring clearing electrodes in the straight sections amounts to about 5 m. This distance corresponds to the effective length of the compensation solenoids. We estimate the mean clearing time $T_c$ assuming the mean thermal velocity $\bar{v}_\parallel$ of the ions (see Table 3) as a typical mean drift velocity. The resulting mean clearing time $T_c$ reads

$$T_c = \frac{L}{2\,\bar{v}_\parallel}. \tag{107}$$

We note that similar estimates are obtained if one takes the longitudinal acceleration $a_s = qE_s/m$ due to the longitudinal electric field components of the beam into account, see next

subsection. The resulting beam neutralization $\eta = 0.9\,T_c/T_p$ depends on the production time $T_p$. The production times $T_p$ and the resulting neutralizations $\eta$ are estimated for $H_2^+$ and $CO^+$ ions assuming different partial pressures, see Tables 8-10. We mention that the UHV pressure of the HESR ring amounts to about $1.0 \cdot 10^{-9}$ mbar. The resulting estimates of the neutralization $\eta$ in the full HESR ring are shown in Figs. 15, 16, 19 and 20.

Table 8: Mean thermal velocity $|\bar{v}_\parallel|$, mean clearing time $T_c$ ($L = 5$ m), production time $T_p$ and neutralization $\eta$ for $H_2^+$ ions assuming a partial $H_2$ pressure of $1.0 \cdot 10^{-9}$ mbar.

| $p$ GeV/c | $\lvert\bar{v}_\parallel\rvert$ (m/s) | $T_c$ (s) | $T_p$ (s) | $\eta$ |
|---|---|---|---|---|
| 1.5 | 889 | 0.00281 | 7.38 | $3.43 \cdot 10^{-4}$ |
| 3.825 | 889 | 0.00281 | 7.44 | $3.40 \cdot 10^{-4}$ |
| 8.889 | 889 | 0.00281 | 6.95 | $3.64 \cdot 10^{-4}$ |
| 15.0 | 889 | 0.00281 | 6.38 | $3.96 \cdot 10^{-4}$ |

Table 9: Mean thermal velocity $|\bar{v}_\parallel|$, mean clearing time $T_c$ ($L = 5$ m), production time $T_p$ and neutralization $\eta$ for $H_2^+$ ions assuming a partial $H_2$ pressure of $0.8 \cdot 10^{-9}$ mbar.

| $p$ GeV/c | $\lvert\bar{v}_\parallel\rvert$ (m/s) | $T_c$ (s) | $T_p$ (s) | $\eta$ |
|---|---|---|---|---|
| 1.5 | 889 | 0.00281 | 9.22 | $2.74 \cdot 10^{-4}$ |
| 3.825 | 889 | 0.00281 | 9.29 | $2.72 \cdot 10^{-4}$ |
| 8.889 | 889 | 0.00281 | 8.69 | $2.91 \cdot 10^{-4}$ |
| 15.0 | 889 | 0.00281 | 7.98 | $3.17 \cdot 10^{-4}$ |

Table 10: Mean thermal velocity $|\bar{v}_\parallel|$, mean clearing time $T_c$ ($L = 5$ m), production time $T_p$ and neutralization $\eta$ for $CO^+$ ions assuming a partial CO pressure of $0.2 \cdot 10^{-9}$ mbar.

| $p$ GeV/c | $\lvert\bar{v}_\parallel\rvert$ (m/s) | $T_c$ (s) | $T_p$ (s) | $\eta$ |
|---|---|---|---|---|
| 1.5 | 237 | 0.0106 | 8.50 | $1.12 \cdot 10^{-3}$ |
| 3.825 | 237 | 0.0106 | 8.33 | $1.12 \cdot 10^{-3}$ |
| 8.889 | 237 | 0.0106 | 7.45 | $1.12 \cdot 10^{-3}$ |
| 15.0 | 237 | 0.0106 | 6.92 | $1.37 \cdot 10^{-3}$ |

### 10.3 Ion clearing in straight sections by longitudinal acceleration

For $1.0 \cdot 10^{11}$ antiprotons the longitudinal acceleration $a_s$ of ions by the longitudinal electric field component $E_s$ are so large that they must be taken into account in the estimates of the clearing time $T_c$. The produced positive ions are accelerated towards the clearing electrodes due to the longitudinal gradient of the beam potential, i.e. the longitudinal electric field $E_s$, see Fig. 8. This accelerated motion occurs in the region of drift spaces, quadrupole magnets, sextupole magnets and solenoids. However, an accelerated motion does not occur in the region of dipole magnets. This is due to the cyclotron motion around the magnetic field lines and the resulting $\vec{E} \times \vec{B}$ cross-field drift velocity which occurs in crossed electric and magnetic fields, see Sect. 8..

The longitudinal acceleration $a_s$ of a singly charged ion is given by

$$a_s = \frac{e}{m} E_s. \tag{108}$$

Here, $m$ is the mass of the ion. The resulting acceleration for $H_2^+$ ions is shown in Fig. 13. Outside of the PANDA target region the acceleration varies between $10^4$ m/s$^2$ and $5 \cdot 10^6$ m/s$^2$.

Here, we assume that the ion clearing is dominated by the longitudinal acceleration $a_s$ and we neglect the thermal velocities of the ions. An ion which is produced in a drift space at a certain position $x, y, s$ makes transverse oscillations inside the potential well and is accelerated in the longitudinal direction by the longitudinal electric field component $E_s$. It moves inside the potential well of the antiproton beam until it sees the strong transverse electric field of a clearing electrode. The mean clearing time $T_c$ is given by the distance $L$ between neighbouring clearing electrodes and the longitudinal acceleration $a_s$. Assuming constant longitudinal acceleration yields a mean clearing time

$$T_c = \sqrt{\frac{8}{9}\frac{L}{a_s}} \approx \sqrt{\frac{L}{a_s}}. \tag{109}$$

We assume a distance of $L = 5$ m between neighbouring clearing electrodes[3]. The resulting estimates of the neutralization $\eta$ in the full HESR ring are shown in Figs. 17, 18, 21 and 22.

We note that these estimates neglect the dependence of $E_s$ on the transverse coordinates $(x, y)$. The longitudinal field component $E_s$ is weaker near the beam edge than in the center of the beam. However, the potential depth and therewith the field component $E_s$ decrease rather weakly with increasing transversal distance $r = \sqrt{x^2 + y^2}$ from the beam axis. For instance, if the beam pipe radius $r_c$ is about $10\sqrt{\sigma_x^2 + \sigma_y^2}$ the reduction is only 25 % near the beam edge $r = 2\sqrt{\sigma_x^2 + \sigma_y^2}$.

We mention that the longitudinal acceleration near the PANDA target solenoid cannot be used for trapped ion clearing. The direction of the longitudinal electric field is such that all ions from upstream and downstream are accelerated towards the beam waist at the target point. The peak-like structures of $a_s$ near the PANDA target are due to the sudden changes of the longitudinal electric fields $E_s$ as discussed in subsection 3.3. The neutralization near the PANDA target will be discussed separately in section 15..

[3]It is foreseen to use also the electrodes of the beam position monitors BPM as clearing electrodes. There are about 50 BPM's in the ring.

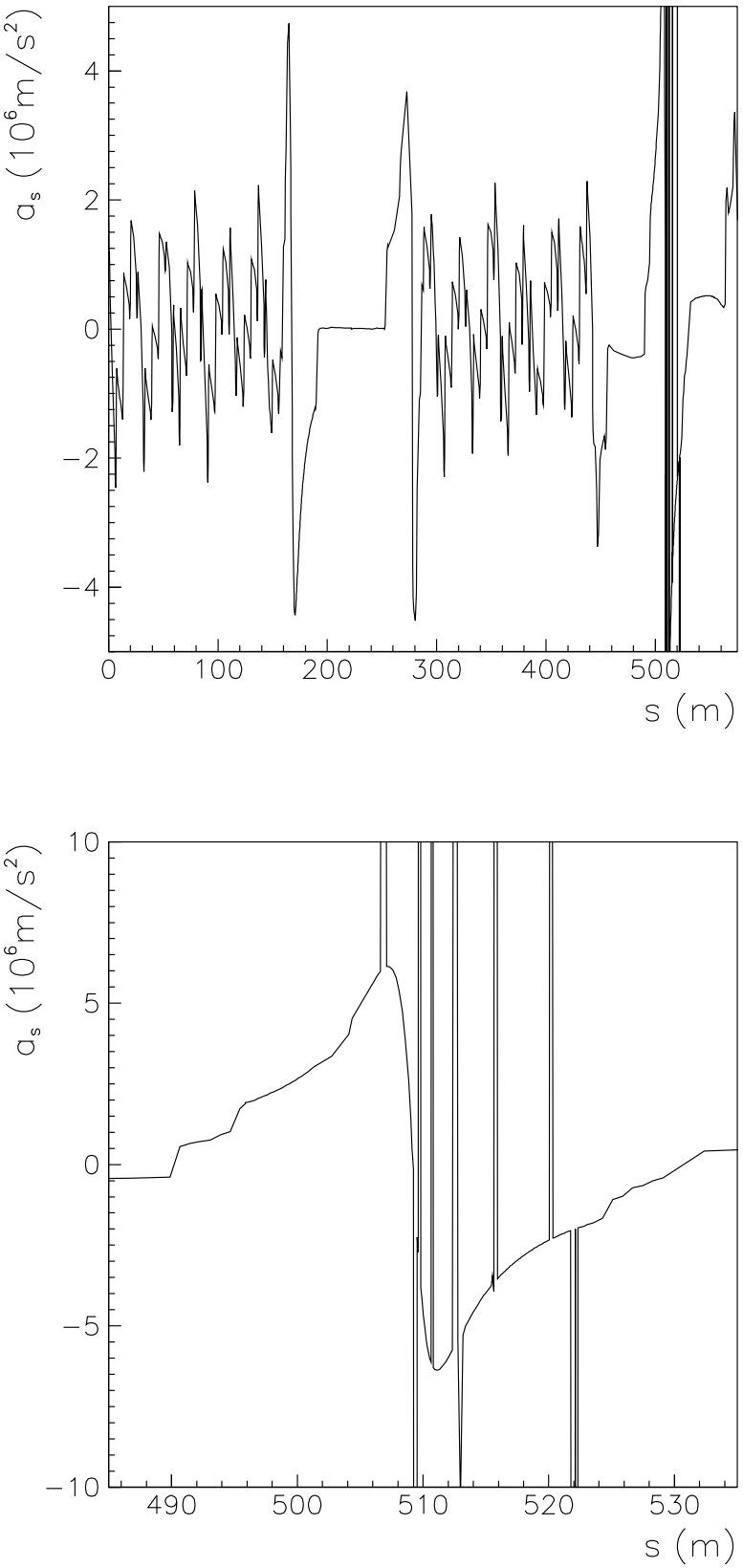


Fig. 13: Estimates of the longitudinal acceleration $a_s(s)$ of $H_2^+$ ions assuming the standard optics, $L_1 = 0.9C$, $p_{\bar{p}} = 15$ GeV/c and $N_{\bar{p}} = 1.0 \cdot 10^{11}$. The modification of the beam potential by the neutralization $\eta$ is neglected. Top: the complete HESR ring from $s = 0$ m to $s = 575$ m. Bottom: the PANDA target region from $s = 485$ m to $s = 535$ m. The peak-like structures near the PANDA target are due to sudden changes of the inner radius of the beam pipe.

### 10.4 Ion clearing in dipole magnets by mean cross-field drift velocities

We first discuss the possibility to use clearing electrodes at the entrance and exit of dipole magnets. There is a cross-field drift velocity $v_D = E_x/B_y$ in the longitudinal direction (see Subsection 8.2) which can be used in order to guide trapped ions to the entrance and exit of the dipole magnets. This cross-field drift velocity is due to the transverse electric field component $E_x$ of the beam and the transverse magnetic field component $B_y$. The concurrent cross-field drift velocity components $v_x = E_s/B_y$ due to longitudinal electric field components of the beam are neglected. On average, the longitudinal field components $E_s$ are very small in comparison to the transverse field components $E_x$, see Figs. 7 and 8.

We note that the cross-field drift velocities $\vec{v}_D = \vec{E} \times \vec{B}/B^2$ for ions created on the left side of the beam axis are negative, i.e. they are directed in the backward direction. Ions created on the right side of the beam axis exhibit positive drift velocities, i.e. they drift in the forward direction. The mean cross-field drift velocities $|\bar{v}_D|$ on either side are evaluated assuming Gaussian beam distributions, see Subsection 8.2.

In Tables 11-13, we list the mean cross-field drift velocity $|\bar{v}_D|$, the mean clearing time $T_c$ for a mean drift of $L/2 = 2.25$ m (we assume that the clearing electrodes are located in the 0.3 m long drift spaces at the entrance and exit of the dipole magnets), the production time $T_p$ for $H_2^+$ and $CO^+$ ions assuming different partial pressures and the resulting neutralization $\eta = (L_1/C)(T_c/T_p) = 0.9(T_c/T_p)$ for four beam momenta. In Table 11, we list the results for $H_2^+$ ions assuming a partial pressure of $1.0 \cdot 10^{-9}$ mbar for $H_2$ molecules, in Table 12, we list the results for $H_2^+$ ions assuming a partial pressure of $0.8 \cdot 10^{-9}$ mbar for $H_2$ molecules and in Table 13 for $CO^+$ ions assuming a partial pressure of $0.2 \cdot 10^{-9}$ mbar for CO molecules. We mention that a CO molecule content of about 10-20 % is always present in the UHV of storage rings.

We note that the mean cross-field drift velocity $|\bar{v}_D|$ is rather small. This is due to the fact that the electric field $E_x$ and therewith the cross-field drift velocity $v_D$ drops down to zero at the beam center. Therefore, ions created near the beam center are practically not cleared and the resulting mean cross-field drift velocities are rather low in dipole magnets when averaged over the Gaussian beam profile. As a consequence, the resulting beam neutralization is rather high (between 0.9 % at 1.5 GeV/c and 3.4 % at 15 GeV/c assuming $1.0 \cdot 10^{11}$ antiprotons and a partial $H_2$ pressure of $0.8 \cdot 10^{-9}$ mbar and a partial CO pressure of $0.2 \cdot 10^{-9}$ mbar). The situation is yet worse for $1.0 \cdot 10^{10}$ antiprotons. The mean cross-field drift velocities for $1.0 \cdot 10^{10}$ antiprotons are by a factor of $10^{3/5}$=3.98 lesser[4] and the mean clearing times $T_c$ and the resulting neutralization $\eta$ are by a factor of $10^{3/5}$=3.98 larger than the values listed in Tables 11 - 13. Such neutralization levels are dangerous in view of possible coherent instabilities. In this context, it should be noted that 44 dipole magnets are installed in the HESR ring. The total length of 44 dipole magnets amounts to 184.8 m which is about one third of the circumference. Therefore, we recommend additional measures in order to reduce substantially the neutralization in dipole magnets, see Subsects. 10.5, 10.6 and 10.7.

We first discuss ion clearing by vertical electric fields $E_y$, see Subsect. 10.5. The idea is to use continuous clearing electrodes in the beam pipe in order to extract the ions along the magnetic field lines in the vertical direction. Another technique could be to provide horizontal electric fields $E_x$ in the beam pipe. The resulting cross-field drift velocity $E_x/B_y$ could be used in order to extract the ions in the longitudinal direction, see Subsect. 10.6. A third possibility

[4] $\lambda \propto N_{\bar{p}}$, $\sigma \propto N_{\bar{p}}^{2/5}$, $|\bar{v}_D| \propto N_{\bar{p}}^{3/5}$, see Subsect. 8.3.

could be to improve the ultra-high vacuum (UHV) substantially, see Subsect. 10.7.

Table 11: Mean cross-field drift velocity $|\bar{v}_D|$, mean clearing time $T_c$, production time $T_p$ and neutralization $\eta$ for $H_2^+$ ions assuming a partial $H_2$ pressure of $1.0 \cdot 10^{-9}$ mbar ($N_{\bar{p}} = 1.0 \cdot 10^{11}$).

| $p$ GeV/c | $\|\bar{v}_D\|$ (m/s) | $T_c$ (s) | $T_p$ (s) | $\eta$ |
|---|---|---|---|---|
| 1.5 | 51.3 | 0.0439 | 7.38 | 0.00535 |
| 3.825 | 32.1 | 0.0701 | 7.44 | 0.00848 |
| 8.889 | 21.1 | 0.107 | 6.95 | 0.0139 |
| 15.0 | 16.2 | 0.139 | 6.38 | 0.0196 |

Table 12: Mean cross-field drift velocity $|\bar{v}_D|$, mean clearing time $T_c$, production time $T_p$ and neutralization $\eta$ for $H_2^+$ ions assuming a partial $H_2$ pressure of $0.8 \cdot 10^{-9}$ mbar ($N_{\bar{p}} = 1.0 \cdot 10^{11}$).

| $p$ GeV/c | $\|\bar{v}_D\|$ (m/s) | $T_c$ (s) | $T_p$ (s) | $\eta$ |
|---|---|---|---|---|
| 1.5 | 51.3 | 0.0439 | 9.22 | 0.00429 |
| 3.825 | 32.1 | 0.0701 | 9.29 | 0.00679 |
| 8.889 | 21.1 | 0.107 | 8.69 | 0.0111 |
| 15.0 | 16.2 | 0.139 | 7.98 | 0.0157 |

Table 13: Mean cross-field drift velocity $|\bar{v}_D|$, mean clearing time $T_c$, production time $T_p$ and neutralization $\eta$ for $CO^+$ ions assuming a partial CO pressure of $0.2 \cdot 10^{-9}$ mbar ($N_{\bar{p}} = 1.0 \cdot 10^{11}$).

| $p$ GeV/c | $\|\bar{v}_D\|$ (m/s) | $T_c$ (s) | $T_p$ (s) | $\eta$ |
|---|---|---|---|---|
| 1.5 | 51.3 | 0.0439 | 8.50 | 0.00464 |
| 3.825 | 32.1 | 0.0701 | 8.33 | 0.00757 |
| 8.889 | 21.1 | 0.107 | 7.45 | 0.0129 |
| 15.0 | 16.2 | 0.139 | 6.92 | 0.0181 |

### 10.5 Ion clearing in dipole magnets by vertical electric fields

The optimum solution for dipole magnets are continuous clearing electrodes. In dipole magnets, only vertical electric fields with field components $E_y$ along the magnetic field lines can be used in order to accelerate the trapped ions towards clearing electrodes. Continuous band electrodes could be mounted together with a thin insulator inside the beam pipe. An ideal insulator would be a 100 $\mu$m thick layer of vitreous enamel ('Emaille'). Electrode potentials of $\pm 100$ V yield an electric field of about 2250 V/m in a beam pipe of 89 mm diameter.

The positive ions which are created inside the beam envelopes are immediately accelerated towards the clearing electrode. For $H_2^+$ ions the resulting acceleration is

$$a_y = \frac{eE_y}{m} = 1.08 \cdot 10^{11}\ \mathrm{m/s^2}. \tag{110}$$

Estimating the mean clearing time $T_c$ we assume a mean flight path length of $3\sigma_y$. That means ions which are created in the beam center $y = 0$ reach the beam edge at $y = 3\sigma_y$. This assumption yields

$$T_c \approx \sqrt{\frac{6\sigma_y}{a_y}}. \tag{111}$$

The resulting clearing times $T_c(s)$ are below $1.0 \cdot 10^{-6}$ s and the neutralization $\eta$ near $1.0 \cdot 10^{-7}$, see Figs. 15 - 22.

### 10.6 Ion clearing in dipole magnets by horizontal electric fields

Another technique has been suggested by Rudolf Maier [33] in order to remove trapped ions in dipole magnets. He suggested to use elliptic beam pipes instead of round beam pipes in the region of dipole magnets. Using this technique one has sufficient space for electrodes providing electric fields $E_x$ in the horizontal direction. Electric fields $E_x$ of about 3400 V/m in combination with the vertical magnetic field $B_y$ between 0.17 T and 1.7 T yield cross-field drift velocities $v_s = E_x/B_y$ between 20000 m/s and 2000 m/s. The total length of a dipole magnet amounts to 4.2 m. The clearing electrodes are located at the entrance and exit of the dipole magnets. Assuming that the ions travel a mean drift distance of about $L/2 = 2.25$ m yields clearing times $T_c = (L/2)/|\bar{v}_D|$ between 0.113 ms and 1.13 ms, and neutralizations $\eta$ of order of magnitude $10^{-4}$ and below, see Tables 14-16.

Table 14: Cross-field drift velocity $|\bar{v}_D|$ assuming $E_x = 3.4$ kV/m, mean clearing time $T_c$, production time $T_p$ and neutralization $\eta$ for $H_2^+$ ions assuming a partial $H_2$ pressure of $1.0 \cdot 10^{-9}$ mbar.

| $p$ GeV/c | $\|\bar{v}_D\|$ (m/s) | $T_c$ (ms) | $T_p$ (s) | $\eta$ |
|---|---|---|---|---|
| 1.5 | 20000 | 0.113 | 7.38 | $1.59 \cdot 10^{-5}$ |
| 3.825 | 7843 | 0.287 | 7.44 | $3.86 \cdot 10^{-5}$ |
| 8.889 | 3375 | 0.667 | 6.95 | $8.64 \cdot 10^{-5}$ |
| 15.0 | 2000 | 1.13 | 6.38 | $1.59 \cdot 10^{-4}$ |

Table 15: Cross-field drift velocity $|\bar{v}_D|$ assuming$E_x = 3.4$ kV/m, mean clearing time $T_c$, production time $T_p$ and neutralization $\eta$ for $H_2^+$ ions assuming a partial $H_2$ pressure of $0.8 \cdot 10^{-9}$ mbar ($N_{\bar{p}} = 1.0 \cdot 10^{11}$).

| $p$ GeV/c | $\|\bar{v}_D\|$ (m/s) | $T_c$ (ms) | $T_p$ (s) | $\eta$ |
|---|---|---|---|---|
| 1.5 | 20000 | 0.113 | 9.22 | $1.27 \cdot 10^{-5}$ |
| 3.825 | 7843 | 0.287 | 9.29 | $3.09 \cdot 10^{-5}$ |
| 8.889 | 3375 | 0.667 | 8.69 | $6.91 \cdot 10^{-5}$ |
| 15.0 | 2000 | 1.13 | 7.98 | $1.27 \cdot 10^{-4}$ |

Table 16: Cross-field drift velocity $|\bar{v}_D|$ assuming $E_x = 3.4$ kV/m, mean clearing time $T_c$, production time $T_p$ and neutralization $\eta$ for $CO^+$ ions assuming a partial CO pressure of $0.2 \cdot 10^{-9}$ mbar ($N_{\bar{p}} = 1.0 \cdot 10^{11}$).

| $p$ GeV/c | $\|\bar{v}_D\|$ (m/s) | $T_c$ (ms) | $T_p$ (s) | $\eta$ |
|---|---|---|---|---|
| 1.5 | 20000 | 0.113 | 8.50 | $1.20 \cdot 10^{-5}$ |
| 3.825 | 7843 | 0.287 | 8.33 | $3.10 \cdot 10^{-05}$ |
| 8.889 | 3375 | 0.667 | 7.45 | $8.06 \cdot 10^{-5}$ |
| 15.0 | 2000 | 1.13 | 6.92 | $1.47 \cdot 10^{-4}$ |

### 10.7 UHV upgrade in dipole magnets

Another technique would be to upgrade the UHV vacuum substantially. First vacuum tests with a setup similar to the planned vacuum system near the dipole magnets (4.2 m long beam pipes of 89 mm diameter with vacuum pumps at the entrance and exit of the dipole magnets) showed that pressures below $1.0 \cdot 10^{-10}$ mbar can be achieved without heating, i.e. without baking out the beam pipe. A further substantial improvement of the UHV (order of magnitude improvement) can be achieved by baking out the beam pipes. To this end bake-out jackets must be installed from the start. The baked UHV vacuum system at the CERN Antiproton Accelerator was operated at pressures of about $1.3 \cdot 10^{-11}$ mbar.

Lowering the UHV vacuum pressure from $1.0 \cdot 10^{-9}$ mbar to about $1.0 \cdot 10^{-11}$ mbar has the advantage that the ion production time $T_p$ increases by about a factor of hundred. Thus, ion clearing by mean cross-field drift velocities (as in Tables 11-13) with clearing electrodes at the entrance and exit of the dipole magnets yields a sufficiently low neutralization. This is even true for $1.0 \cdot 10^{10}$ antiprotons yielding a factor of four lower cross-field drift velocities and a factor of four higher neutralization. In Tables 17-19 we list the resulting neutralizations for $1.0 \cdot 10^{-11}$ mbar and $1.0 \cdot 10^{11}$ antiprotons.

Table 17: Mean cross-field drift velocity $|\bar{v}_D|$, mean clearing time $T_c$, production time $T_p$ and neutralization $\eta$ for $H_2^+$ ions assuming a partial $H_2$ pressure of $1.0 \cdot 10^{-11}$ mbar ($N_{\bar{p}} = 1.0 \cdot 10^{11}$).

| $p$ GeV/c | $\lvert\bar{v}_D\rvert$ (m/s) | $T_c$ (s) | $T_p$ (s) | $\eta$ |
|---|---|---|---|---|
| 1.5 | 51.3 | 0.0439 | 738 | $5.35 \cdot 10^{-5}$ |
| 3.825 | 32.1 | 0.0701 | 744 | $8.48 \cdot 10^{-5}$ |
| 8.889 | 21.1 | 0.107 | 695 | $1.39 \cdot 10^{-4}$ |
| 15.0 | 16.2 | 0.139 | 638 | $1.96 \cdot 10^{-4}$ |

Table 18: Mean cross-field drift velocity $|\bar{v}_D|$, mean clearing time $T_c$, production time $T_p$ and neutralization $\eta$ for $H_2^+$ ions assuming a partial $H_2$ pressure of $0.8 \cdot 10^{-11}$ mbar ($N_{\bar{p}} = 1.0 \cdot 10^{11}$).

| $p$ GeV/c | $\lvert\bar{v}_D\rvert$ (m/s) | $T_c$ (s) | $T_p$ (s) | $\eta$ |
|---|---|---|---|---|
| 1.5 | 51.3 | 0.0439 | 922 | $4.29 \cdot 10^{-5}$ |
| 3.825 | 32.1 | 0.0701 | 929 | $6.79 \cdot 10^{-5}$ |
| 8.889 | 21.1 | 0.107 | 869 | $1.11 \cdot 10^{-4}$ |
| 15.0 | 16.2 | 0.139 | 798 | $1.57 \cdot 10^{-4}$ |

Table 19: Mean cross-field drift velocity $|\bar{v}_D|$, mean clearing time $T_c$, production time $T_p$ and neutralization $\eta$ for $CO^+$ ions assuming a partial CO pressure of $0.2 \cdot 10^{-11}$ mbar ($N_{\bar{p}} = 1.0 \cdot 10^{11}$).

| $p$ GeV/c | $\lvert\bar{v}_D\rvert$ (m/s) | $T_c$ (s) | $T_p$ (s) | $\eta$ |
|---|---|---|---|---|
| 1.5 | 51.3 | 0.0439 | 850 | $4.64 \cdot 10^{-5}$ |
| 3.825 | 32.1 | 0.0701 | 833 | $7.57 \cdot 10^{-5}$ |
| 8.889 | 21.1 | 0.107 | 745 | $1.29 \cdot 10^{-4}$ |
| 15.0 | 16.2 | 0.139 | 692 | $1.81 \cdot 10^{-4}$ |

## 11. Local Density of Trapped Ions and Secondary Reactions

### 11.1 Transverse distribution of trapped ions

Here, we estimate the local density of trapped ions which is necessary to estimate double ionization processes and other adverse effects like small angle Coulomb scattering and hadronic reactions due to trapped ions. In the longitudinal direction, the local density of trapped ions, $\rho_{ion}(s)$ is proportional to the local neutralization $\eta(s)$. However, the transverse distribution of trapped ions is not simply a replica of the transverse distribution of the beam. This is due to the fact that the ions perform harmonic oscillations in the potential well of the antiproton beam.

If one assumes that the ions are created at rest, i.e. if one neglects the thermal velocity of the molecules, the ions start at the turning point of their harmonic oscillation. During the harmonic oscillation the ions spend most of the time at the turning points. But the time period where the ions move through the beam center is not negligible. This effect yields an enrichment in the beam center and a depletion of the tails. The transverse distribution of ions trapped in a Gaussian beam has been studied by explicitly solving the Liouville equation in a one-dimensional model [27]. The resulting modification of the ion distribution depends on the parameter $\alpha = \sqrt{U/(kT/2)}$, i.e. on the ratio of the potential energy $U$ at the beam edge $(x, y) = (\sigma_x.0)$ or $(x, y) = (0, \sigma_y)$ to the mean thermal energy per degree of freedom, $kT/2$. For the HESR beam the ring-averaged value of $\alpha$ at $T = 3.0$ GeV and $1.0 \cdot 10^{11}$ antiprotons amounts to $\alpha \approx 10$. Thus, the transverse ion distributions are characterized by a narrow central core and tails greatly diluted at the beam edges when comparing with the Gaussian beam distributions. However, this effect is less pronounced if one decreases the number of stored antiprotons by a factor of ten.

### 11.2 Estimate of trapped ion luminosity and secondary reactions

The trapped ions represent an additional target in the antiproton beam. For a rough estimate we neglect the modifications of the trapped ion distributions as discussed in the previous subsection. Thus, we assume that the trapped ion distributions are a replica of the beam distribution. Assuming a bi-Gaussian distribution the total ring-averaged luminosity $L_{ion}$ may be written

$$L_{ion} = N_{\bar{p}} f \oint \frac{1}{4\pi\sigma_x(s)\sigma_y(s)} \frac{\mathrm{d}N_{ion}}{\mathrm{d}s} \mathrm{d}s. \tag{112}$$

In the barrier bucket mode of operation with a bunch length $L_1$, the line density $\mathrm{d}N_{ion}/\mathrm{d}s$ can be expressed by the local neutralization $\eta(s)$,

$$\frac{\mathrm{d}N_{ion}}{\mathrm{d}s} = \frac{N_{\bar{p}}}{L_1}\eta(s). \tag{113}$$

Thus, we get

$$\frac{\mathrm{d}L_{ion}}{\mathrm{d}s} = \frac{N_{\bar{p}}^2 f}{4\pi L_1} \frac{\eta(s)}{\sigma_x(s)\sigma_y(s)} \tag{114}$$

and

$$L_{ion} = \frac{N_{\bar{p}}^2 f}{4\pi L_1} \oint \frac{\eta(s)}{\sigma_x(s)\sigma_y(s)} \mathrm{d}s. \tag{115}$$

A simple estimate of the total ring-averaged luminosity $\bar{L}_{ion}$ can be achieved by inserting ring-averaged values $\bar{\eta}$, $\bar{\sigma}_x$ and $\bar{\sigma}_y$. Using $\bar{\beta}_x = R/Q_x$ and $\bar{\beta}_y = R/Q_y$ where $R$ the effective

radius of the HESR ring, $R = C/(2\pi) = 91.5$ m, yields with $Q_{x,y} \approx 7.6$

$$\bar{\beta}_{x,y} \approx 12.0 \text{ m}. \tag{116}$$

Taking as a characteristic value for the emittance $\epsilon_{x,y} = 0.148$ mm mrad for $1.0 \cdot 10^{11}$ antiprotons yields for a beam momentum of 15 GeV/c

$$\bar{\sigma}_{x,y} = 1.33 \text{ mm}. \tag{117}$$

This yields

$$\bar{L}_{ion} = \bar{\eta} \frac{1.0 \cdot 10^{22}}{4\pi (0.133 \text{ cm})^2} \frac{5.2 \cdot 10^5 \text{ s}^{-1}}{0.9} = \bar{\eta} \cdot 2.6 \cdot 10^{28} \text{ cm}^{-2} \text{ s}^{-1}. \tag{118}$$

For a mean neutralization of $\bar{\eta} = 0.01$ we get $\bar{L}_{ion} \approx 2.6 \cdot 10^{26}$ cm$^{-2}$ s$^{-1}$. The ionization cross section for $H_2$ molecules amounts to $\sigma_{ion} = 2.12 \cdot 10^{-19}$ cm$^2$. Taking the same value for ionization processes on $H_2^+$ ions yields a ring-averaged ionization rate of $\bar{L}_{ion}\sigma_{ion} = 5.5 \cdot 10^7$ s$^{-1}$.

### 11.3 Comparison of primary and secondary reaction rates

It is interesting to compare the primary reaction rates of the antiproton beam due to the interaction with a certain species of residual gas molecules and the secondary reaction rates due to the interaction with the corresponding trapped ions. To this end we compare $\mathrm{d}L_{ion}/\mathrm{d}s$ (see Eq. 114) for a certain species (e.g. $H_2^+$ ions) with the corresponding expression $\mathrm{d}L/\mathrm{d}s$ for the luminosity due to the interaction with the residual gas molecules (local number density $\rho_m(s)$),

$$\frac{\mathrm{d}L}{\mathrm{d}s} = N_{\bar{p}} f \rho_m(s). \tag{119}$$

In the following, we denote the ionization cross section by $\sigma_{ion}$. Taking into account that the neutralization due to a certain molecule species is given by

$$\eta(s) = \frac{L_1}{C} \frac{T_c(s)}{T_p(s)} = \frac{L_1}{C} T_c(s) \sigma_{ion} \rho_m(s) \beta c, \tag{120}$$

the ratio $R = (\mathrm{d}L_{ion}/\mathrm{d}s)/(\mathrm{d}L/\mathrm{d}s)$ of the luminosity due to trapped ions to the luminosity due to residual gas molecules (see Eqs. (114) and (119)) may be written

$$R = N_{\bar{p}} f \frac{T_c(s)}{4\pi \sigma_x(s) \sigma_y(s)} \sigma_{ion}. \tag{121}$$

Inserting typical values for the dominant $H_2$ molecules, $T_c = 0.00281$ s and $\sigma_{ion} = 2.12 \cdot 10^{-23}$ m$^2$ and taking $N_{\bar{p}} = 1.0 \cdot 10^{11}$, $f = 5.2 \cdot 10^5$ Hz and $\sigma_x \sigma_y = (1.33 \cdot 10^{-3})^2$ m$^2$ yields

$$R = 1.39 \cdot 10^{-4}. \tag{122}$$

This example shows that secondary reactions on trapped ions are negligibly small compared to the primary reactions on residual gas molecules. This holds true even if the clearing time $T_c$ rises up to about 1.0 s. In addition we note that the ratio $R$ decreases by a factor of $10^{1/5} = 1.58$ if only $1.0 \cdot 10^{10}$ antiprotons are stored.

## 12. Neutralization in the Arcs

The arcs consist mainly of dipole magnets, see Fig. 1. The space between the dipole magnets is filled with a regular sequence of sextupole magnet, quadrupole magnet, sextupole magnet. The arrangement of magnetic elements is very compact and the drift spaces between the different elements are very short. There are only two longer drift spaces in the arcs which replace the missing dipoles near the entrance and exit of the arcs. Their length amounts to about 4.5 m. There are 22 dipole magnets of 4.2 m length in one arc yielding a total length of about 92.4 m. The total length of one arc amounts to 153.310 m. That means that about 60 % of the total arc length is covered by the dipole magnets and the mean neutralization of the arc depends very much on the mean neutralization in the dipole magnets.

We first assume that clearing electrodes near the entrance and exit of the dipole magnets are used in order to extract the ions coming from the inside of the dipole magnets. The mean cross-field drift velocities $\bar{v}_D$ and the resulting clearing rates $1/T_c$ are rather low and the neutralizations $\eta$ are rather high in the region of the dipole magnets, see estimates in Tables 11-13 in Subsection 10.4 for $1.0 \cdot 10^{11}$ antiprotons. We assume an UHV pressure of $1.0 \cdot 10^{-9}$ mbar with 80 % $H_2$ and 20 % CO molecule content. The assumption of 20 % CO molecules takes approximately the contribution of CO and other heavier molecules like $CH_4$, $H_2O$, $N_2$ etc. into account. Taking the mean neutralization values for $H_2^+$ and $CO^+$ from Tables 12 and 13 yields for $1.0 \cdot 10^{11}$ antiprotons a mean neutralization $\bar{\eta}$ between 0.9 % at 1.5 GeV/c and 3.4 % at 15 GeV/c. For $1.0 \cdot 10^{10}$ antiprotons the mean neutralization would be even about a factor of four larger, i.e. about 3.6 % at 1.5 GeV/c and 13.5 % at 15 GeV/c.

Such neutralizations in the dipole magnets are dangerous in view of possible coherent instabilities. Therefore, we suggest to use continuous vertical clearing electrodes in the dipole magnets, see Sect. 10.5. Assuming vertical electric fields $E_y$ of about 2250 V/m yields accelerations $a_y$ of about $1.08 \cdot 10^{11}$ m/s$^2$ for $H_2^+$ and $7.70 \cdot 10^9$ m/s$^2$ for $CO^+$. Assuming $T_c \approx \sqrt{6\sigma_y/a_y}$ the resulting clearing times $T_c(s)$ are below $1.0 \cdot 10^{-6}$ s and the neutralization $\eta$ below $1.0 \cdot 10^{-7}$.

Another possibility to reduce the neutralization is clearing with horizontal electric fields, see Subsect. 10.6. Assuming horizontal electric fields $E_x$ of about 3400 V/m yields rather high cross-field drift velocities $E_x/B_y$ and neutralizations $\eta$ of order of magnitude $10^{-4}$ and below, see Tables 14-16.

A third possibility to reduce the neutralization is a substantial improvement of the UHV vacuum by a factor of about hundred, see Subsect. 10.7. This yields immediately a reduction of the neutralization $\eta$ by a factor of hundred, see Tables 17-19 in Subsect. 10.7.

The clearing electrodes near the entrance and exit of the dipole magnets are also used in order to extract the ions coming from the straight sections between the dipole magnets which consist of a regular sequence of sextupole, quadrupole and sextupole. The distance between the clearing electrodes amounts to about 2.0 m. We assume that the ion drift velocities in the straight sections between the dipole magnets are dominated by the mean thermal drift velocity in one direction, $\bar{v}_{\parallel}$. (We mention that the rather high $\vec{E} \times \vec{B}$ cross-field drift velocities in quadrupole and sextupole magnets estimated in subsections 8.5 and 8.6 can never be reached by transverse acceleration in the rather weak electric field $E_x$ of the antiproton beam). The resulting mean neutralization $\bar{\eta}$ due to $H_2^+$ and $CO^+$ varies between $5.6 \cdot 10^{-4}$ at 1.5 GeV/c and $4.5 \cdot 10^{-4}$ at 15 GeV/c.

The neutralization $\eta(s)$ at 15 GeV/c is shown in Fig. 14 in the top panel for clearing by mean cross-field drift velocities with clearing electrodes at the entrance and exit of dipole

magnets and in the bottom panel for adding continuous vertical clearing electrodes inside dipole magnets. Using only clearing by mean cross-field drift velocities with clearing electrodes at the entrance and exit of dipole magnets yields an average neutralization $\bar{\eta}$ of the arcs of 2.1 % at 15 GeV/c. Adding continuous vertical clearing electrodes inside dipole magnets yields $\bar{\eta} = 1.8 \cdot 10^{-4}$.

In Sect. 13. we show also results assuming an UHV pressure of $1.0 \cdot 10^{-9}$ mbar with 100 % $H_2$ and 0 % CO molecule content. In addition, we show results assuming that the clearing in the straight sections is mainly due to the longitudinal acceleration by the electric fields $E_s$.

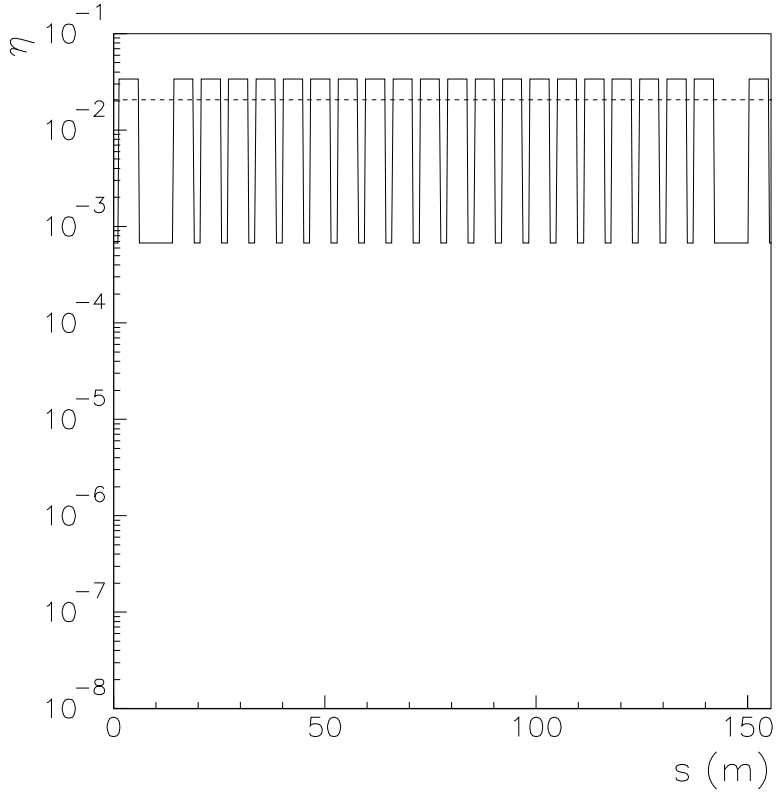


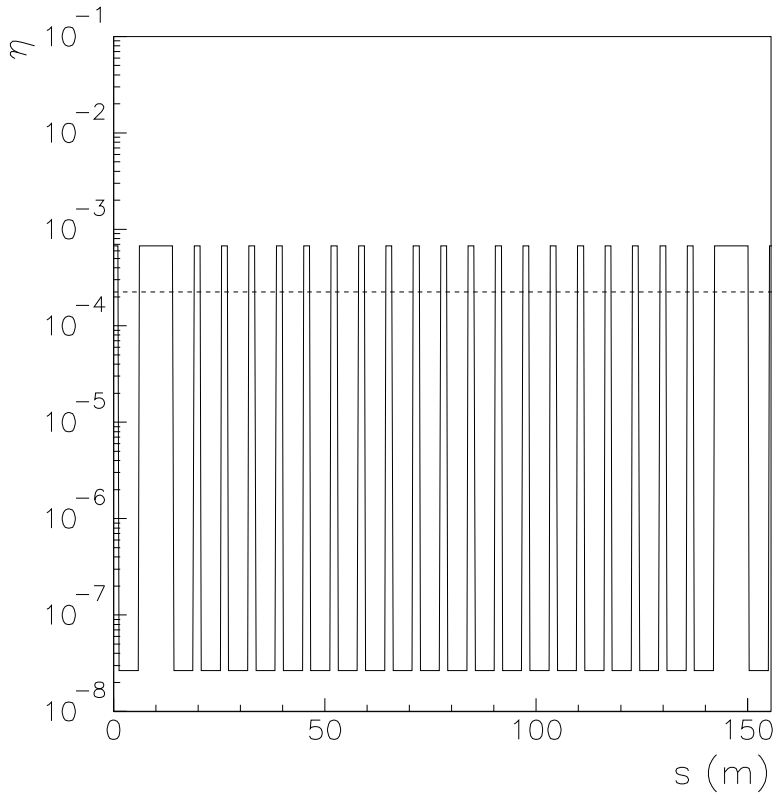


Fig. 14: Neutralization $\eta$ in the arcs at 15 GeV/c assuming $1.0 \cdot 10^{11}$ antiprotons, $0.8 \cdot 10^{-9}$ mbar for $H_2$ and $0.2 \cdot 10^{-9}$ mbar for CO. Clearing in the straight sections by mean thermal drift velocities $\bar{v}_{\parallel}$. **Top**: Clearing electrodes at the entrance and exit of dipoles magnets. **Bottom**: Continuous clearing electrodes inside dipole magnets and clearing electrodes at the entrance and exit of dipoles magnets. Dashed lines: Average neutralization of the arcs.

## 13. Neutralization in the Full HESR Ring

### 13.1 Estimates with different assumptions

Here, we show the neutralization of the full HESR ring assuming different scenarios. The HESR storage ring has a racetrack shape with two long straight sections, see Fig. 1. The long straight sections are located between $s_1 = 154.75$ m and $s_2 = 289.03$ m and between $s_3 = 442.34$ m and $s_4 = (575.18 + 1.44)$ m. The total length of one long straight section amounts to 134.282 m. We differentiate between the cooler straight section and the target straight section. The 24 m long electron cooler will be installed in the cooler straight section. The PANDA target together with the spectrometer solenoid and a dipole chicane will be installed in the target straight section. The problem of trapped ions in the electron cooler is discussed in Sect. 14.. The problem of trapped ions in the PANDA target region is discussed in Sect. 15.. We present eight scenarios with different assumptions:

(i) The HESR ring is assembled without electron cooler, see Figs 15 - 18. In the long straight sections the mean distance between the clearing electrodes amounts to about 5 m. This distance corresponds to the magnetic length of the compensation solenoids. In the arcs, the clearing electrodes are located near the entrance and exit of the dipole magnets. We assume that the clearing is either due to the mean thermal drift velocity[5] $\bar{v}_{\|}$ or due to the longitudinal acceleration by the electric field $E_s$ of the antiproton beam. The pressure outside of the PANDA target region amounts to about $1.0 \cdot 10^{-9}$ mbar and the residual gas consists either of $H_2^+$ molecules (100 %) or $H_2^+$ molecules (80 %) and CO molecules (20 %). The neutralization in the PANDA target region is estimated assuming that the residual gas consists mainly of $H_2$ molecules and assuming clearing by the mean thermal velocity of $H_2$ molecules with $L = 5$ m. Overneutralization is not possible. Therefore we set $\eta = 1$ in regions where $0.9\,T_c/T_p > 1$. The special problems of the PANDA target region are discussed in Sect. 15.. The resulting mean neutralization $\bar{\eta}$ is indicated in the Figure captions.

(ii) The HESR ring is assembled with an electron cooler (EC), see Figs. 19 - 22. In the region of the electron cooler, i.e. between $s_1 = 209.890$ m and $s_2 = 233.890$ m, the mean neutralization amounts to about 0.012, see the final HESR electron cooler design study [34] and Sect. 14.. It refers to the sum of the electron and antiproton beam current, i.e. to 1.00833 A. The corresponding linear charge density amounts to $\lambda(e + \bar{p}) = -3.36 \cdot 10^{-9}$ C/m. Thus we get a linear charge density of trapped ions of $\lambda(ion) = +4.04 \cdot 10^{-11}$ C/m. The linear charge density of the antiproton beam alone (0.00833 A for $1.0 \cdot 10^{11}$ antiprotons and 15 GeV/c) amounts to $\lambda(\bar{p}) = -2.78 \cdot 10^{-11}$ C/m. Referring the linear charge density of trapped ions in the EC only to the linear charge density of the antiproton beam yields $\lambda(ion)/\lambda(\bar{p}) = 1.45$, i.e. more than 100 %!

### 13.2 Discussion

The drift of ions in the straight sections depends on the mean thermal velocity in one direction $\bar{v}_{\|}$ (see Table 3) as well as on the longitudinal acceleration $a_s = q\,E_s/m$ by the longitudinal electric field $E_s$ of the antiproton beam (see Fig. 8). The longitudinal electric field $E_s$ and therewith the longitudinal acceleration $a_s$ depends on the number of stored antiprotons. For $1.0 \cdot 10^{10}$ antiprotons the longitudinal accelerations are by a factor of about eight lesser than for $1.0 \cdot 10^{11}$ antiprotons (see discussion at the end of Subsects. 3.1 and 3.3). For $1.0 \cdot 10^{11}$ antiprotons, the typical longitudinal accelerations of $H_2^+$ and $CO^+$ ions amount to about $1.0 \cdot 10^6$ m/s$^2$ and

[5] The resulting clearing times $T_c$, production times $T_p$ and neutralizations $\eta$ are listed in the Tables 8 - 10.

$7.1 \cdot 10^4$ m/s$^2$, respectively.

The ion clearing in straight sections is dominated by the mean thermal velocity $\bar{v}_\parallel$ if the longitudinal acceleration $a_s$ is relatively small, i.e. if $|a_s| < \bar{v}_\parallel^2/L$ ($L$ is the distance between two clearing electrodes in a straight section). That means for $L = 5$ m $|a_s| < 1.58 \cdot 10^5$ m/s$^2$ for $H_2^+$ and $|a_s| < 4.22 \cdot 10^4$ m/s$^2$ for $CO^+$. Then, we can estimate the mean clearing time $T_c$ using

$$T_c \approx \frac{L}{2\,\bar{v}_\parallel}. \tag{123}$$

The condition $a_s < \bar{v}_\parallel^2/L$ occurs for $1.0 \cdot 10^{11}$ antiprotons at a few positions in the ring. It is generally fulfilled for $1.0 \cdot 10^{10}$ antiprotons.

The ion clearing in straight sections is dominated by the longitudinal acceleration $a_s$ if $|a_s| > \bar{v}_\parallel^2/L$. That means for $L = 5$ m $|a_s| > 1.58 \cdot 10^5$ m/s$^2$ for $H_2^+$ and $|a_s| > 4.22 \cdot 10^4$ m/s$^2$ for $CO^+$. Then, we can estimate the mean clearing time $T_c$ using

$$T_c \approx \sqrt{\frac{8}{9}\frac{L}{|a_s|}} \approx \sqrt{\frac{L}{|a_s|}}. \tag{124}$$

For $1.0 \cdot 10^{11}$ antiprotons, the ion clearing in straight sections is mainly due to the longitudinal acceleration $a_s$, see Figs. 17, 18, 21 and 22.

Comparing Figs. 15, 16, 19 and 20 with Figs. 17, 18, 21 and 22 one sees that clearing by mean thermal velocities $\bar{v}_\parallel$ yields similar results as clearing by the longitudinal acceleration $a_s$.

Comparing the contributions of $H_2$ and CO molecules one sees that the neutralization outside of the PANDA target is about a factor of four larger if the contribution of 20 % CO molecules is taken into account. This is due to the larger ionization cross sections of CO molecules.

The ring-averaged neutralization $\bar{\eta}$ is dominated by the pressure bump near the PANDA target. A substantial contribution is due to the dipole magnets if the vacuum pressure amounts to about $1.0 \cdot 10^{-9}$ mbar and the ions are cleared by mean cross-field drift velocities with clearing electrodes at the entrance and exit of the dipole magnets, see top panels of Figs. 15 - 22. The situation would be even worse for $1.0 \cdot 10^{10}$ antiprotons since the cross-field drift velocities would be a factor of about four lower and the neutralization in the dipole magnets a factor of about four higher. The contribution due to the dipole magnets is negligibly small for ion clearing by vertical or horizontal electric fields, see Subsects. 10.5 and 10.6. The same holds true if the residual gas pressure is reduced from $1.0 \cdot 10^{-9}$ mbar to $1.0 \cdot 10^{-11}$ mbar, see Subsect. 10.7.

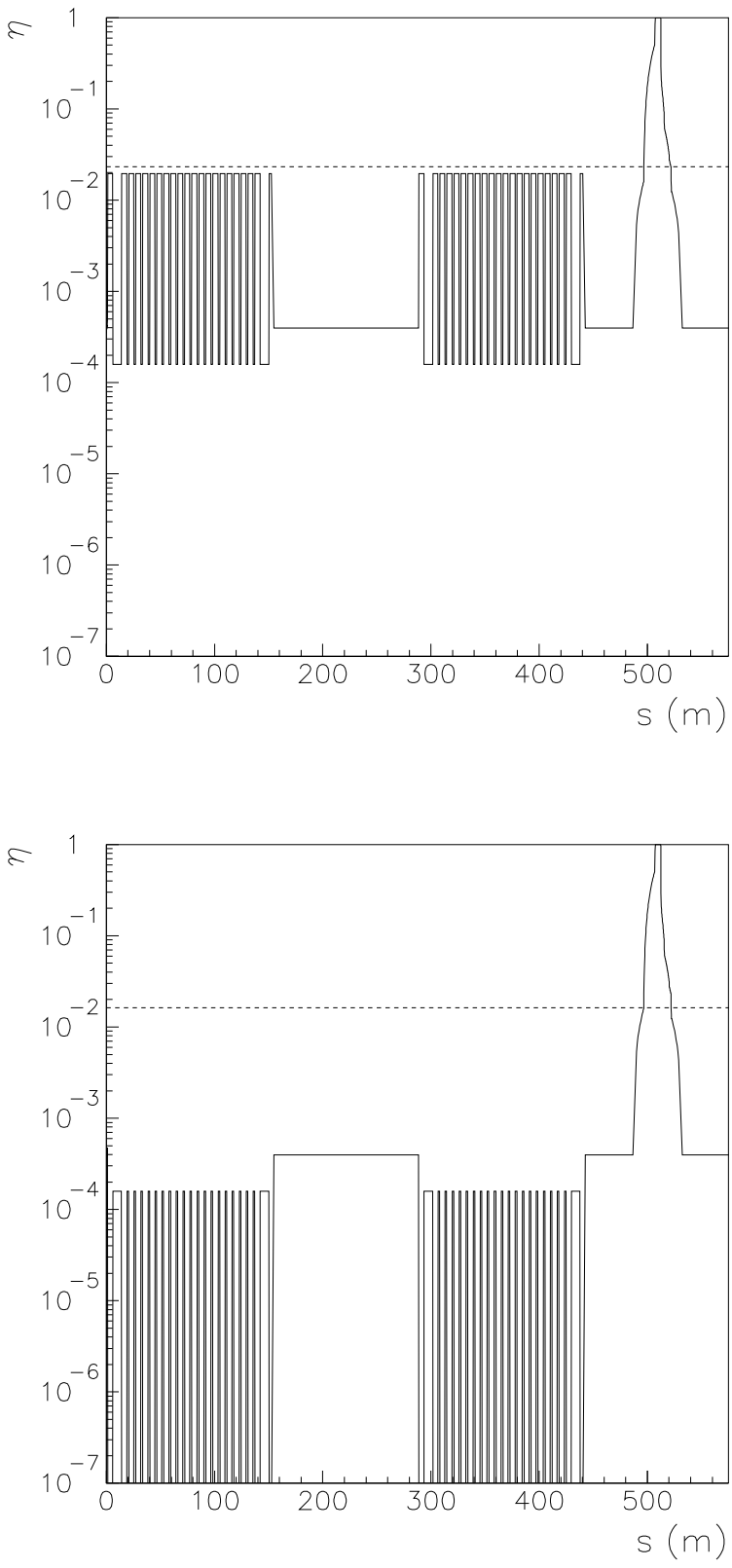


Fig. 15: Neutralization $\eta$ in the HESR ring ($1.0 \cdot 10^{11}$ antiprotons, 15 GeV/c) **without EC** assuming outside of the PANDA target region partial pressures of $1.0 \cdot 10^{-9}$ mbar for $H_2$ and $0.0 \cdot 10^{-9}$ mbar for CO. **Clearing in the straight sections by mean thermal drift velocities** $\bar{v}_{\parallel}$. Distance between clearing electrodes in the long straight sections: 5 m. Distance between clearing electrodes in the straight sections of the arcs: 2 m. **Top**: Clearing electrodes only at the entrance and exit of dipole magnets, $\bar{\eta} = 0.0232$. **Bottom**: Clearing electrodes at the entrance and exit of dipole magnets and continuous clearing electrodes inside dipole magnets, $\bar{\eta} = 0.0162$. Dashed line: Mean neutralization $\bar{\eta}$.

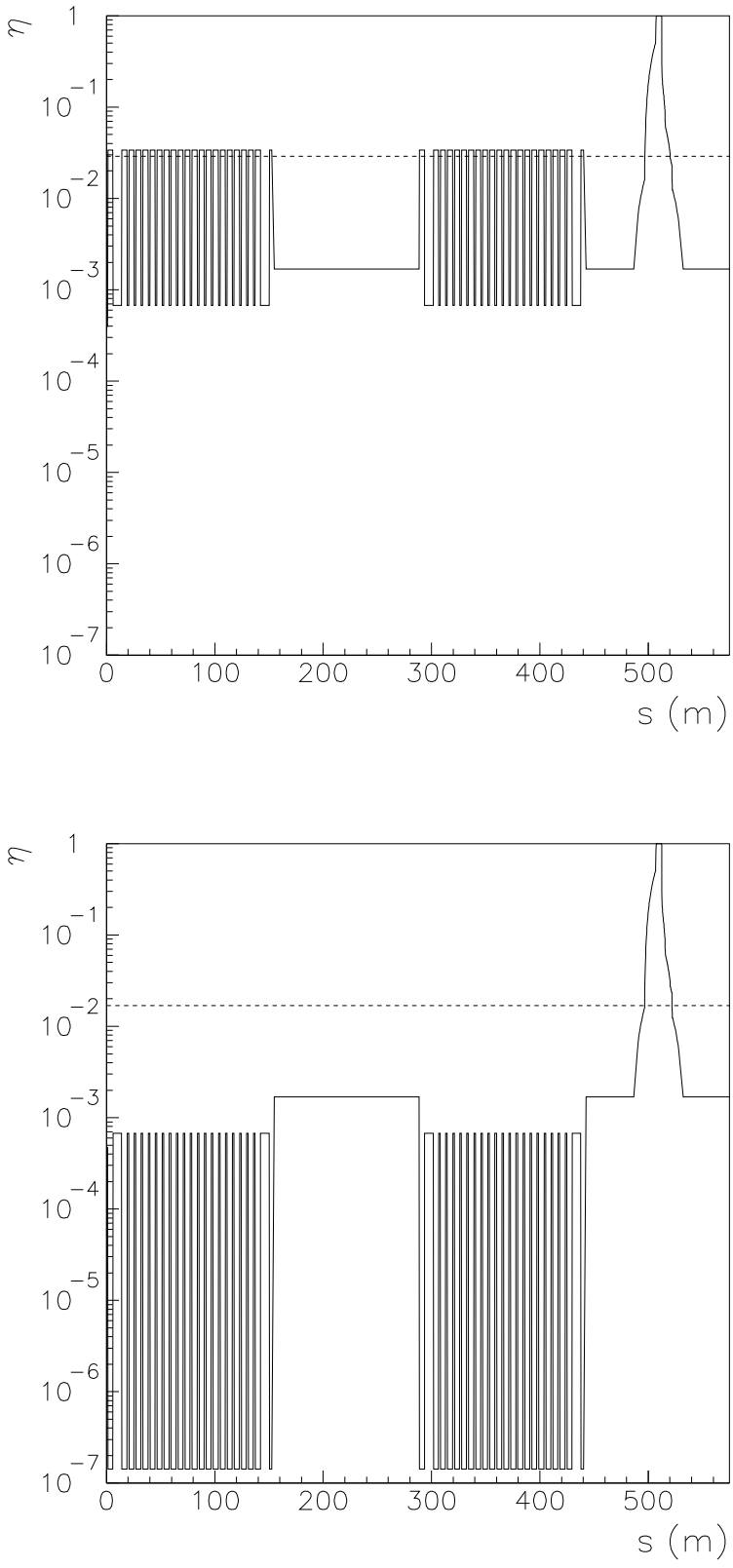


Fig. 16: Neutralization $\eta$ in the HESR ring ($1.0 \cdot 10^{11}$ antiprotons, 15 GeV/c) **without EC** assuming outside of the PANDA target region partial pressures of $0.8 \cdot 10^{-9}$ mbar for $H_2$ and $0.2 \cdot 10^{-9}$ mbar for CO. **Clearing in the straight sections by mean thermal drift velocities** $\bar{v}_{\parallel}$. Distance between clearing electrodes in the long straight sections: 5 m. Distance between clearing electrodes in the straight sections of the arcs: 2 m. **Top**: Clearing electrodes only at the entrance and exit of dipole magnets, $\bar{\eta} = 0.0289$. **Bottom**: Clearing electrodes at the entrance and exit of dipole magnets and continuous clearing electrodes inside dipole magnets, $\bar{\eta} = 0.0168$. Dashed line: Mean neutralization $\bar{\eta}$.

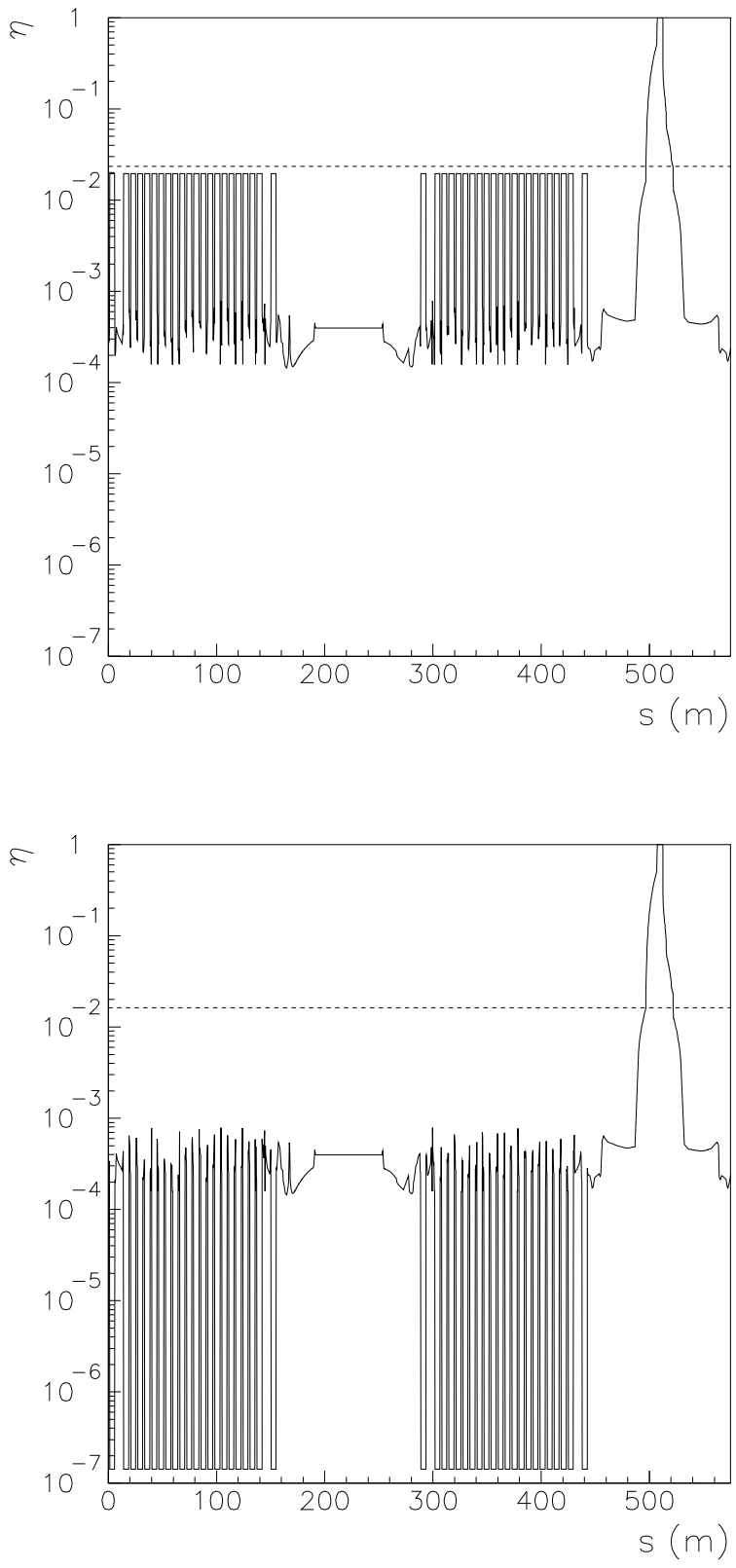


Fig. 17: Neutralization $\eta$ in the HESR ring ($1.0 \cdot 10^{11}$ antiprotons, 15 GeV/c) **without EC** assuming outside of the PANDA target region partial pressures of $1.0 \cdot 10^{-9}$ mbar for $H_2$ and $0.0 \cdot 10^{-9}$ mbar for CO. **Clearing in the straight sections dominated by longitudinal acceleration** $a_s = qE_s/m$. Distance between clearing electrodes in the long straight sections: 5 m. Distance between clearing electrodes in the straight sections of the arcs: 2 m. **Top**: Clearing electrodes only at the entrance and exit of dipole magnets, $\bar{\eta} = 0.0234$. **Bottom**: Clearing electrodes at the entrance and exit of dipole magnets and continuous clearing electrodes inside dipole magnets, $\bar{\eta} = 0.0162$. Dashed line: Mean neutralization $\bar{\eta}$.

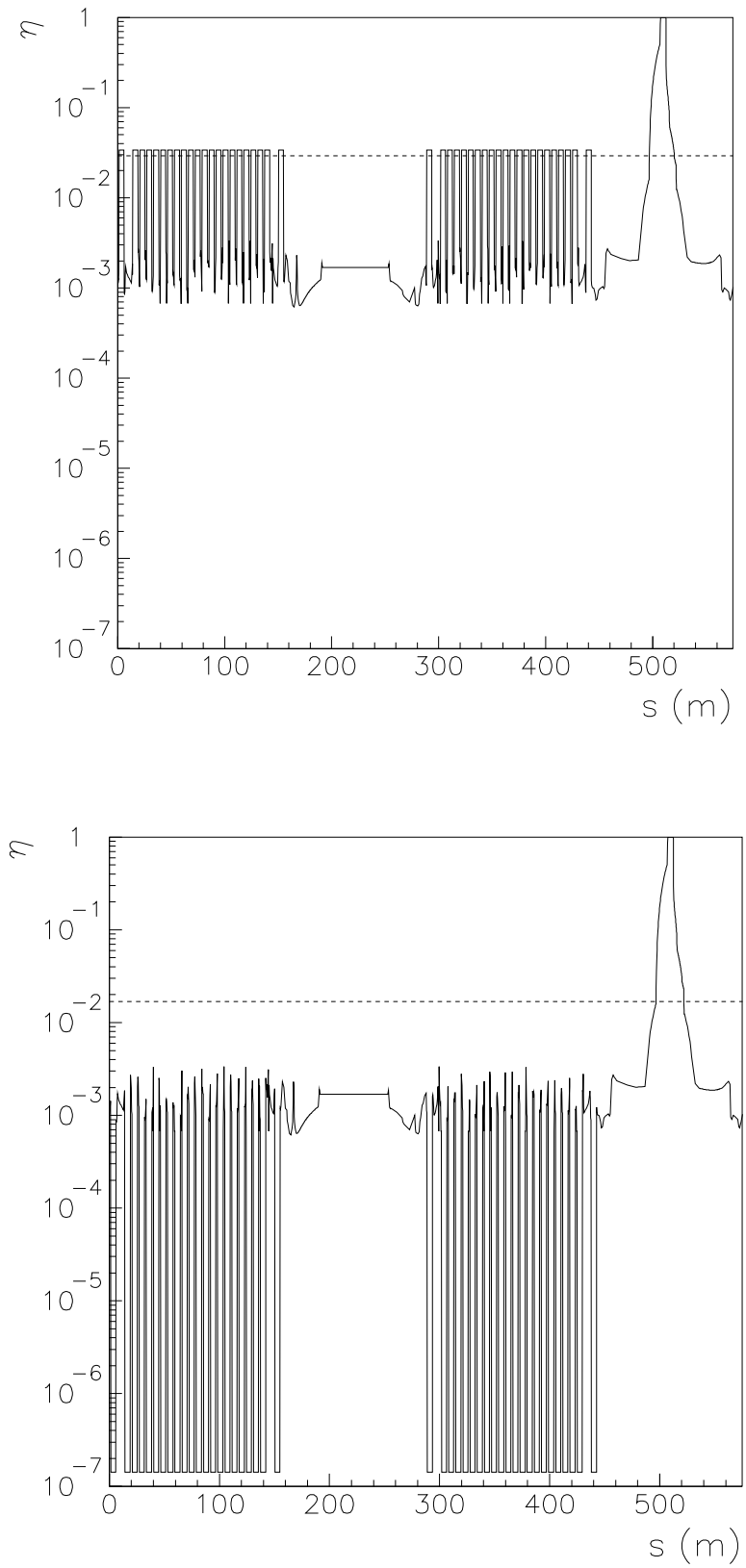


Fig. 18: Neutralization $\eta$ in the HESR ring ($1.0 \cdot 10^{11}$ antiprotons, 15 GeV/c) **without EC** assuming outside of the PANDA target region partial pressures of $0.8 \cdot 10^{-9}$ mbar for $H_2$ and $0.2 \cdot 10^{-9}$ mbar for CO. **Clearing in the straight sections dominated by longitudinal acceleration** $a_s = qE_s/m$**.** Distance between clearing electrodes in the long straight sections: 5 m. Distance between clearing electrodes in the straight sections of the arcs: 2 m. **Top**: Clearing electrodes only at the entrance and exit of dipole magnets, $\bar{\eta} = 0.0293$. **Bottom**: Clearing electrodes at the entrance and exit of dipole magnets and continuous clearing electrodes inside dipole magnets, $\bar{\eta} = 0.0168$. Dashed line: Mean neutralization $\bar{\eta}$.

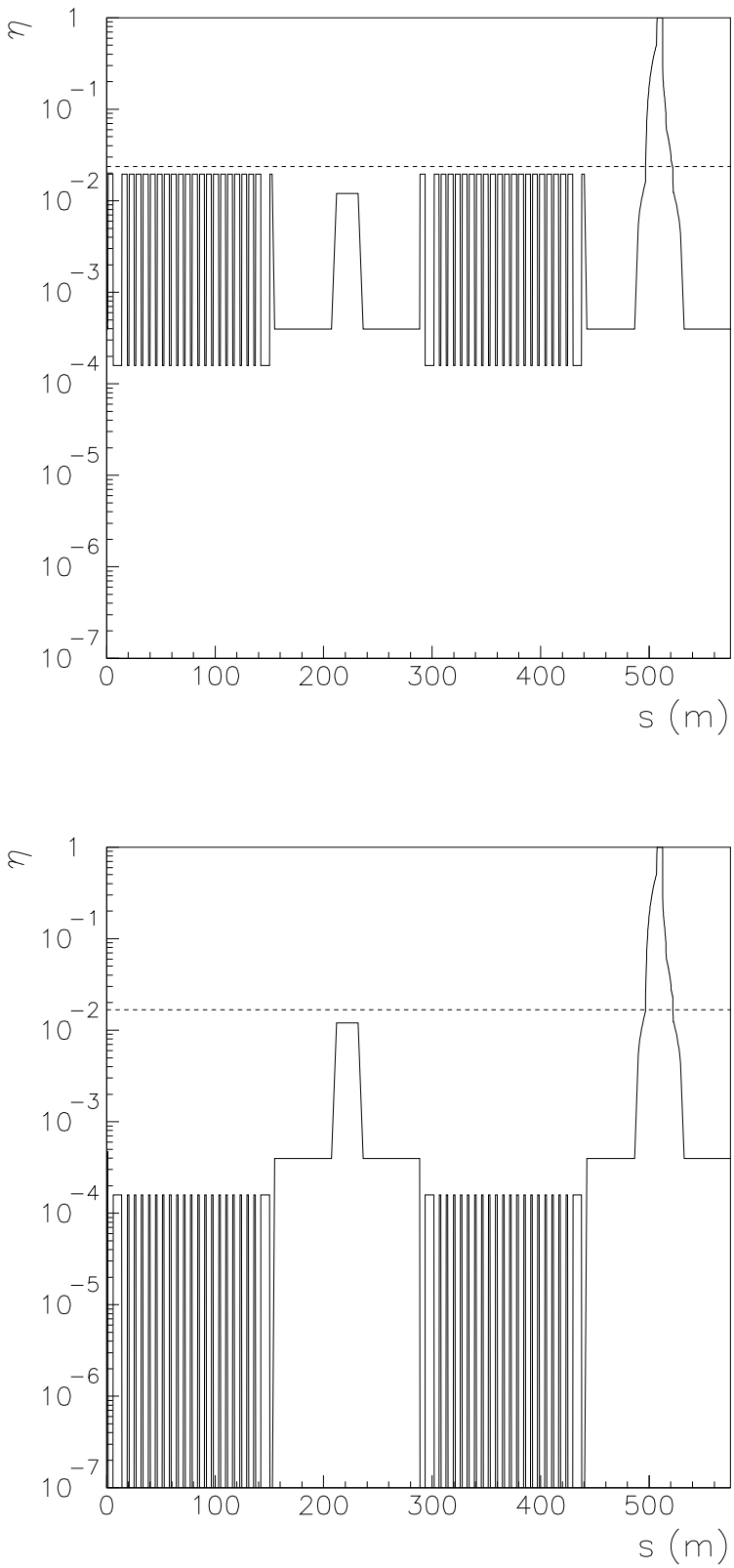


Fig. 19: Neutralization $\eta$ in the HESR ring ($1.0 \cdot 10^{11}$ antiprotons, 15 GeV/c) **with EC** assuming outside of the PANDA target region partial pressures of $1.0 \cdot 10^{-9}$ mbar for $H_2$ and $0.0 \cdot 10^{-9}$ mbar for CO. **Clearing in the straight sections by mean thermal drift velocities** $\bar{v}_{\parallel}$. Distance between clearing electrodes in the long straight sections: 5 m. Distance between clearing electrodes in the straight sections of the arcs: 2 m. **Top**: Clearing electrodes only at the entrance and exit of dipole magnets, $\bar{\eta} = 0.0237$. **Bottom**: Clearing electrodes at the entrance and exit of dipole magnets and continuous clearing electrodes inside dipole magnets, $\bar{\eta} = 0.0167$. Dashed line: Mean neutralization $\bar{\eta}$.

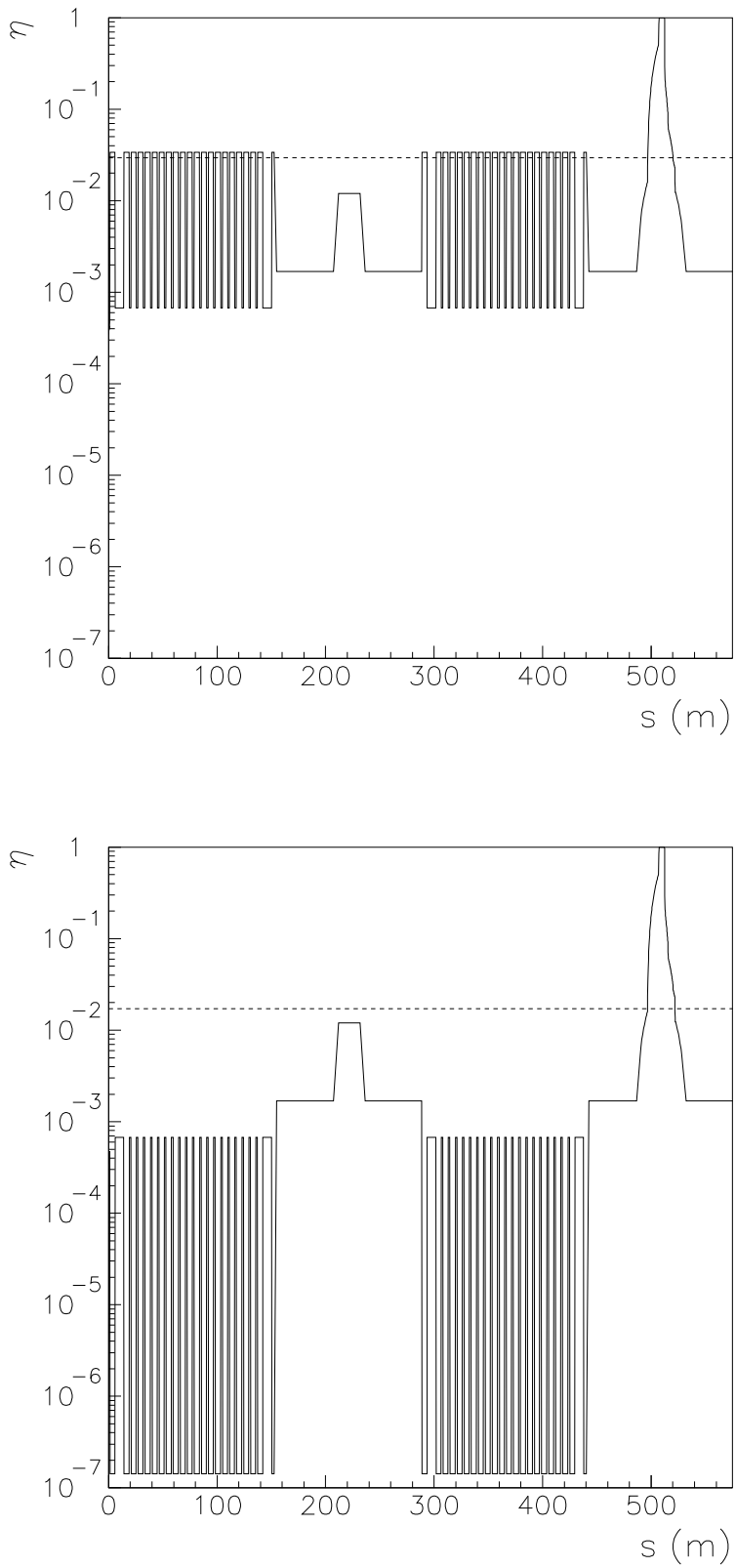


Fig. 20: Neutralization $\eta$ in the HESR ring ($1.0 \cdot 10^{11}$ antiprotons, 15 GeV/c) **with EC** assuming outside of the PANDA target region partial pressures of $0.8 \cdot 10^{-9}$ mbar for $H_2$ and $0.2 \cdot 10^{-9}$ mbar for CO. **Clearing in the straight sections by mean thermal drift velocities** $\bar{v}_{\parallel}$. Distance between clearing electrodes in the long straight sections: 5 m. Distance between clearing electrodes in the straight sections of the arcs: 2 m. **Top**: Clearing electrodes only at the entrance and exit of dipole magnets, $\bar{\eta} = 0.0294$. **Bottom**: Clearing electrodes at the entrance and exit of dipole magnets and continuous clearing electrodes inside dipole magnets, $\bar{\eta} = 0.0172$. Dashed line: Mean neutralization $\bar{\eta}$.

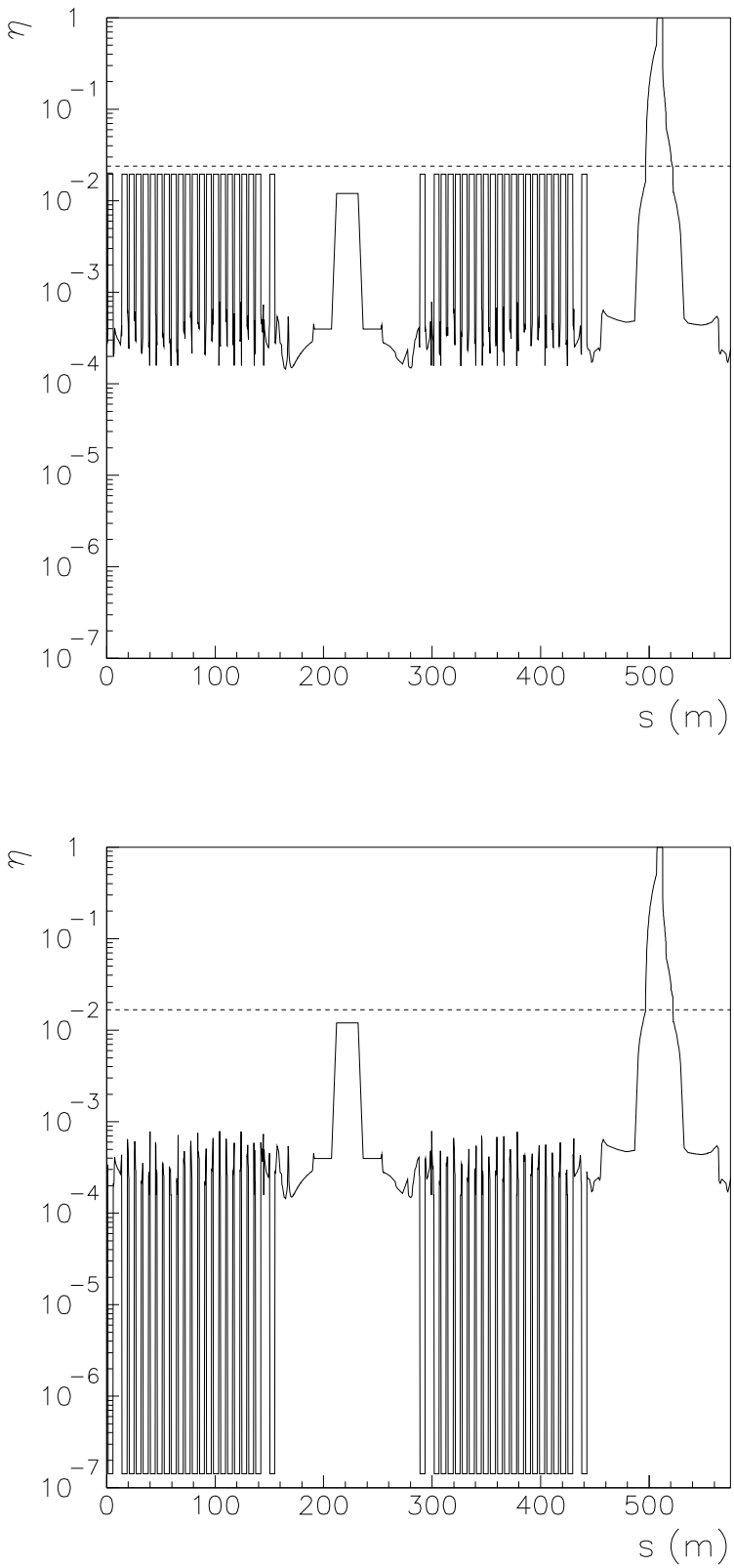


Fig. 21: Neutralization $\eta$ in the HESR ring ($1.0 \cdot 10^{11}$ antiprotons, 15 GeV/c) **with EC** assuming outside of the PANDA target region partial pressures of $1.0 \cdot 10^{-9}$ mbar for $H_2$ and $0.0 \cdot 10^{-9}$ mbar for CO. **Clearing in the straight sections dominated by longitudinal acceleration** $a_s = qE_s/m$. Distance between clearing electrodes in the long straight sections: 5 m. Distance between clearing electrodes in the straight sections of the arcs: 2 m. **Top**: Clearing electrodes only at the entrance and exit of dipole magnets, $\bar{\eta} = 0.0239$. **Bottom**: Clearing electrodes at the entrance and exit of dipole magnets and continuous clearing electrodes inside dipole magnets, $\bar{\eta} = 0.0167$. Dashed line: Mean neutralization $\bar{\eta}$.

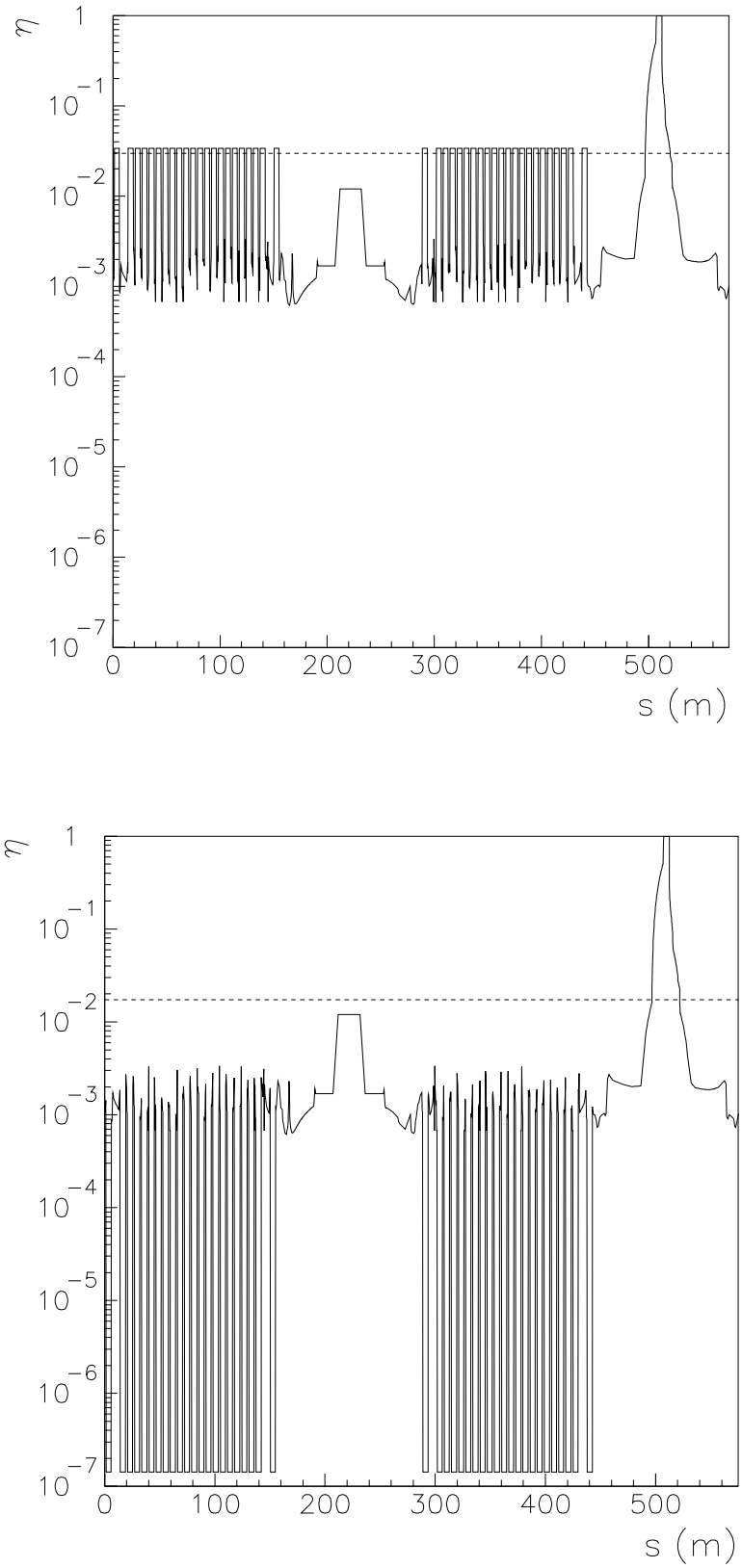


Fig. 22: Neutralization $\eta$ in the HESR ring ($1.0 \cdot 10^{11}$ antiprotons, 15 GeV/c) **with EC** assuming outside of the PANDA target region partial pressures of $0.8 \cdot 10^{-9}$ mbar for $H_2$ and $0.2 \cdot 10^{-9}$ mbar for CO. **Clearing in the straight sections dominated by longitudinal acceleration** $a_s = qE_s/m$. Distance between clearing electrodes in the long straight sections: 5 m. Distance between clearing electrodes in the straight sections of the arcs: 2 m. **Top**: Clearing electrodes only at the entrance and exit of dipole magnets, $\bar{\eta} = 0.0297$. **Bottom**: Clearing electrodes at the entrance and exit of dipole magnets and continuous clearing electrodes inside dipole magnets, $\bar{\eta} = 0.0173$. Dashed line: Mean neutralization $\bar{\eta}$.

## 14. Electron Cooler

Here, we discuss the special problems due to the electron beam if the electron cooler (EC) is installed. We refer to the final HESR electron cooler design study [34]. The electron beam current $I$ amounts to 1.0 A. It is guided by the EC solenoid with a constant beam radius $a = 5$ mm. The inner diameter of the EC vacuum chamber amounts to 200 mm. The resulting radius profile $r_c(s)$ is shown in Fig. 23. The total length of the EC solenoid is $L_{EC} = 24.0$ m. In addition, nine beam position monitors are foreseen. The beam position monitors consist of four electrodes that together form a cylinder with an inner diameter of 200 mm and a length of 200 mm.

### 14.1 Negative potential well of the electron beam

We first estimate the negative potential well due to the strong electron beam. The linear charge density $\lambda$ is given by

$$\lambda = \frac{\mathrm{d}Q}{\mathrm{d}s} = \frac{I}{v}. \tag{125}$$

Here, $I$ is the current and $v = \beta c \approx c$ the longitudinal velocity of the electrons. The resulting potential well and the electric field can be calculated using Eqs. (4)-(6). A round electron beam of 1.0 A with a constant density within a radius $a = 5$ mm yields the following values:

$$\frac{\lambda}{2\pi\epsilon_0} = -59.9 \text{ V}, \tag{126}$$

$$U(0) = -195 \text{ V}, \tag{127}$$

$$E_r(a) = -12 \text{ kV/m}. \tag{128}$$

The absolute value of the electric field component in radial direction, $|E_r|$, is maximum at the edge of the electron beam, i.e. at $r = a$. For comparison we calculate the corresponding potential well parameters of the antiproton beam at 8.889 GeV/c using Eqs. (8)and (9). Inside the EC the rms widths of the bi-Gaussian beam distribution are $\sigma_x \approx 6.5$ mm and $\sigma_y \approx 6.5$ mm, the inner radius of the beam pipe amounts to 100 mm. These parameters yield for $1.0 \cdot 10^{11}$ antiprotons at 8.889 GeV/c

$$\frac{\lambda}{2\pi\epsilon_0} = -0.556 \text{ V}, \tag{129}$$

$$U(0) = -1.63 \text{ V}, \tag{130}$$

$$E_r(a) = -42.8 \text{ V/m}. \tag{131}$$

Here, the absolute value of $E_r(a)$ represents the value of the electric field at the 1-sigma edge $r = a = \sigma_x = \sigma_y$ of the antiproton beam. The depth of the electron potential well is a factor of 120 larger than the depth of the antiproton potential well and the strength of the electric field near the edge is a factor of 280 larger.

Summarizing, the negative potential well of the electron beam acts as a very deep pocket for trapped ions (see Fig. 24). The positive ions perform modified cyclotron motions around the magnetic field lines of the solenoid and magnetron motions around the central axis of the electron beam, see Subsections 9.3.

It is interesting to note that the transverse electric field of the electron beam (about 12 kV/m at beam edge) is so strong that $\omega_b = 1.07 \cdot 10^7$ s$^{-1}$ for $H_2^+$ ions. The magnetic field of

the EC solenoid is rather low (0.2 T) yielding $\omega_c = 9.58 \cdot 10^6$ s$^{-1}$ for $H_2^+$ ions. Using Eqs. (98) and (99), we get $f_+ = 2.63 \cdot 10^6$ Hz for the frequency of the modified cyclotron motion and $f_- = 1.11 \cdot 10^6$ Hz for the frequency of the magnetron motion of $H_2^+$ ions. The high value of $f_-$ is a consequence of the high transverse electric field. In the PANDA target solenoid and the compensation solenoids the frequency $f_-$ is rather low.

### 14.2 Ionization rate and neutralization due to the electron beam

The number of antiprotons per second amounts to about $\dot{N}_{\bar{p}} = 5.0 \cdot 10^{16}$ s$^{-1}$ if $1.0 \cdot 10^{11}$ antiprotons are stored in the HESR ring. This corresponds to a $\bar{p}$ current of about 8 mA. The current of the electron beam amounts to 1.0 A. This corresponds to a number of electrons per second of $\dot{N}_e = 6.24 \cdot 10^{18}$ s$^{-1}$ which is a factor of 125 larger. Therefore, the ionization rate due to the electron beam is also a factor of 125 larger. In the following estimates of ionization and neutralization we neglect the very small contribution of the antiproton beam in the region of the electron cooler.

We recall that the ionization cross section depends on the molecules in the residual gas and the velocity $\beta = v/c$ of the beam particles. It does not depend on the charge and the mass of the beam particles. Now, the velocity of the electron beam is exactly equal to the velocity of the antiproton beam. Therefore, applying Bethe's formula (17) yields identical ionization cross sections $\sigma$ for electrons and antiprotons and we can use the values listed in Table 2. The corresponding production rate $R_p$ for a certain ion species is given by

$$R_p = \sigma \rho_m \beta c. \tag{132}$$

Here, $\sigma$ is the ionization cross section, $\rho_m$ the number density of the residual molecules and $\beta c$ the velocity of the beam particles. The production time $T_p$ is the inverse of the production rate, $T_p = 1/R_p$. It is simply the time which a single antiproton and/or electron needs in order to produce one singly charged ion. We note that the production rate $R_p$ and the production time $T_p$ are also identical for electrons and antiprotons.

The following estimates are taken from the final electron cooler design study [34]. In the region of the electron cooler big pumps on both sides of the straight cooling section and the return straight section are installed. The distance between the pumps is 30 m. The outgassing rate is assumed to be $q = 1.0 \cdot 10^{-12}$ mbar·liter/cm$^2$/s after bake-out to 150°C. The residual gas is assumed to consist of $H_2$ (75 %), $CH_4$ (14 %) and CO (11 %). The average pressure for each gas is calculated taking the specific molecular conductance $w = 305\, r^3 \sqrt{T/M}$ into account. The calculated average partial pressures become

1. $5.5 \cdot 10^{-10}$ mbar for $H_2$ ($\rho_m = 1.5 \cdot 10^{13}$ m$^{-3}$),
2. $1.3 \cdot 10^{-10}$ mbar for CO ($\rho_m = 3.5 \cdot 10^{12}$ m$^{-3}$),
3. $2.0 \cdot 10^{-10}$ mbar for $CH_4$ ($\rho_m = 5.3 \cdot 10^{12}$ m$^{-3}$).

The ionization cross sections $\sigma$ and the resulting production times $T_p$ are

1. $\sigma = 2 \cdot 10^{-23}$ m$^2$, $T_p = 11$ s for $H_2$,
2. $\sigma = 9 \cdot 10^{-23}$ m$^2$, $T_p = 11$ s for CO,
3. $\sigma = 11 \cdot 10^{-23}$ m$^2$ $T_p = 6$ s for $CH_4$.

It is planned to remove the trapped ions with clearing electrodes near the entrance and exit of the straight cooling section [34]. The clearing electrodes are installed in the merging modules. The resulting clearing times due to the mean thermal velocity in one direction are estimated as [34]

1. $T_c = 13$ ms for $H_2$,
2. $T_c = 50$ ms for CO,
3. $T_c = 38$ ms for $CH_4$.

The resulting mean neutralization $\eta$ from $H_2$, CO and $CH_4$ amounts to

$$\eta = \left(\frac{T_c}{T_p}\right)_{H_2} + \left(\frac{T_c}{T_p}\right)_{CO} + \left(\frac{T_c}{T_p}\right)_{CH_4} = \frac{0.013}{11} + \frac{0.050}{11} + \frac{0.038}{6} = 0.012. \tag{133}$$

The achievable neutralization is sufficiently small for the operation of the electron cooler [34]. However, the neutralization is rather high when comparing it with the neighbouring sections of the HESR ring, see Figs. 19 - 22. This is due to the fact that clearing electrodes can only be installed outside of the 24 m long cooler section. In addition, the number of ions per meter is about a factor 125 larger since the neutralization refers to the sum of electron and antiproton beam.

We note that the neutralization in the EC could be reduced by removing the trapped ions by short interruptions of the electron beam (for instance a 2 $\mu$s interruption at 100 Hz). Such a scheme has been tested with great success at the Fermilab [35]. Then, it would be possible to extract the trapped ions with moderate electric fields using clearing electrodes inside of the electron cooler. Electric fields of about $(200\mathrm{V})/(0.2\mathrm{m}) = 1000$ V/m would be sufficient. To this end, one could use the nine beam position monitors in the electron cooler section.

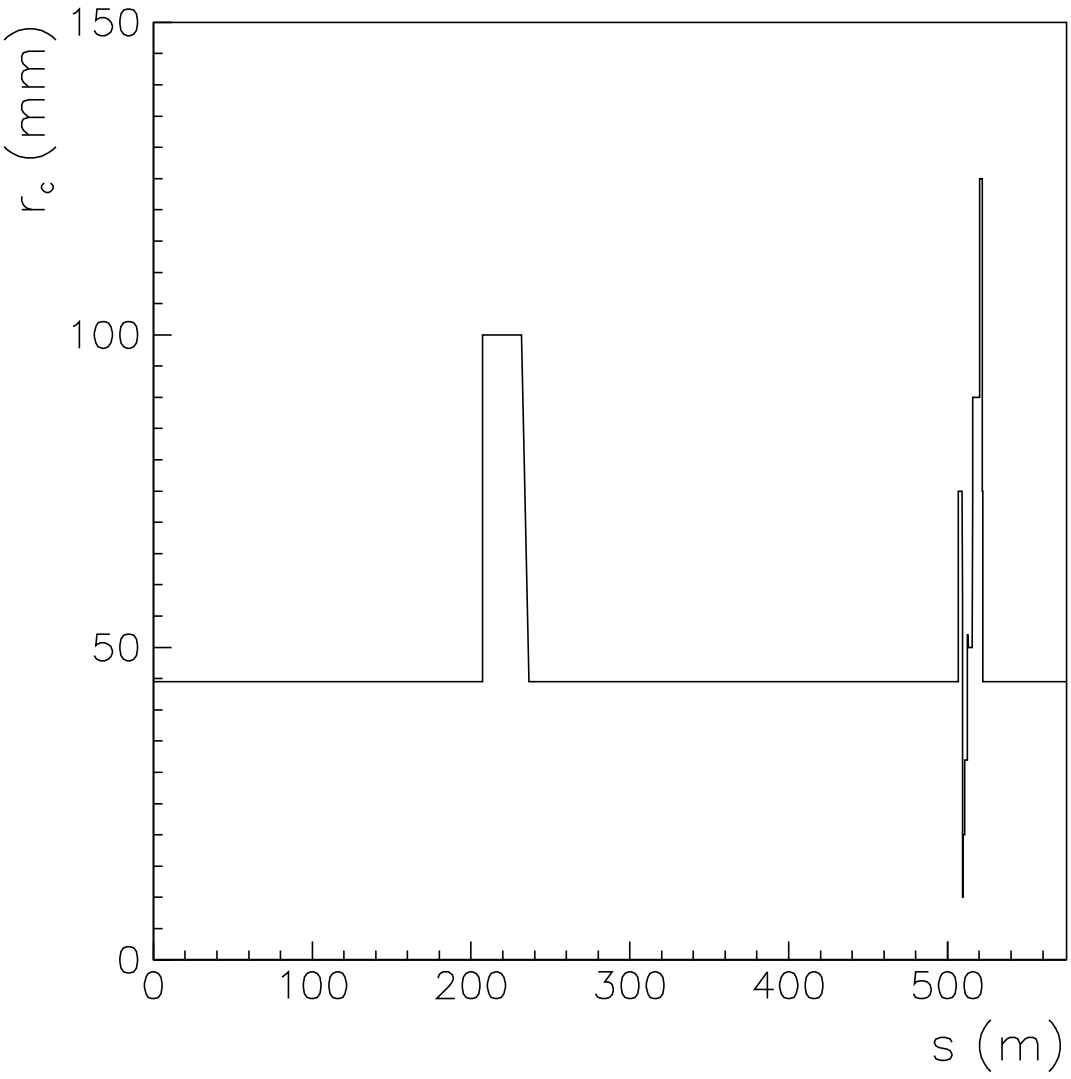


Fig. 23: Inner beam pipe radius $r_c(s)$ after installation of the electron cooler.

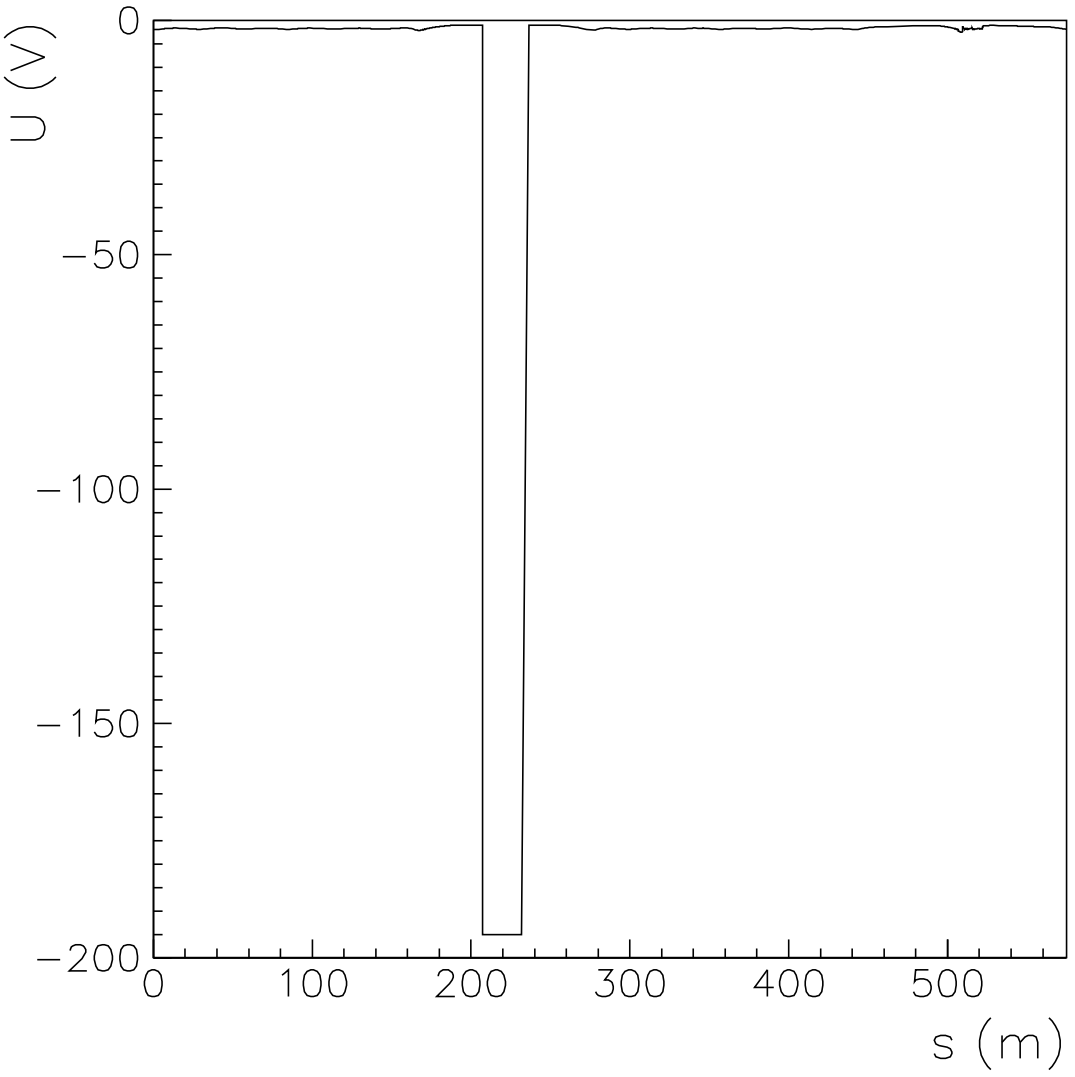


Fig. 24: Central potential $U(s)$ showing the large potential depth due to the electron beam.

## 15. Target Region

### 15.1 Problems

The problem of trapped ions is especially virulent in the region of the PANDA target.
(i) The local density of $H_2$ molecules is extremely high due to the pressure bump in the neighbourhood of the PANDA target, see Fig. 9. Near the target point the production time $T_p$ for $H_2^+$ ions decreases strongly from 6.4 s to about 0.1 ms, see Fig. 10.
(ii) The produced ions cannot escape in the transverse direction due to the high magnetic field of the PANDA target solenoid. The produced ions (mainly $H_2^+$ ions) gyrate around the magnetic field lines of the solenoid. They can only escape in the longitudinal direction along the magnetic field lines.
(iii) There is a 2 m long dipole spectrometer in the immediate neighbourhood of the PANDA solenoid.
(iv) There is a 5 m long compensation solenoid in front of the PANDA solenoid.
(v) There is a narrow beam waist in $x$- and $y$-direction at the target point. As a consequence the longitudinal electric field $E_s$ of the antiproton beam is directed towards the target point, both upstream and downstream, see Fig. 8. Thus, positive ions are accelerated towards the target point instead of being accelerated towards clearing electrodes at the entrance and exit of the target solenoid. Therefore, ion clearing by the longitudinal electric field of the beam is not possible.
(vi) The inner diameter of the beam pipe near the PANDA target amounts to 20 mm and 40 mm, respectively. There is no room for clearing electrodes. Apart from that, a direct transverse acceleration of trapped ions towards clearing electrodes using transverse electric fields is not possible due to the longitudinal magnetic field of the solenoid which causes a cyclotron motion around the field lines.
(vii) Ion clearing using beam shaking is not possible. Transverse ion oscillations are suppressed by the longitudinal magnetic field of the solenoid.

### 15.2 Possible solutions outside of the PANDA solenoid

The highly uniform part of the magnetic field of the PANDA solenoid extends over a distance of 1.5 m from the target point at $s = 509.481$ m to $s = 510.981$ m. Including the fringe fields, the magnetic field of the PANDA solenoid extends over a distance of 5.50 m from $s = 507.481$ m to $s = 512.981$ m. The high magnetic field of the PANDA solenoid (2.0 T) has two important advantages: (i) Transverse oscillations of trapped ions and the excitation of coherent ion-beam oscillations cannot occur in this region due to the longitudinal magnetic field. (ii) Due to the short production time of positive ions the antiproton beam is fully neutralized within a very short time period and the longitudinal electric field $E_s$ directed towards the target point disappears. The overshoot of ions which are produced continuously with a very high production rate can escape along the magnetic field lines towards the fringe field of the solenoid. In the fringe field region of the solenoid the ions follow adiabatically the magnetic field lines towards the beam pipe where they are neutralized, see Subsect. 9.5.

Thus, it is only necessary to provide clearing electrodes outside of the PANDA solenoid region. There, clearing times of $T_c < 1$ $\mu$s are needed in order achieve a neutralization of less than 0.1 %. This can be achieved with continuous clearing electrodes. However, it is necessary to take the additional constraints of the PANDA experiment into account. Clearing electrodes must not disturb the PANDA experiment.

In this context we mention the PANDA dipole spectrometer in the immediate neighbourhood of the PANDA solenoid which starts in the fringe field region of the solenoid and extends over 2 m from $s = 512.481$ m to $s = 514.481$ m. The PANDA dipole spectrometer is located in a region where the residual $H_2$ gas pressure is still rather high and the production time for $H_2^+$ ions is rather low. The mean cross-field drift velocities in longitudinal direction are very low and the beam is fully neutralized within a short period of time. Then, the overshoot of positive ions can escape along the vertical magnetic field lines towards the vacuum chamber. Summarizing, the beam is fully neutralized in the region of the dipole spectrometer, i.e. $\eta = 1$ without clearing electrodes inside of the dipole spectrometer

In addition, there is a compensation solenoid with opposite field direction which extends over 5.0 m from $s = 500.231$ m to $s = 505.231$ m. Here, we estimate the neutralization in the region of the compensation solenoid assuming that there are no clearing electrodes inside of the solenoid. Fortunately, the longitudinal electric field $E_s$ is unidirectional (directed in the positive direction). The trapped ions move along the magnetic field lines towards the fringe field of the compensation solenoid. There, the ions follow adiabatically the magnetic field lines towards the beam pipe where they are neutralized, see Subsect. 9.5. The mean clearing time $T_c$ depends on the strength of the longitudinal electric field. For $1.0 \cdot 10^{11}$ antiprotons the longitudinal electric field varies between 0.057 V/m and 0.11 V/m and the clearing time $T_c$ is dominated by the longitudinal acceleration of the ions. It yields for $H_2^+$ ions $T_c \approx 1.1$ ms and $\eta \approx 0.11$ in the region of the compensation solenoid. For $1.0 \cdot 10^{10}$ antiprotons the longitudinal electric field is about a factor of eight lower but the clearing time $T_c$ is still dominated by the longitudinal acceleration of the ions. It yields for $H_2^+$ ions $T_c \approx 3.0$ ms and $\eta \approx 0.29$ in the region of the compensation solenoid.

## 16. Stability Condition for Ion Oscillations

The barrier-bucket mode of operation produces a long bunch of length $L_1 = 0.9C$ followed by a short beam-free gap of length $L_2 = 0.1\,C$, with $L_1 + L_2$ equal to the circumference, $L_1 + L_2 = C$. The corresponding times are $t_1 = L_1/(\beta c)$ and $t_2 = L_2/(\beta c)$. The barrier-bucket bunch has a nearly constant linear charge density $\lambda$. Positive ions perform oscillations during the long time period $t_1$ in the negative potential well of the antiproton beam, see Sect. 18.1. During the short beam-free time gap $t_2$ the ions move freely in the direction of their momentary transverse velocity. We consider the stability condition assuming that the neutralization is negligibly small.

### 16.1 Stability condition assuming neutralization $\eta = 0$

During the beam-free time gap $t_2$, the focusing force is zero and the ions behave like in a drift space. The sequence of focusing and non-focusing can be represented by a transport matrix like the TWISS matrix in accelerators,

$$M_x = \begin{pmatrix} 1 & L_2 \\ 0 & 1 \end{pmatrix} \begin{pmatrix} \cos(\sqrt{k_x}L_1) & \sin(\sqrt{k_x}L_1)/\sqrt{k_x} \\ -\sqrt{k_x}\sin(\sqrt{k_x}L_1) & \cos(\sqrt{k_x}L_1) \end{pmatrix}, \tag{134}$$

$$M_y = \begin{pmatrix} 1 & L_2 \\ 0 & 1 \end{pmatrix} \begin{pmatrix} \cos(\sqrt{k_y}L_1) & \sin(\sqrt{k_y}L_1)/\sqrt{k_y} \\ -\sqrt{k_y}\sin(\sqrt{k_y}L_1) & \cos(\sqrt{k_y}L_1) \end{pmatrix}, \tag{135}$$

where $k_x$ and $k_y$ depend on the electric field components $E_x$ and $E_y$ of the antiproton beam,

$$\begin{aligned} k_x &= \frac{1}{(\beta c)^2}\frac{e^2 N_{\bar{p}}}{2\pi\epsilon_0 L_1 m\sigma_x(\sigma_x+\sigma_y)} \\ k_y &= \frac{1}{(\beta c)^2}\frac{e^2 N_{\bar{p}}}{2\pi\epsilon_0 L_1 m\sigma_y(\sigma_x+\sigma_y)}. \end{aligned} \tag{136}$$

The ion oscillation and therewith the ion trapping is stable in regions where

$$|\mathrm{Tr}(M_x)| \le 2 \quad \text{and} \quad |\mathrm{Tr}(M_y)| \le 2. \tag{137}$$

The ion oscillation becomes instable and the ions leave the potential well of the beam if

$$|\mathrm{Tr}(M_x)| > 2 \quad \text{and/or} \quad |\mathrm{Tr}(M_y)| > 2. \tag{138}$$

In passing, we note that the TWISS matrix could also be written in terms of $t_1$ and $t_2$,

$$\tilde{M}_x = \begin{pmatrix} 1 & t_2 \\ 0 & 1 \end{pmatrix} \begin{pmatrix} \cos(\sqrt{\tilde{k}_x}t_1) & \sin(\sqrt{\tilde{k}_x}t_1)/\sqrt{\tilde{k}_x} \\ -\sqrt{\tilde{k}_x}\sin(\sqrt{\tilde{k}_x}t_1) & \cos(\sqrt{\tilde{k}_x}t_1) \end{pmatrix}, \tag{139}$$

$$\tilde{M}_y = \begin{pmatrix} 1 & t_2 \\ 0 & 1 \end{pmatrix} \begin{pmatrix} \cos(\sqrt{\tilde{k}_y}t_1) & \sin(\sqrt{\tilde{k}_y}t_1)/\sqrt{\tilde{k}_y} \\ -\sqrt{\tilde{k}_y}\sin(\sqrt{\tilde{k}_y}t_1) & \cos(\sqrt{\tilde{k}_y}t_1) \end{pmatrix}, \tag{140}$$

where $\tilde{k}_x$ and $\tilde{k}_y$ depend on the electric field components $E_x$ and $E_y$ of the antiproton beam,

$$\begin{aligned} \tilde{k}_x &= \frac{e^2 N_{\bar{p}}}{2\pi\epsilon_0 L_1 m\sigma_x(\sigma_x+\sigma_y)} \\ \tilde{k}_y &= \frac{e^2 N_{\bar{p}}}{2\pi\epsilon_0 L_1 m\sigma_y(\sigma_x+\sigma_y)}. \end{aligned} \tag{141}$$

It should be noted that the calculations of $Tr(M_x)$ and $Tr(M_y)$ presented in Figs. 25 and 26 have been done assuming $1.0 \cdot 10^{11}$ antiprotons in the HESR ring. Instabilities with $|\mathrm{Tr}(M_{x,y})| > 2$ occur only at a few positions in the HESR ring. The regions of instability would be larger if the beam-free gap would be 20 % instead of 10 %,

In dipole magnets, vertical ion oscillations along the magnetic field lines are not hindered and instabilities due to $|Tr(M_y)| > 2$ are possible. In the $x$-direction dangerous oscillations are suppressed by the Lorentz force $q\vec{v} \times \vec{B}$ yielding cyclotron motions around the magnetic field lines, see subsection 8.2. Thus, instabilities due to $|Tr(M_x)| > 2$ cannot occur in dipole magnets. Therefore, we set $Tr(M_x) = 0$ in the region of dipole magnets, see Fig. 25.

In the region of solenoids, the transverse ion oscillations due to the electric field $\vec{E}$ of the antiproton beam are completely suppressed and an instability due to $|Tr(M_{x,y})| > 2$ cannot occur. This is due to the Lorentz force $q\vec{v} \times \vec{B}$ yielding a strong confinement in the transverse direction. The magnetic field of the solenoid and the electric field of the antiproton beam cause the modified cyclotron motion and the slow magnetron motion around the central axis (see subsection 9.3). Therefore, we set $Tr(M_x) = 0$ and $Tr(M_y) = 0$ in the region of solenoids, see Figs. 25 and 26. It is interesting to note that the spectrometer solenoid near the PANDA target prevents $|Tr(M_{x,y})| > 2$ instabilities which would occur without solenoid. Therefore, the huge amount of $H_2^+$ ions near the PANDA target cannot not be detrapped by $|Tr(M_{x,y})| > 2$ instabilities.

In order to study the basic cause for instabilities a program has been written where the harmonic oscillation in the potential well of the antiproton beam is periodically interrupted during the beam-free time gap. A detailed analysis shows that instabilities occur for a beam-free time gap of 10 % if the 'tune numbers' of the ion oscillations, $q_x = \omega_x/\omega_0$ and/or $q_y = \omega_y/\omega_0$, are located in certain intervals, i.e. if $0.50 < q_x < 0.55$, $1.0 < q_x < 1.1$, $1.5 < q_x < 1.65$, etc. and/or $0.50 < q_y < 0.55$, $1.0 < q_y < 1.1$, $1.5 < q_y < 1.65$, etc.. If the ion oscillation is instable the oscillation amplitudes rise quickly and the ions are detrapped. For instance for $q_y = 0.53$ only 21 oscillations are necessary in order to reach amplitudes of more than 50 mm.

It should be noted that ions with larger mass like for instance $CO^+$ or $N_2^+$ ions perform always stable oscillations since the focusing strengths are nearly an order of magnitude lesser. It should also be noted that instabilities with $|Tr(M_{x,y})| > 2$ do not occur at all for $1.0 \cdot 10^{10}$ antiprotons in the ring since the electric fields and the focusing strengths are by a factor of ten lesser.

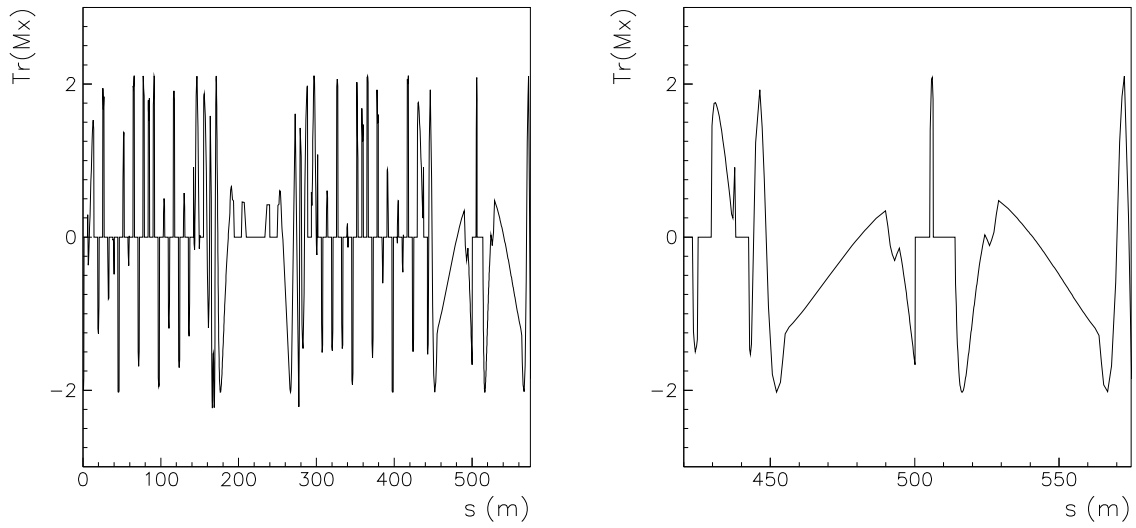


Fig. 25: Tr($M_x$) vs. $s$ with Tr($M_x$) $= 0$ in the region of dipole magnets and solenoids. A beam-free gap of 10 $\%$ and the standard optics are assumed with $p_{\bar{p}} = 15$ GeV/c, $N_{\bar{p}} = 1.0 \cdot 10^{11}$ and $\eta = 0$. Left: the complete HESR ring from $s = 0$ m to $s = 575$ m. Right: the PANDA target region from $s = 420$ m to $s = 575$ m. The trapped ions are detrapped if $|TrM_x| > 2$.

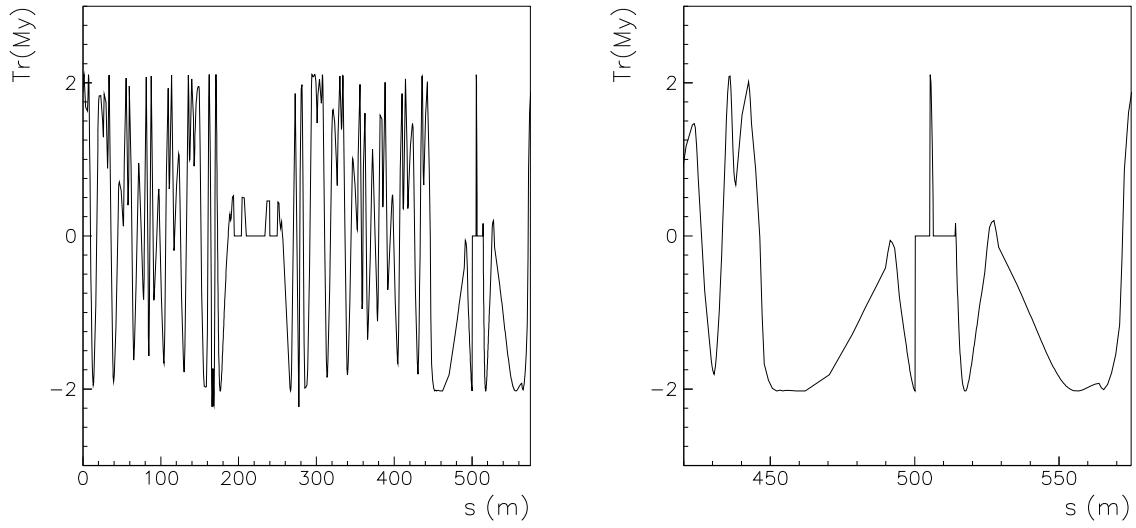


Fig. 26: Tr($M_y$) vs. $s$ with Tr($M_y$) $= 0$ in the region of solenoids. A beam-free gap of 10 $\%$ and the standard optics are assumed with $p_{\bar{p}} = 15$ GeV/c, $N_{\bar{p}} = 1.0 \cdot 10^{11}$ and $\eta = 0$. Left: the complete HESR ring from $s = 0$ m to $s = 575$ m. Right: the PANDA target region from $s = 420$ m to $s = 575$ m. The trapped ions are detrapped if $|TrM_y| > 2$.

### 16.2 Stability condition assuming neutralization $\eta > 0$

If positive ions are trapped in the potential well of the antiproton beam the neutralization $\eta$ is nonzero. The corresponding TWISS matrix may be written as the product of a focusing and defocusing matrix,

$$\begin{aligned} M_x &= \begin{pmatrix} \cosh(\sqrt{k_{2,x}}L_2) & \sinh(\sqrt{k_{2,x}}L_2)/\sqrt{k_{2,x}} \\ \sqrt{k_{2,x}}\sinh(\sqrt{k_{2,x}}L_2) & \cosh(\sqrt{k_{2,x}}L_2) \end{pmatrix} \\ &\cdot \begin{pmatrix} \cos(\sqrt{k_{1,x}}L_1) & \sin(\sqrt{k_{1,x}}L_1)/\sqrt{k_{1,x}} \\ -\sqrt{k_{1,x}}\sin(\sqrt{k_{1,x}}L_1) & \cos(\sqrt{k_{1,x}}L_1) \end{pmatrix}, \end{aligned} \tag{142}$$

$$\begin{aligned} M_y &= \begin{pmatrix} \cosh(\sqrt{k_{2,y}}L_1) & \sinh(\sqrt{k_{2,y}}L_1)/\sqrt{k_{2,y}} \\ \sqrt{k_{2,y}}\sinh(\sqrt{k_{2,y}}L_1) & \cosh(\sqrt{k_{2,y}}L_1) \end{pmatrix} \\ &\cdot \begin{pmatrix} \cos(\sqrt{k_{1,y}}L_1) & \sin(\sqrt{k_{1,y}}L_1)/\sqrt{k_{1,y}} \\ -\sqrt{k_{1,y}}\sin(\sqrt{k_{1,y}}L_1) & \cos(\sqrt{k_{1,y}}L_1) \end{pmatrix}, \end{aligned} \tag{143}$$

where

$$k_{1,x} = \frac{1}{(\beta c)^2}\frac{e^2 N_{\bar{p}}(1-\eta)}{2\pi\epsilon_0 L_1 m\sigma_x(\sigma_x+\sigma_y)}, \tag{144}$$

$$k_{1,y} = \frac{1}{(\beta c)^2}\frac{e^2 N_{\bar{p}}(1-\eta)}{2\pi\epsilon_0 L_1 m\sigma_y(\sigma_x+\sigma_y)}, \tag{145}$$

$$k_{2,x} = \frac{1}{(\beta c)^2}\frac{e^2 N_{\bar{p}}\eta}{2\pi\epsilon_0 L_2 m\sigma_x(\sigma_x+\sigma_y)}, \tag{146}$$

$$k_{2,y} = \frac{1}{(\beta c)^2}\frac{e^2 N_{\bar{p}}\eta}{2\pi\epsilon_0 L_2 m\sigma_y(\sigma_x+\sigma_y)}. \tag{147}$$

## 17. Tune Shift and Tune Spread

### 17.1 Tune shifts due to trapped ions

The trapped ions affect the betatron oscillations of the antiproton beam particles. The space charge of the trapped ions yields a focusing force whereas the beam space charge yields a defocusing force. Assuming identical transverse distributions (elliptic and bi-Gaussian) of the beam particles and the trapped ions the maximum total tune shifts[6] $\Delta Q_x$ and $\Delta Q_y$ are given in linear approximation by

$$\begin{aligned} \Delta Q_x &= \frac{N_{\bar{p}} r_p}{2\pi\beta^2\gamma}\frac{1}{C}\int_0^C \frac{\beta_x(s)}{\sigma_x(s)[\sigma_x(s)+\sigma_y(s)]}\left(\eta(s)-\frac{1}{\gamma^2}\right)\mathrm{d}s, \\ \Delta Q_y &= \frac{N_{\bar{p}} r_p}{2\pi\beta^2\gamma}\frac{1}{C}\int_0^C \frac{\beta_y(s)}{\sigma_y(s)[\sigma_x(s)+\sigma_y(s)]}\left(\eta(s)-\frac{1}{\gamma^2}\right)\mathrm{d}s. \end{aligned} \tag{148}$$

Here, $r_p = 1.5347 \cdot 10^{-18}$ m is the classical proton radius. The integral indicates the averaging around the ring.

The term with $1/\gamma^2 = 1 - \beta^2$ represents the effects of the electric and magnetic forces from the $\bar{p}$ beam charges and currents and the term with $\eta$ represents the effects of the electric forces from the positive ion charges. The ions, which are practically motionless contribute only a focusing electric field. Without trapped ions ($\eta = 0$) the tune shifts are negative. If the space charge effects are dominated by trapped ions the tune shifts are positive. Thus, measuring the tune shifts provides one means to estimate the average neutralization in the HESR ring.

The equation (148) gives the maximum tune shift. Beam particles with large betatron amplitudes at the edge of the beam distribution experience less focusing and defocusing (zero at the limit). Therefore, the $\Delta Q_x$ and $\Delta Q_y$ represent also approximately the tune spreads.

In order to estimate the effects of trapped ions we calculate the maximum tune shifts and tune spreads by solving numerically the integral expression (148). We take as an example calculations assuming $N_{\bar{p}} = 1.0 \cdot 10^{11}$ at 15 GeV/c, a UHV vacuum pressure of $1.0 \cdot 10^{-9}$ mbar with 80 % $H_2$ and 20 % CO outside of the target pressure bump, ion clearing using longitudinal acceleration $a_s$ by the longitudinal electric fields in the straight sections and cross-field drift velocities in the dipole magnets. The electron cooler is also taken into account. To this end we assume the neutralization $\eta(s)$ as a function of $s$ as estimated in Sect. 13. and shown in the top panel of Fig. 22. In addition we calculate also separately the maximum tune shifts $\Delta Q_x^{ion}$ and $\Delta Q_y^{ion}$ caused by the ion space charges taking only the $\eta(s)$ term, and the $\Delta Q_x^{beam}$ and $\Delta Q_y^{beam}$ caused by the beam space charge taking only the $1/\gamma^2$ term. They are related by $\Delta Q_{x,y} = \Delta Q_{x,y}^{ion} + \Delta Q_{x,y}^{beam}$. And we calculate numerically the average neutralization $\bar{\eta}$ as given by

$$\bar{\eta} = \frac{1}{C}\int_0^C \eta(s)\mathrm{d}s. \tag{149}$$

The results are listed in Table 20.

It is interesting to study what happens if we assume full neutralization in the HESR ring, i.e. $\eta = 1.0$ everywhere. Full neutralization can be prepared approximately by switching off all clearing electrodes. The resulting maximum tune shifts are listed in Table 21.

[6] Often this tune shift is called incoherent tune shift since it refers to the incoherent motion of the beam particles.

Table 20: Maximum tune shifts and tune spreads for $\eta(s)$ shown in the bottom panel of Fig. 22 with $N_{\bar{p}} = 1.0 \cdot 10^{11}$ at 15.0 GeV/c.

| $\Delta Q_x^{ion}$ | $\Delta Q_x^{beam}$ | $\Delta Q_x$ | $\Delta Q_y^{ion}$ | $\Delta Q_y^{beam}$ | $\Delta Q_y$ | $\bar{\eta}$ |
|---|---|---|---|---|---|---|
| $1.51 \cdot 10^{-4}$ | $-2.05 \cdot 10^{-5}$ | $1.30 \cdot 10^{-4}$ | $1.50 \cdot 10^{-4}$ | $-1.93 \cdot 10^{-5}$ | $1.31 \cdot 10^{-4}$ | $2.97 \cdot 10^{-2}$ |

Table 21: Maximum tune shifts and tune spreads for $N_{\bar{p}} = 1.0 \cdot 10^{11}$ and $\eta = 1.0$ at 15.0 GeV/c.

| $\Delta Q_x^{ion}$ | $\Delta Q_x^{beam}$ | $\Delta Q_x$ | $\Delta Q_y^{ion}$ | $\Delta Q_y^{beam}$ | $\Delta Q_y$ | $\bar{\eta}$ |
|---|---|---|---|---|---|---|
| $5.26 \cdot 10^{-3}$ | $-2.05 \cdot 10^{-5}$ | $5.24 \cdot 10^{-3}$ | $4.96 \cdot 10^{-3}$ | $-1.93 \cdot 10^{-5}$ | $4.94 \cdot 10^{-3}$ | 1.0 |

### 17.2 Estimate of tune shifts

A simple order of magnitude check can be performed [20] using

$$\Delta Q_{x,y} \approx \frac{N_{\bar{p}} r_p}{2\pi\beta} \frac{1}{2\epsilon_{n,rms}} \left( \bar{\eta} - \frac{1}{\gamma^2} \right), \tag{150}$$

where $\epsilon_{n,rms}$ is the normalized rms emittance. With $N_{\bar{p}} = 1 \cdot 10^{11}$ and $\epsilon_{n,rms} = (10/3.5)^{0.8} \cdot 1.0$ mm mrad = 2.32 mm mrad (see Sect. 2.) we get

$$\begin{aligned} \Delta Q_{x,y}^{ion} &\approx 0.00526 \frac{1}{\beta} \bar{\eta}, \\ \Delta Q_{x,y}^{beam} &\approx 0.00526 \frac{1}{\beta} \left( -\frac{1}{\gamma^2} \right), \\ \Delta Q_{x,y} &\approx 0.00526 \frac{1}{\beta} \left( \bar{\eta} - \frac{1}{\gamma^2} \right). \end{aligned} \tag{151}$$

These equations can be used in the full momentum range of HESR between 1.5 and 15 GeV/c in order to get a quick estimate.

They yield for $\bar{\eta} = 0.0297$ at 15 GeV/c

$$\begin{aligned} \Delta Q_{x,y}^{ion} &\approx 1.57 \cdot 10^{-4}, \\ \Delta Q_{x,y}^{beam} &\approx -2.05 \cdot 10^{-5} \\ \Delta Q_{x,y} &\approx 1.37 \cdot 10^{-4}. \end{aligned} \tag{152}$$

These values are in rather good agreement with the values in Tab. 20.

Assuming full neutralization ($\bar{\eta} = 1.0$) at 15 GeV/c yields

$$\begin{aligned} \Delta Q_{x,y}^{ion} &\approx 5.26 \cdot 10^{-3}, \\ \Delta Q_{x,y}^{beam} &\approx -2.05 \cdot 10^{-5} \\ \Delta Q_{x,y} &\approx 5.24 \cdot 10^{-3}. \end{aligned} \tag{153}$$

These values are in rather good agreement with the values in Tab. 21.

## 18. Coherent Instabilities

Transverse coherent instabilities have been observed at several antiproton machines. There, collective oscillations of the beam center (dipole mode) or the beam shape (quadrupole mode) grow exponentially due to the interaction of the beam with the trapped ions. The most dangerous mode is the dipole mode, i.e. the coherent oscillation of the beam center. The coherent instabilities can be estimated using the two-beam instability theory developed by Koshkarev and Zenkevich [9], Laslett, Sessler and Möhl [10] Keil and Zotter [11] and Alves-Pires et al. [13]. Additional information can be found in the thesis of Zhou [16] and in the references [12, 20].

Trapped ions oscillate in the electric field of the antiproton beam. They cause forces back on the beam. Vice versa, the beam disturbs the motion of the ions which interact with trailing beam particles. Thus, the beam is forced to interact coherently with itself. This phenomenon is very similar to the interaction between beam and wake fields which are described by the machine impedance $Z(\omega)$. Here, $\omega$ is the angular frequency of the resulting coherent oscillation. The effect of trapped ions can be described by some extra impedance $Z_i(\omega)$. Since the real part of $Z(\omega) + Z_i(\omega)$ is positive the fast-wave mode with the sideband frequency $\omega = (n + Q)\omega_0$ is always stable [16]. Here, $\omega_0$ is the revolution frequency, $Q$ the betatron tune and $n$ an integer with $n > -Q$. Without Landau damping, i.e. without any frequency spreads the slow-wave mode with $\omega = (n - Q)\omega_0$ is always unstable. Here, $n$ is an integer with $n > Q$. Thus, dangerous coherent oscillations can occur if the trapped ions oscillate at frequencies near the sideband frequencies $(n - Q)\omega_0$.

### 18.1 Ion oscillations

Ions trapped in the potential well of the antiproton beam perform oscillations. Using the linear approximation of the electric field the equation of motion reads for an ion of mass $m_i$ and charge $Z_i e$

$$\begin{aligned}
\frac{\mathrm{d}^2 x_i}{\mathrm{d}t^2} &= \frac{Z_i e}{m_i} E_x = -\frac{e^2 N_{\bar{p}}}{2\pi\epsilon_0 L_1} \frac{Z_i}{m_i} \frac{1-\eta}{\sigma_x(\sigma_x+\sigma_y)} x_i = -q_x^2 \omega_0^2 x_i \\
\frac{\mathrm{d}^2 y_i}{\mathrm{d}t^2} &= \frac{Z_i e}{m_i} E_y = -\frac{e^2 N_{\bar{p}}(1-\eta)}{2\pi\epsilon_0 L_1 m \sigma_y(\sigma_x+\sigma_y)} y_i = -q_y^2 \omega_0^2 y_i.
\end{aligned} \tag{154}$$

Here, $m_i \approx A_i m_p$ is the mass of the ion and $Z_i$ is the charge number of the ionization where $Z_i = 1$ for singly charged ions, $Z_i = 2$ for doubly charged ions and so on. The other quantities are defined in Sect. 3.. The transverse and longitudinal velocities of the ion are so small that the weak Lorentz force due to the magnetic field of the beam can be neglected. The ions perform harmonic oscillations. The frequencies $f_x$ and $f_y$ of the ion oscillations ('bounce frequency') read

$$\begin{aligned}
f_x &= \frac{1}{2\pi}\sqrt{\frac{Z_i e^2 N_{\bar{p}}(1-\eta)}{2\pi\epsilon_0 L_1 m_i \sigma_x(\sigma_x+\sigma_y)}} = q_x f_0 \\
f_y &= \frac{1}{2\pi}\sqrt{\frac{Z_i e^2 N_{\bar{p}}(1-\eta)}{2\pi\epsilon_0 L_1 m_i \sigma_y(\sigma_x+\sigma_y)}} = q_y f_0.
\end{aligned} \tag{155}$$

where $\eta$ is the neutralization factor, $\omega_0$ the angular revolution frequency and $f_0$ the revolution frequency of the antiprotons ($f_0 = 520.2$ kHz at 15 GeV/c) and $q_x$, $q_y$ the 'tune numbers' of the

ion oscillations. These equations can also be written in the following form,

$$
\begin{aligned}
q_x^2 &= \frac{1}{\omega_0^2}\frac{Z_i e^2 N_{\bar{p}}(1-\eta)}{2\pi\epsilon_0 L_1 m_i \sigma_x(\sigma_x+\sigma_y)} = \frac{2R^2}{L_1}\frac{N_{\bar{p}} r_p}{\beta^2}\frac{Z_i}{A_i}\frac{1-\eta}{\sigma_x(\sigma_x+\sigma_y)}, \\
q_y^2 &= \frac{1}{\omega_0^2}\frac{Z_i e^2 N_{\bar{p}}(1-\eta)}{2\pi\epsilon_0 L_1 m_i \sigma_y(\sigma_x+\sigma_y)} = \frac{2R^2}{L_1}\frac{N_{\bar{p}} r_p}{\beta^2}\frac{Z_i}{A_i}\frac{1-\eta}{\sigma_y(\sigma_x+\sigma_y)}.
\end{aligned}
\tag{156}
$$

Here, $r_p = e^2/(4\pi\epsilon_0 m_p c^2) = 1.535 \cdot 10^{-18}$ m is the classical proton radius.

In the region of solenoids the ion motion is modified by the presence of the longitudinal magnetic field $B$. The resulting motion can be described by a superposition of a fast modified cyclotron motion around the field lines (large angular frequency $\omega_+$ and small radius $r_+$) and a slow magnetron motion around the beam center (angular frequency $\omega_-$ and radius $r_-$), see Sect. 9.3. Direct transverse oscillations in $x$- and $y$-direction are not possible. Therefore, we set $q_x = 0$ and $q_y = 0$ in the region of solenoids.

In the region of dipole magnets the transverse ion motion in $x$-direction is strongly affected by the magnetic field $B_y$. The ions perform a fast cyclotron motion around the vertical field lines. This motion is modified by the transverse electric field component $E_x$ of the antiproton beam. The resulting $\vec{E} \times \vec{B}/B^2$ cross-field drift velocity is directed in the longitudinal direction. A transverse oscillation in $x$-direction is not possible. Therefore, we set $q_x = 0$ in the region of dipole magnets.

The resulting 'tune numbers' $q_x$ and $q_y$ depend on the position $s$ in the HESR ring since the rms envelopes $\sigma_x$ and $\sigma_y$ and the neutralization $\eta$ are functions of $s$. They are shown in Figs. 27-38 for $H^+$, $H_2^+$ and $CO^+$ ions at four beam momenta (1.5 GeV/c, 3.825 GeV/c, 8.889 GeV/c and 15.0 GeV/c). These typical examples are calculated assuming a local beam neutralization $\eta(s)$ as shown in the top panel of Fig. 22. The dotted lines indicate the resonance frequencies $(n - Q_x)$ and $(n - Q_y)$ where coherent oscillations of the $\bar{p}$ beam and the trapped ions can occur. The ring-averaged root mean square values $q_x^{rms}$ and $q_y^{rms}$ are indicated by the dashed lines.

The danger of coherent oscillations is especially high if the rms values of $q_x$ and/or $q_y$ are close to a resonance line. This occurs for instance for $q_y(H^+)$ near 1.5 GeV/c, $q_x(H^+)$ near 3.825 GeV/c, for $q_y(H_2^+)$ near 3.825 GeV/c and for $q_x(H_2^+)$ near 8.889 GeV/c. The 'tune numbers' of $CO^+$ ions are always below the critical resonance lines $(8 - Q_x)$ and $(8 - Q_y)$.

We note that the 'tune numbers' $q_x$ and $q_y$ depend not only on the ion mass, ion charge and beam momentum but also on the number of stored antiprotons which determines the depth of the potential well and the electric field strengths $E_x$ and $E_y$. The examples shown in Figs. 27-38 are calculated assuming $N_{\bar{p}} = 1.0 \cdot 10^{11}$ antiprotons in the HESR ring. The 'tune numbers' $q_{x,y}$ are proportional to $\sqrt{N_{\bar{p}}/[\sigma_{x,y}(\sigma_x + \sigma_y)]}$. The beam widths $\sigma_{x,y}$ are proportional to $N_{\bar{p}}^{2/5}$ (see Sect. 2.). Therefore, we get $q_{x,y} \propto \sqrt{N_{\bar{p}}^{1/5}}$, and the 'tune numbers' for $1.0 \cdot 10^{10}$ antiprotons are by a factor $\sqrt{10^{1/5}} = 1.26$ lower than those shown in Figs.27 - 38.

We mention that the bounce frequencies of the trapped ions decrease with increasing oscillation amplitude. This effect is due to the nonlinearity of the electric field of a Gaussian beam distribution. The non-linear detuning of the ion bounce frequency plays an important role when resonant transverse shaking is applied in order to remove the ions out of the beam (see Sect. 19.).

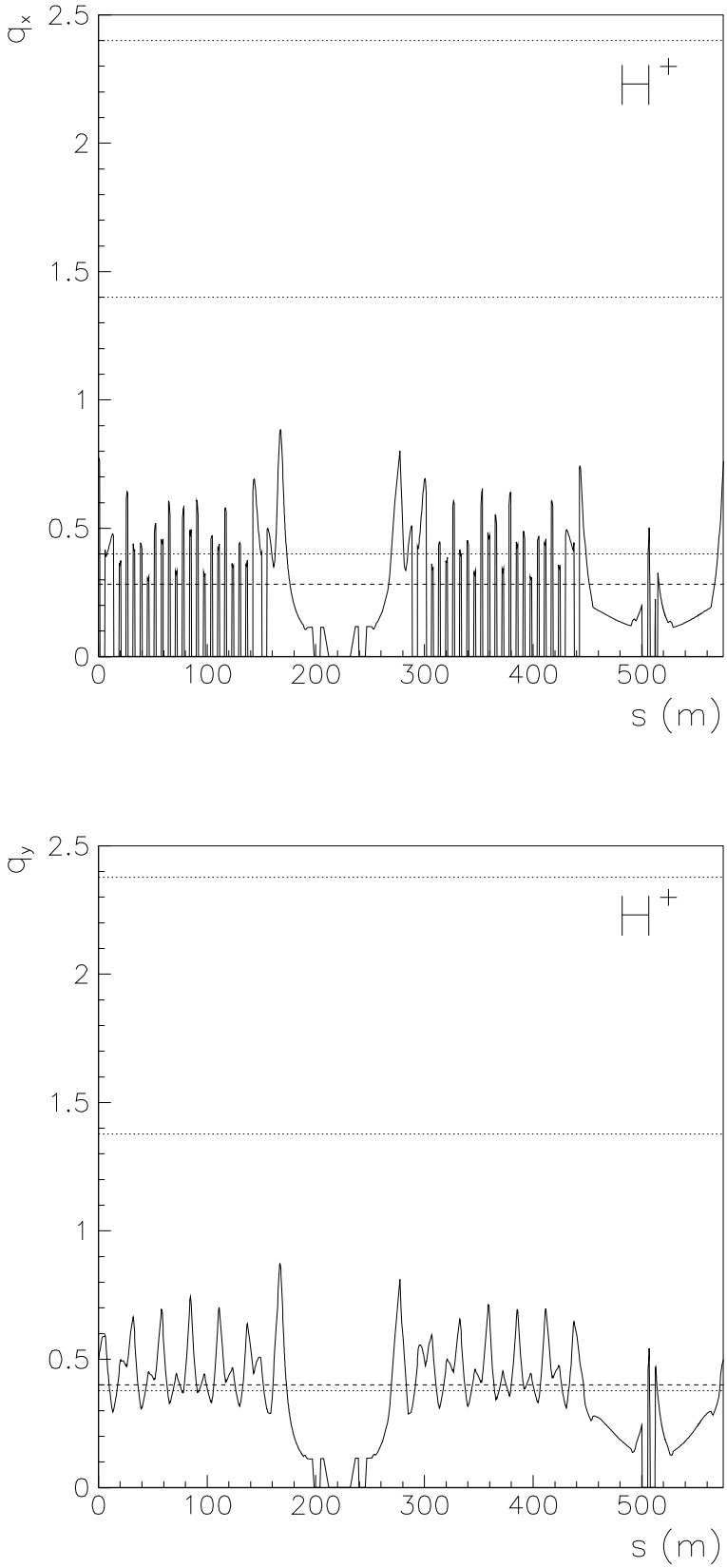


Fig. 27: Bounce frequencies of transverse $\mathbf{H}^+$ **ion oscillations** represented as 'tune numbers' $q_x = f_x/f_0$ and $q_y = f_y/f_0$, assuming $p_{\bar{p}} =$ **1.5 GeV/c**, $N_{\bar{p}} = 1.0 \cdot 10^{11}$, $\eta(s)$ as in top panel of Fig.22. The dotted lines represent the resonance lines $(n - Q_x)$ and $(n - Q_y)$ for $n = 8$, $n = 9$ and $n = 10$, yielding 0.4005, 1.4005 and 2.4005 for $(n - Q_x)$ and 0.3784, 1.3784 and 2.3784 for $(n - Q_y)$, respectively. The dashed lines represent the ring-averaged rms values $q_x^{rms} = 0.282$ and $q_y^{rms} = 0.401$. **Top**: $q_x$. **Bottom**: $q_y$.

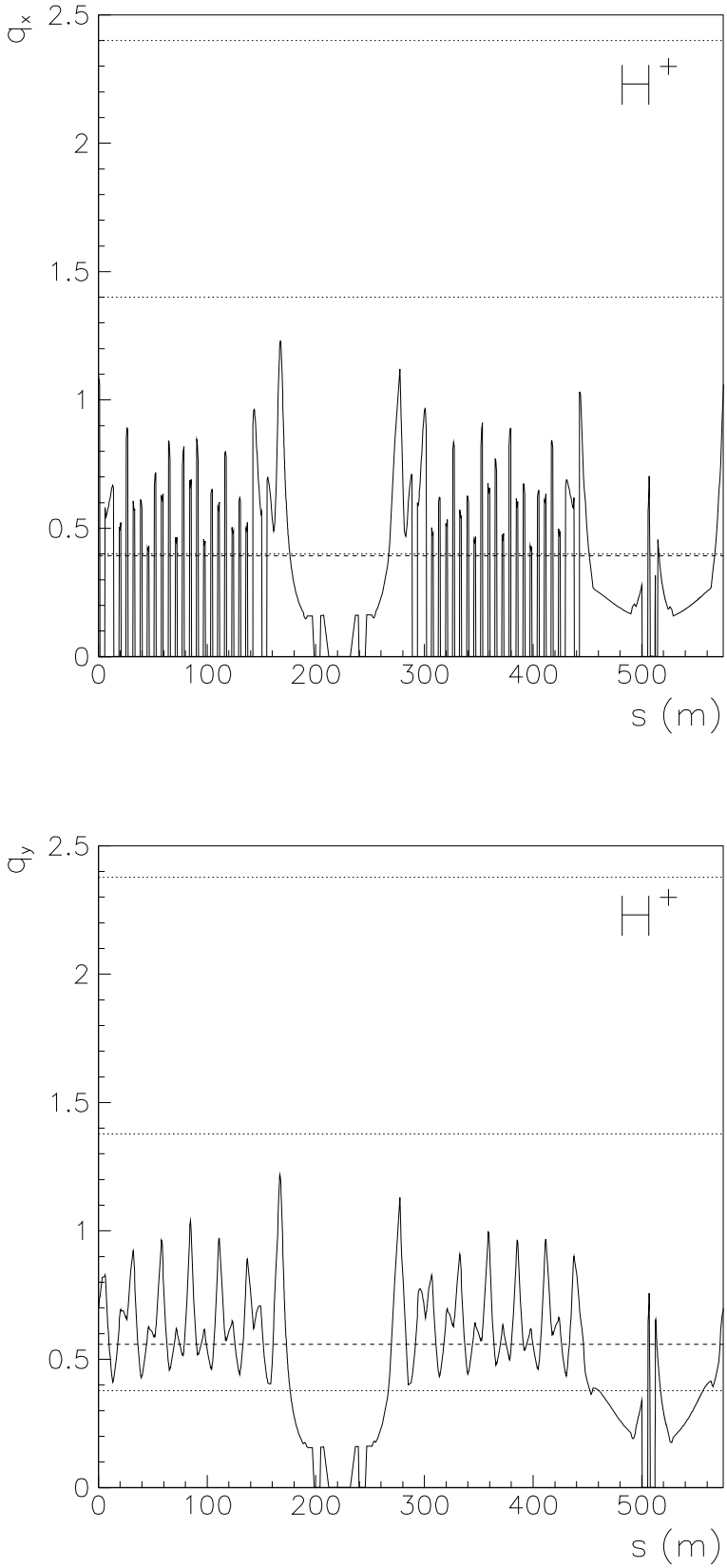


Fig. 28: Bounce frequencies of transverse $\mathbf{H}^+$ **ion oscillations** represented as 'tune numbers' $q_x = f_x/f_0$ and $q_y = f_y/f_0$, assuming $p_{\bar{p}}$ = **3.825 GeV/c**, $N_{\bar{p}} = 1.0 \cdot 10^{11}$, $\eta(s)$ as in top panel of Fig.22. The dotted lines represent the resonance lines $(n - Q_x)$ and $(n - Q_y)$ for $n = 8$, $n = 9$ and $n = 10$, yielding 0.4005, 1.4005 and 2.4005 for $(n - Q_x)$ and 0.3784, 1.3784 and 2.3784 for $(n - Q_y)$, respectively. The dashed lines represent the ring-averaged rms values $q_x^{rms} = 0.393$ and $q_y^{rms} = 0.558$. **Top**: $q_x$. **Bottom**: $q_y$.

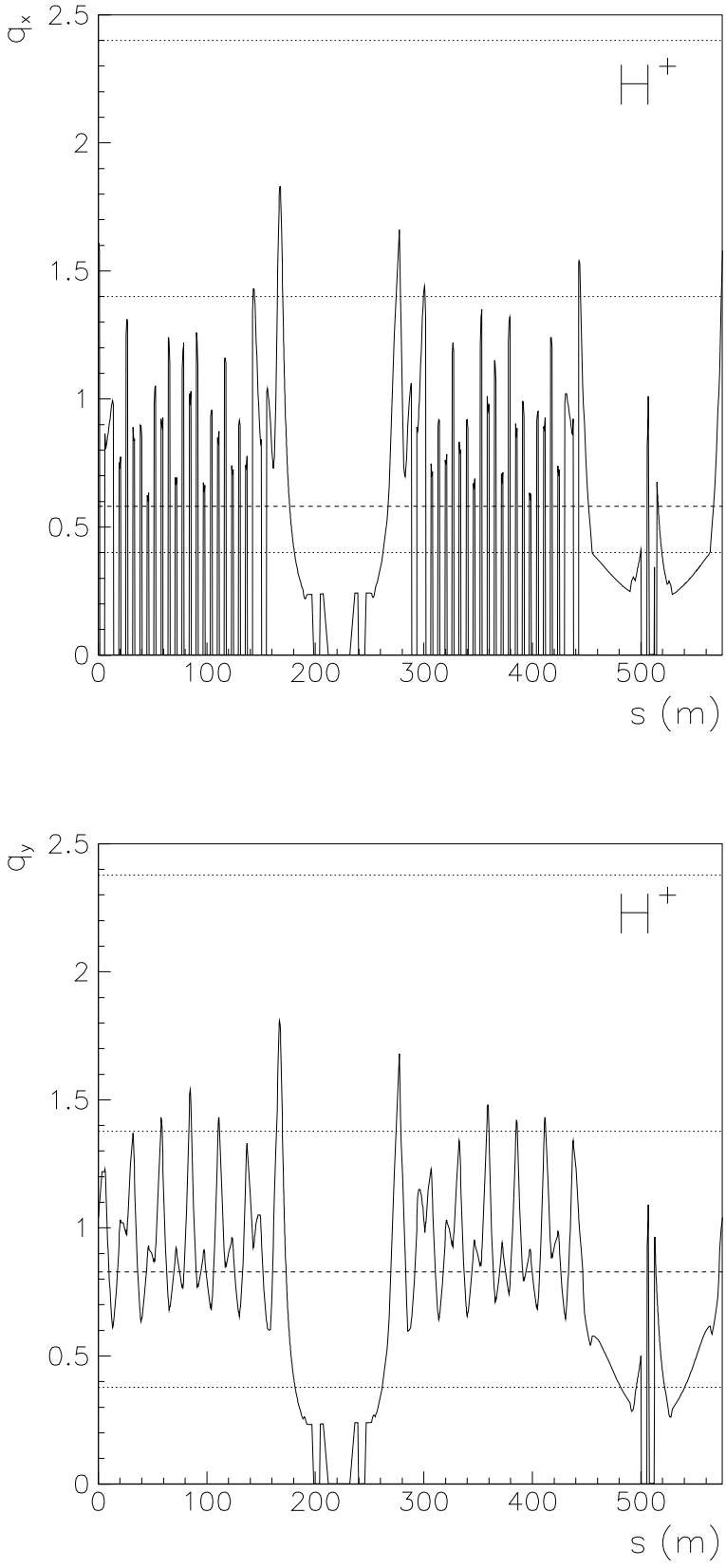


Fig. 29: Bounce frequencies of transverse $\mathbf{H}^+$ **ion oscillations** represented as 'tune numbers' $q_x = f_x/f_0$ and $q_y = f_y/f_0$, assuming $p_{\bar{p}}$ = **8.889 GeV/c**, $N_{\bar{p}} = 1.0 \cdot 10^{11}$, $\eta(s)$ as in top panel of Fig.22. The dotted lines represent the resonance lines $(n - Q_x)$ and $(n - Q_y)$ for $n = 8$, $n = 9$ and $n = 10$, yielding 0.4005, 1.4005 and 2.4005 for $(n - Q_x)$ and 0.3784, 1.3784 and 2.3784 for $(n - Q_y)$, respectively. The dashed lines represent the ring-averaged rms values $q_x^{rms} = 0.581$ and $q_y^{rms} = 0.829$. **Top**: $q_x$. **Bottom**: $q_y$.

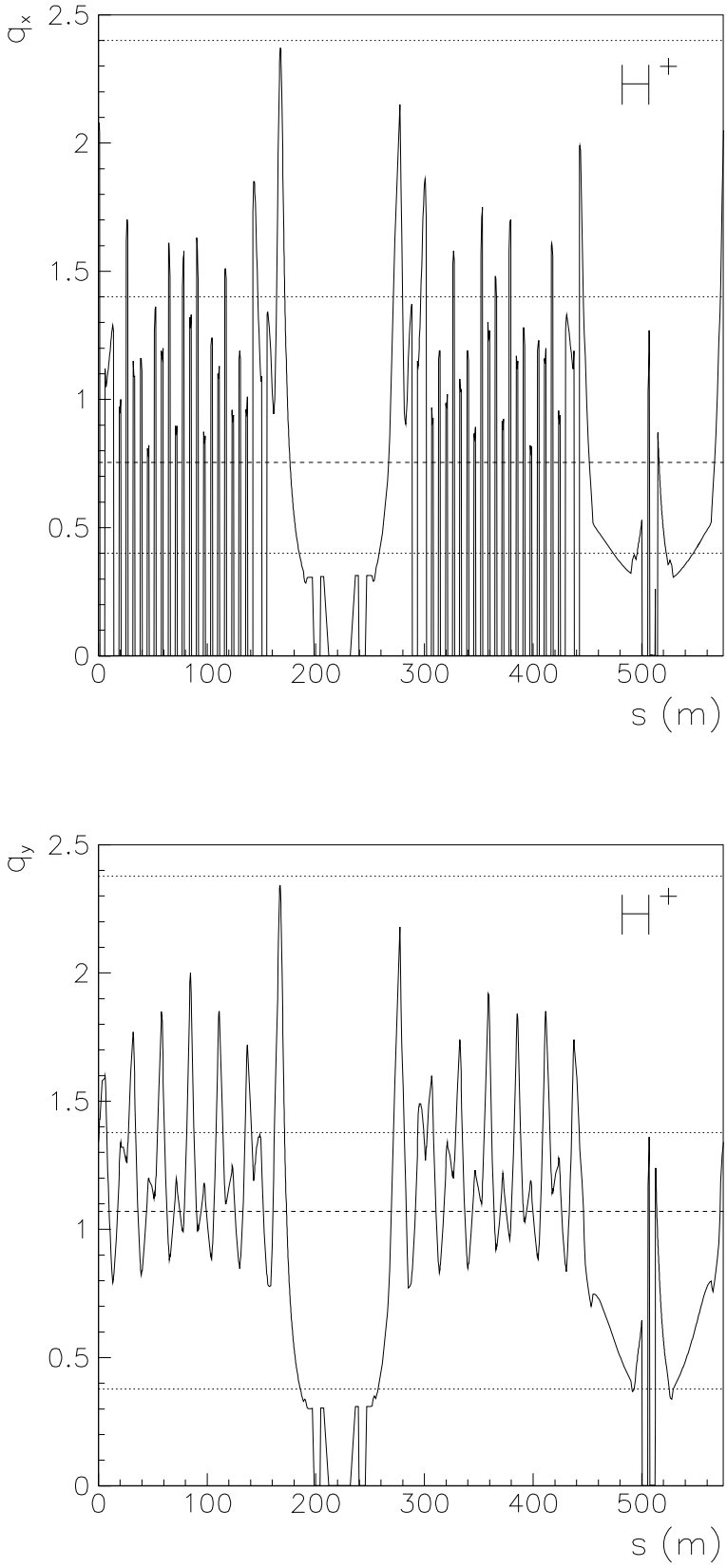


Fig. 30: Bounce frequencies of transverse $\mathbf{H^+}$ **ion oscillations** represented as 'tune numbers' $q_x = f_x/f_0$ and $q_y = f_y/f_0$, assuming $p_{\bar{p}}$ = **15.0 GeV/c**, $N_{\bar{p}} = 1.0 \cdot 10^{11}$, $\eta(s)$ as in top panel of Fig.22. The dotted lines represent the resonance lines $(n - Q_x)$ and $(n - Q_y)$ for $n = 8$, $n = 9$ and $n = 10$, yielding 0.4005, 1.4005 and 2.4005 for $(n - Q_x)$ and 0.3784, 1.3784 and 2.3784 for $(n - Q_y)$, respectively. The dashed lines represent the ring-averaged rms values $q_x^{rms} = 0.754$ and $q_y^{rms} = 1.07$. **Top**: $q_x$. **Bottom**: $q_y$.

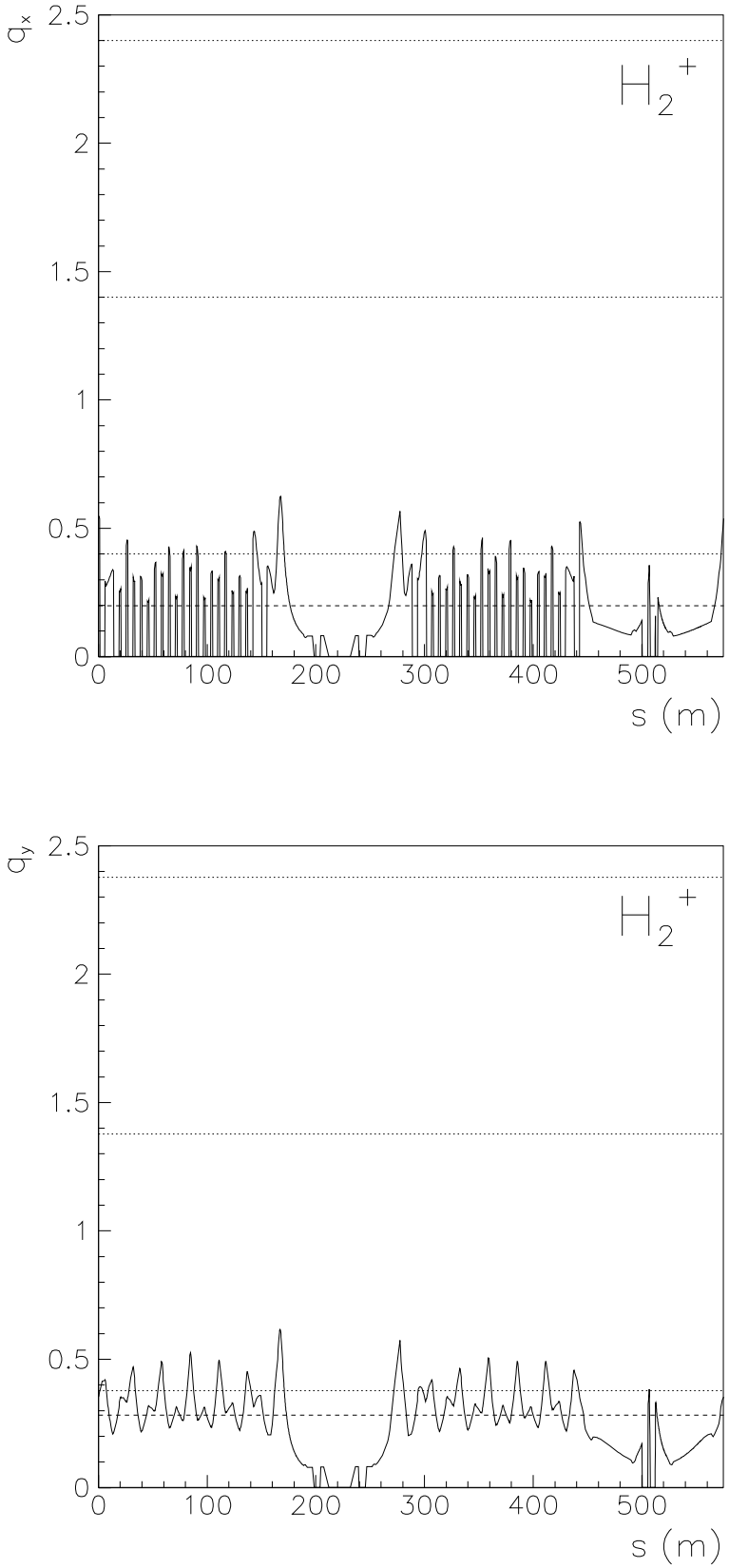


Fig. 31: Bounce frequencies of transverse $\mathbf{H}_2^+$ **ion oscillations** represented as 'tune numbers' $q_x = f_x/f_0$ and $q_y = f_y/f_0$, assuming $p_{\bar{p}} =$ **1.5 GeV/c**, $N_{\bar{p}} = 1.0 \cdot 10^{11}$, $\eta(s)$ as in top panel of Fig.22. The dotted lines represent the resonance lines $(n - Q_x)$ and $(n - Q_y)$ for $n = 8$, $n = 9$ and $n = 10$, yielding 0.4005, 1.4005 and 2.4005 for $(n - Q_x)$ and 0.3784, 1.3784 and 2.3784 for $(n - Q_y)$, respectively. The dashed lines represent the ring-averaged rms values $q_x^{rms} = 0.199$ and $q_y^{rms} = 0.283$. **Top**: $q_x$. **Bottom**: $q_y$.

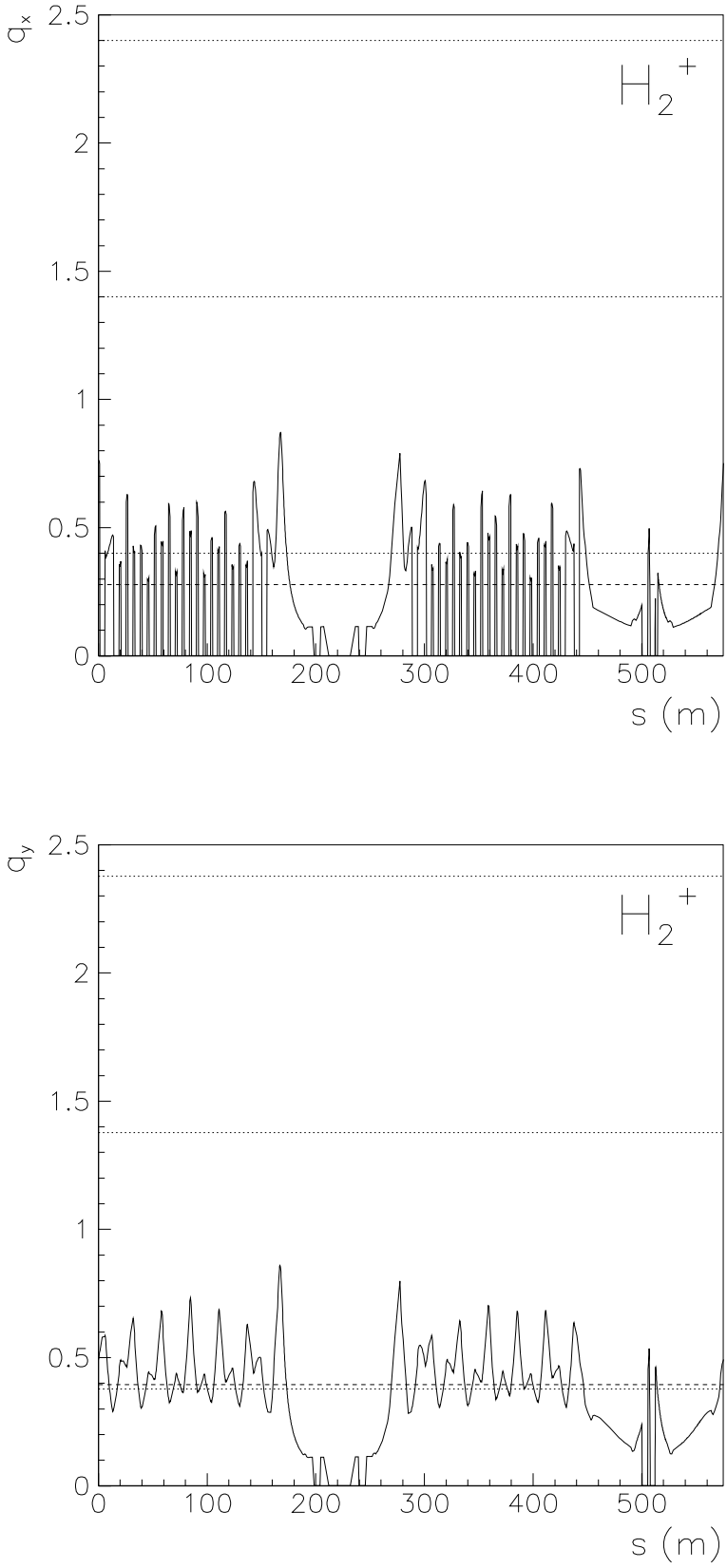


Fig. 32: Bounce frequencies of transverse $\mathbf{H_2^+}$ **ion oscillations** represented as 'tune numbers' $q_x = f_x/f_0$ and $q_y = f_y/f_0$, assuming $p_{\bar{p}}$ = **3.825 GeV/c**, $N_{\bar{p}} = 1.0 \cdot 10^{11}$, $\eta(s)$ as in top panel of Fig.22. The dotted lines represent the resonance lines $(n - Q_x)$ and $(n - Q_y)$ for $n = 8$, $n = 9$ and $n = 10$, yielding 0.4005, 1.4005 and 2.4005 for $(n - Q_x)$ and 0.3784, 1.3784 and 2.3784 for $(n - Q_y)$, respectively. The dashed lines represent the ring-averaged rms values $q_x^{rms} = 0.278$ and $q_y^{rms} = 0.395$. **Top**: $q_x$. **Bottom**: $q_y$.

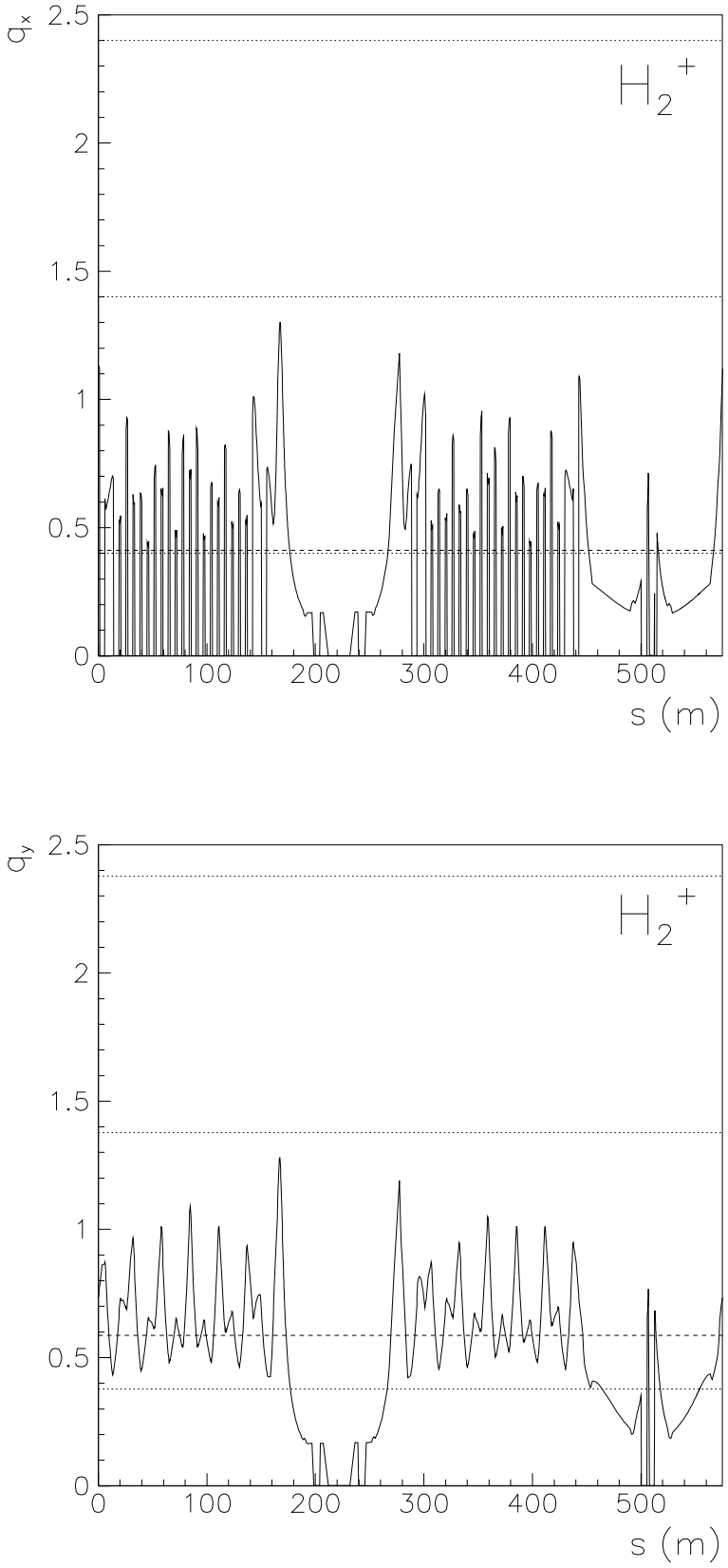


Fig. 33: Bounce frequencies of transverse $\mathbf{H}_2^+$ **ion oscillations** represented as 'tune numbers' $q_x = f_x/f_0$ and $q_y = f_y/f_0$, assuming $p_{\bar{p}}$ = **8.889 GeV/c**, $N_{\bar{p}} = 1.0 \cdot 10^{11}$, $\eta(s)$ as in top panel of Fig.22. The dotted lines represent the resonance lines $(n - Q_x)$ and $(n - Q_y)$ for $n = 8$, $n = 9$ and $n = 10$, yielding 0.4005, 1.4005 and 2.4005 for $(n - Q_x)$ and 0.3784, 1.3784 and 2.3784 for $(n - Q_y)$, respectively. The dashed lines represent the ring-averaged rms values $q_x^{rms} = 0.412$ and $q_y^{rms} = 0.586$. **Top**: $q_x$. **Bottom**: $q_y$.

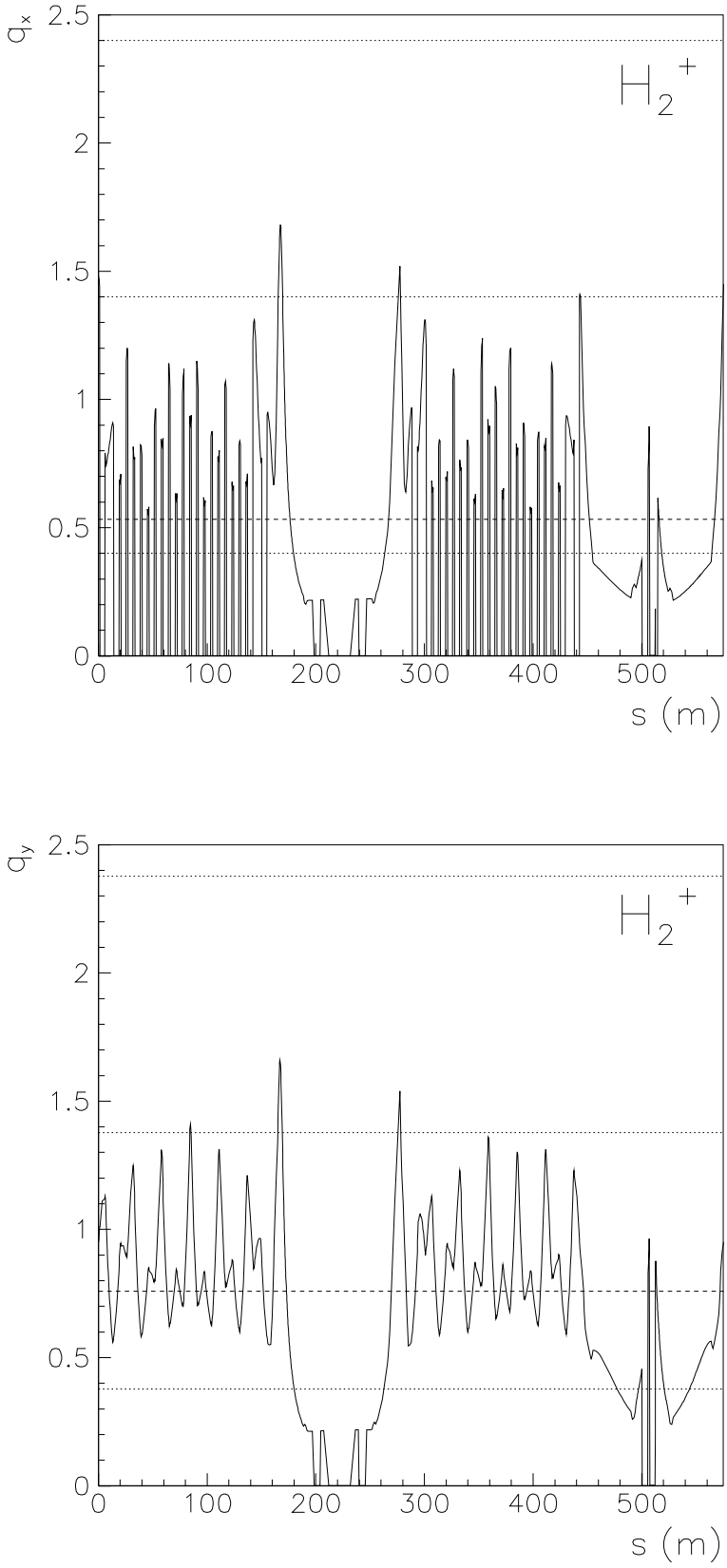


Fig. 34: Bounce frequencies of transverse $\mathbf{H}_2^+$ **ion oscillations** represented as 'tune numbers' $q_x = f_x/f_0$ and $q_y = f_y/f_0$, assuming $p_{\bar{p}} =$ **15.0 GeV/c**, $N_{\bar{p}} = 1.0 \cdot 10^{11}$, $\eta(s)$ as in top panel of Fig.22. The dotted lines represent the resonance lines $(n - Q_x)$ and $(n - Q_y)$ for $n = 8$, $n = 9$ and $n = 10$, yielding 0.4005, 1.4005 and 2.4005 for $(n - Q_x)$ and 0.3784, 1.3784 and 2.3784 for $(n - Q_y)$, respectively. The dashed lines represent the ring-averaged rms values $q_x^{rms} = 0.533$ and $q_y^{rms} = 0.759$. **Top**: $q_x$. **Bottom**: $q_y$.

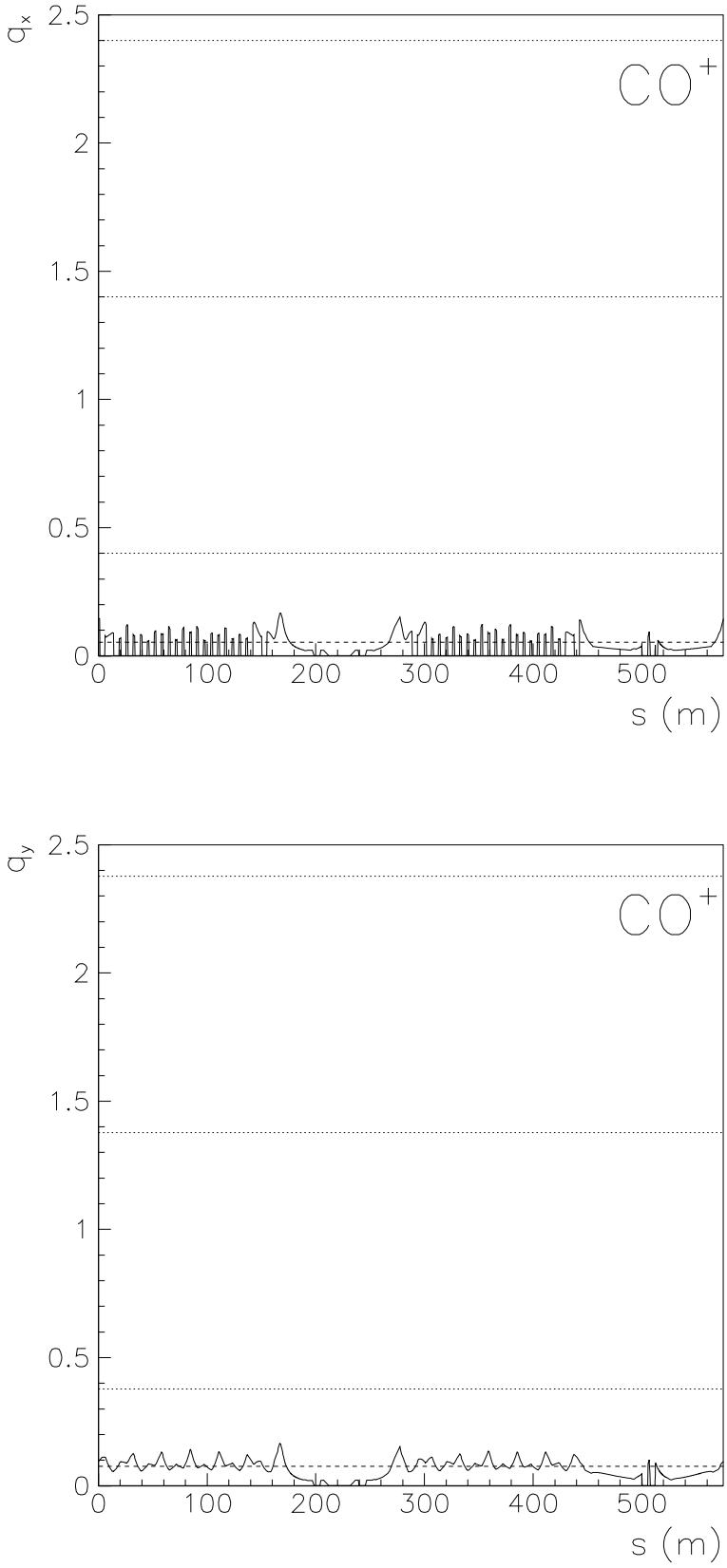


Fig. 35: Bounce frequencies of transverse **$CO^+$ ion oscillations** represented as 'tune numbers' $q_x = f_x/f_0$ and $q_y = f_y/f_0$, assuming $p_{\bar{p}}$ = **1.5 GeV/c**, $N_{\bar{p}} = 1.0 \cdot 10^{11}$, $\eta(s)$ as in top panel of Fig.22. The dotted lines represent the resonance lines $(n - Q_x)$ and $(n - Q_y)$ for $n = 8$, $n = 9$ and $n = 10$, yielding 0.4005, 1.4005 and 2.4005 for $(n - Q_x)$ and 0.3784, 1.3784 and 2.3784 for $(n - Q_y)$, respectively. The dashed lines represent the ring-averaged rms values $q_x^{rms} = 0.0533$ and $q_y^{rms} = 0.0758$. **Top**: $q_x$. **Bottom**: $q_y$.

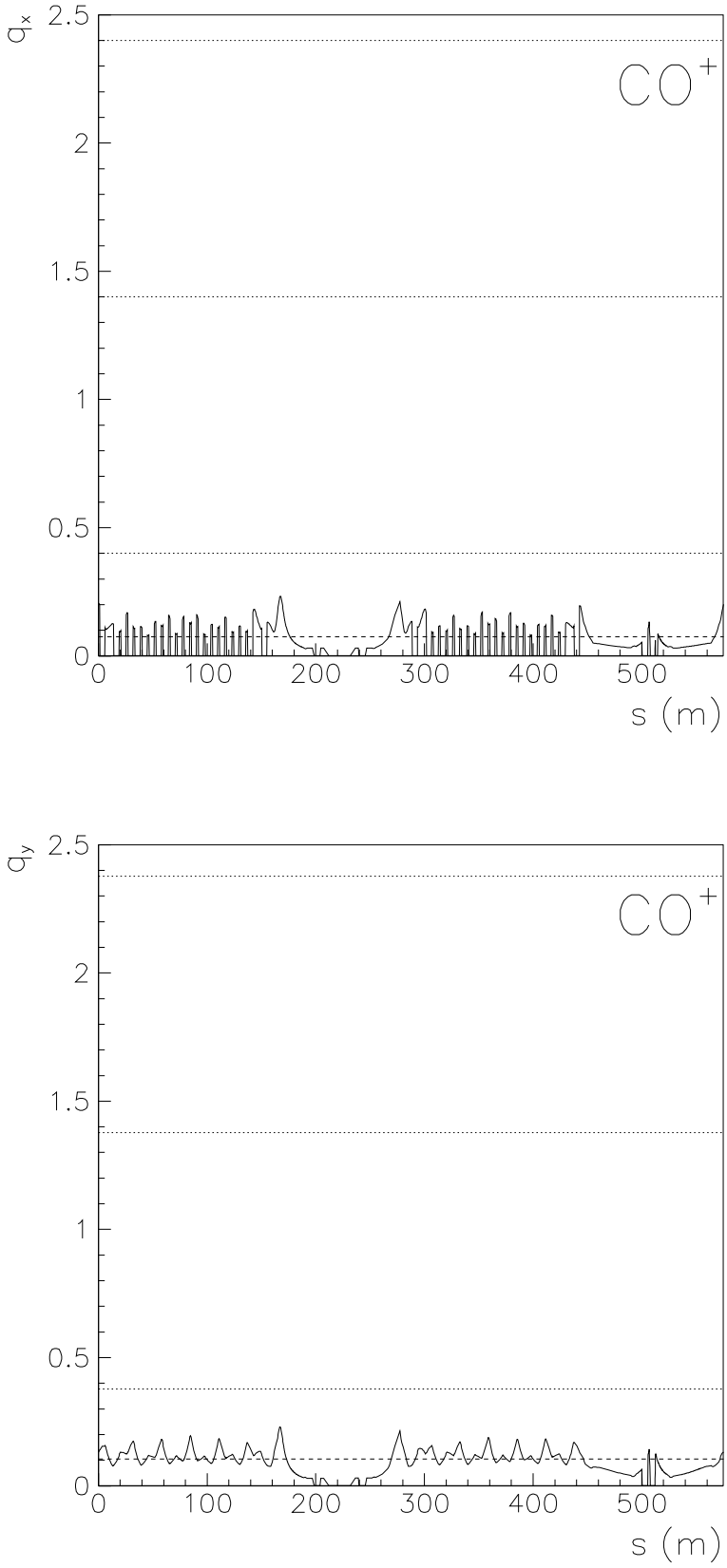


Fig. 36: Bounce frequencies of transverse **$CO^+$ ion oscillations** represented as 'tune numbers' $q_x = f_x/f_0$ and $q_y = f_y/f_0$, assuming $p_{\bar{p}}$ = **3.825 GeV/c**, $N_{\bar{p}} = 1.0 \cdot 10^{11}$, $\eta(s)$ as in top panel of Fig.22. The dotted lines represent the resonance lines $(n - Q_x)$ and $(n - Q_y)$ for $n = 8$, $n = 9$ and $n = 10$, yielding 0.4005, 1.4005 and 2.4005 for $(n - Q_x)$ and 0.3784, 1.3784 and 2.3784 for $(n - Q_y)$, respectively. The dashed lines represent the ring-averaged rms values $q_x^{rms} = 0.0742$ and $q_y^{rms} = 0.105$. **Top**: $q_x$. **Bottom**: $q_y$.

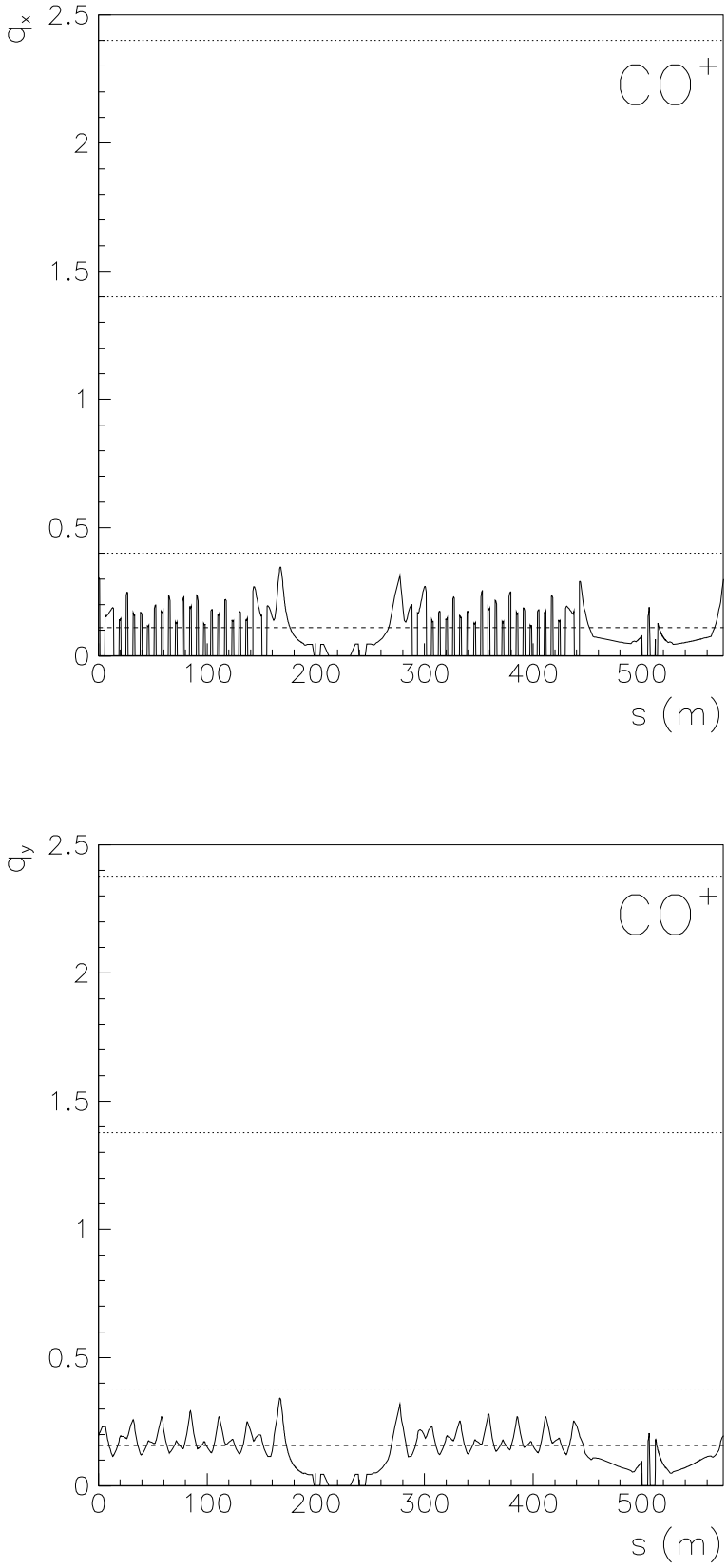


Fig. 37: Bounce frequencies of transverse **$CO^+$ ion oscillations** represented as 'tune numbers' $q_x = f_x/f_0$ and $q_y = f_y/f_0$, assuming $p_{\bar{p}}$ = **8.889 GeV/c**, $N_{\bar{p}} = 1.0 \cdot 10^{11}$, $\eta(s)$ as in top panel of Fig.22. The dotted lines represent the resonance lines $(n - Q_x)$ and $(n - Q_y)$ for $n = 8$, $n = 9$ and $n = 10$, yielding 0.4005, 1.4005 and 2.4005 for $(n - Q_x)$ and 0.3784, 1.3784 and 2.3784 for $(n - Q_y)$, respectively. The dashed lines represent the ring-averaged rms values $q_x^{rms} = 0.110$ and $q_y^{rms} = 0.157$. **Top**: $q_x$. **Bottom**: $q_y$.

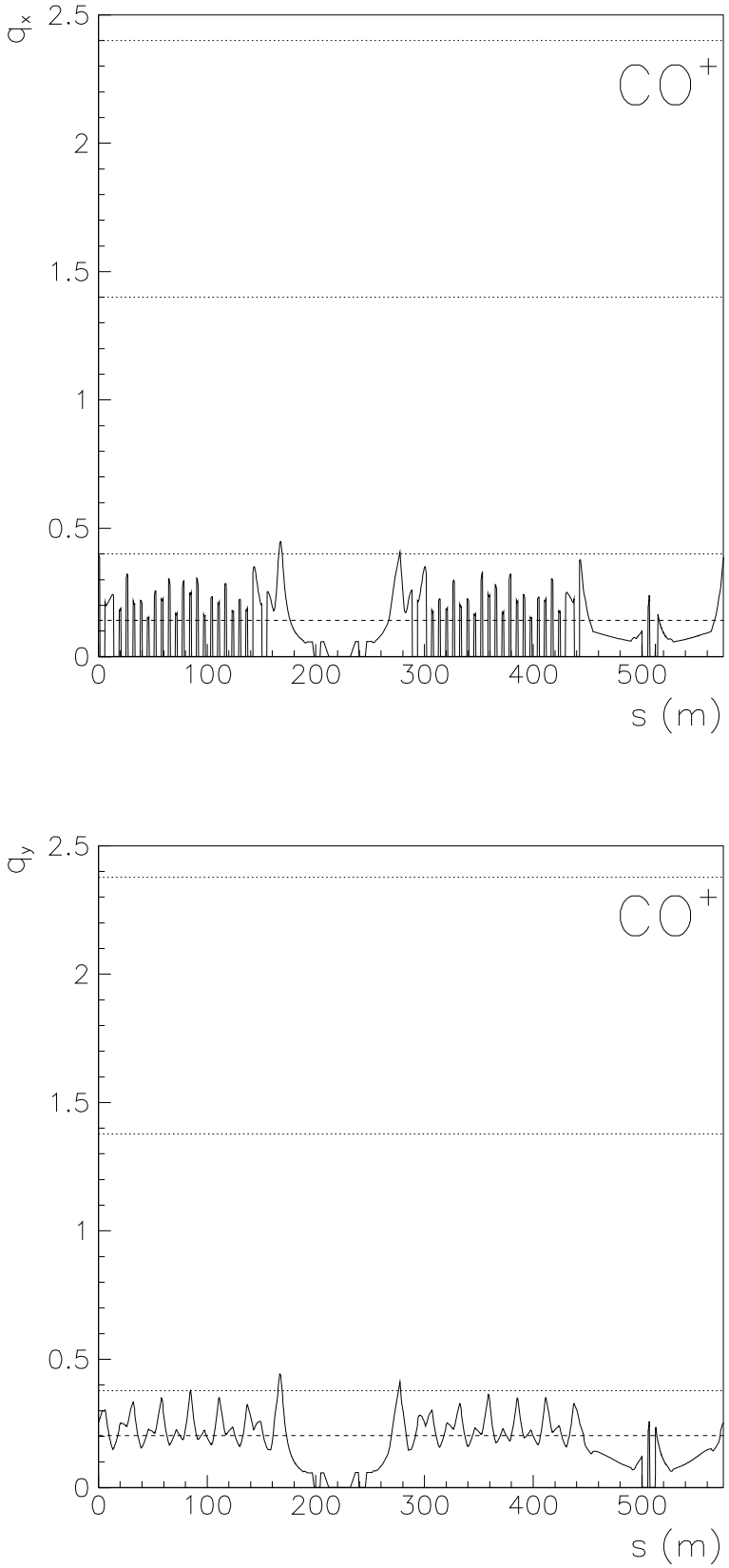


Fig. 38: Bounce frequencies of transverse **$CO^+$ ion oscillations** represented as 'tune numbers' $q_x = f_x/f_0$ and $q_y = f_y/f_0$, assuming $p_{\bar{p}}$ = **15.0 GeV/c**, $N_{\bar{p}} = 1.0 \cdot 10^{11}$, $\eta(s)$ as in top panel of Fig.22. The dotted lines represent the resonance lines $(n - Q_x)$ and $(n - Q_y)$ for $n = 8$, $n = 9$ and $n = 10$, yielding 0.4005, 1.4005 and 2.4005 for $(n - Q_x)$ and 0.3784, 1.3784 and 2.3784 for $(n - Q_y)$, respectively. The dashed lines represent the ring-averaged rms values $q_x^{rms} = 0.142$ and $q_y^{rms} = 0.203$. **Top**: $q_x$. **Bottom**: $q_y$.

### 18.2 Formalism of coherent instabilities

Because beam instabilities develop on a time scale much larger than the revolution period, the theoretical description of coupled oscillations can be simplified by introducing ring-averaged forces. Usually, the ring-averaged forces are calculated assuming a constant neutralization $\eta$ in the ring and using a smooth approximation for the envelopes, $\sigma_x = \sqrt{\epsilon_x \langle \beta_x \rangle}$ and $\sigma_y = \sqrt{\epsilon_y \langle \beta_y \rangle}$ with $\langle \beta_x \rangle = R/Q_x$ and $\langle \beta_y \rangle = R/Q_y$. However, in the HESR ring the neutralization $\eta$ depends strongly on the position $s$ due to the large pressure bump in the vicinity of the PANDA target. Also the envelopes depend strongly on the position $s$ due to the low beta values at the PANDA target and the large beta values in the region of the electron-cooler. Therefore, the HESR ring is segmented in small sections and the ring-averaged forces are numerically evaluated.

In the following we write the coupled equations for coherent oscillations in the $y$-direction and we omit the index $y$ for the characteristic forces $F_\beta$, $F_{sc}$, $F_c$, $F_{i,sc}$ and $F_{i,c}$ and the related quantities $Q_0^2$, $Q_{sc}^2$, $Q_c^2$, $q_{sc}^2$ and $q_c^2$. Similar equations can be written for the coupled oscillations in $x$-direction.

The model for coupled oscillations yields the following coupled equations for the motion of an individual antiproton ($y$) and ion ($y_i$),

$$\gamma m_{\bar{p}} \frac{\mathrm{d}^2 y}{\mathrm{d}t^2} = \langle F_\beta \rangle + \langle F_{sc} \rangle + \langle F_c \rangle, \tag{157}$$

$$m_i \frac{\mathrm{d}^2 y_i}{\mathrm{d}t^2} = \langle F_{i,sc} \rangle + \langle F_{i,c} \rangle. \tag{158}$$

Here, $\langle F_\beta \rangle$ represents the external focusing forces of the betatron oscillation, $\langle F_{sc} \rangle$ the $\bar{p}$ space-charge forces acting on the $\bar{p}$ beam particles, $\langle F_c \rangle$ the trapped ion space-charge forces acting on the $\bar{p}$ beam particles, $\langle F_{i,sc} \rangle$ the trapped ion space-charge forces acting on the ions and $\langle F_{i,c} \rangle$ the $\bar{p}$ space-charge forces acting on the ions. We note that space charge image forces are neglected. These equations are rewritten by introducing the tune number $Q_0$ of the unperturbed betatron oscillation and the 'tune numbers' $Q_{sc}$, $Q_c$, $q_{sc}$ and $q_c$. The ring averaged forces are represented by the corresponding 'tune numbers' times the angular frequency $\omega_0$ of the beam using the following definitions

$$\begin{aligned}
\frac{\langle F_\beta \rangle}{\gamma m_{\bar{p}}} &= Q_0^2 \omega_0^2 \, y, \\
\frac{\langle F_{sc} \rangle}{\gamma m_{\bar{p}}} &= Q_{sc}^2 \omega_0^2 \, (y - \bar{y}), \\
\frac{\langle F_c \rangle}{\gamma m_{\bar{p}}} &= Q_c^2 \omega_0^2 \, (y - \bar{y}_i), \\
\frac{\langle F_{i,sc} \rangle}{m_i} &= q_{sc}^2 \omega_0^2 \, (y_i - \bar{y}_i), \\
\frac{\langle F_{i,c} \rangle}{m_i} &= q_c^2 \omega_0^2 \, (y_i - \bar{y}).
\end{aligned} \tag{159}$$

Thus, the model for linearized coupled oscillations as described in [13] yields the following coupled equations for the dipole mode.

$$\frac{1}{\omega_0^2} \frac{\mathrm{d}^2 y}{\mathrm{d}t^2} + Q_0^2 \, y - Q_{sc}^2 (y - \bar{y}) + Q_c^2 (y - \bar{y}_i) = 0, \tag{160}$$

$$\frac{1}{\omega_0^2} \frac{\mathrm{d}^2 y_i}{\mathrm{d}t^2} - q_{sc}^2 (y_i - \bar{y}_i) + q_c^2 (y_i - \bar{y}) = 0. \tag{161}$$

The external focusing forces are represented by the squared tune $Q_0^2$ of the unperturbed betatron oscillation. The other forces are represented by the corresponding mean squared 'tune numbers',

$$Q_{sc}^2 = 2\frac{R^2}{L_1}\frac{N_{\bar{p}} r_p}{\beta^2\gamma^3}\left\langle \frac{1}{\sigma_y(s)(\sigma_x(s)+\sigma_y(s))}\right\rangle, \quad \bar{p}\text{ space charge acting on }\bar{p}, \tag{162}$$

$$Q_c^2 = 2\frac{R^2}{L_1}\frac{N_{\bar{p}} r_p}{\beta^2\gamma}\left\langle \frac{\eta(s)}{\sigma_y(s)(\sigma_x(s)+\sigma_y(s))}\right\rangle, \quad \text{ion space charge acting on }\bar{p}, \tag{163}$$

$$q_{sc}^2 = 2\frac{R^2}{L_1}\frac{N_{\bar{p}} r_p Z_i}{\beta^2 A_i}\left\langle \frac{\eta(s)}{\sigma_y(s)(\sigma_x(s)+\sigma_y(s))}\right\rangle, \quad \text{ion space charge acting on ion}, \tag{164}$$

$$q_c^2 = 2\frac{R^2}{L_1}\frac{N_{\bar{p}} r_p Z_i}{\beta^2 A_i}\left\langle \frac{1}{\sigma_y(s)(\sigma_x(s)+\sigma_y(s))}\right\rangle, \quad \bar{p}\text{ space charge acting on ion}. \tag{165}$$

Here, $Z_i$ is the charge number of the ion, $A_i$ the mass number and $r_p$ the classical proton radius. We assume that the neutralization $\eta(s)$ is dominated by singly charged $H_2^+$ ions. The coherent transverse motion of the ions is fixed in space and oscillates only in time. The coherent transverse motion of the $\bar{p}$ beam particles is oscillating in space and in time like a travelling wave. We are interested in resonant harmonics of coupled oscillations of the beam centers $\bar{y}$ and $\bar{y}_i$. To this end, we make the following ansatz,

$$\bar{y} = a\exp[i\,(k\,s-\omega\,t)] = a\exp[i\,(\frac{n}{R}\,s-\omega\,t)] \tag{166}$$

$$\bar{y}_i = a_i\exp\,[-i\omega t], \tag{167}$$

Here, the resonance condition imposes that the wave number $k$ and the wave length $\lambda$ of the travelling wave satisfy the resonance condition

$$k=\frac{n}{R}, \qquad \lambda=\frac{C}{n}. \tag{168}$$

where $n$ is an integer, $C$ the circumference and $R=C/(2\pi)$ the effective 'radius' of the machine. The substitution of $\bar{y}$ and $\bar{y}_i$ from (166) and (167) into (160) and (161) gives two equations,

$$\frac{1}{\omega_0^2}\frac{\mathrm{d}^2\bar{y}}{\mathrm{d}t^2} + (Q_0^2+Q_c^2)\,\bar{y} = Q_c^2\,\bar{y}_i, \tag{169}$$

$$\frac{1}{\omega_0^2}\frac{\mathrm{d}^2\bar{y}_i}{\mathrm{d}t^2} + q_c^2\,\bar{y}_i = q_c^2\,\bar{y}. \tag{170}$$

Since the $\bar{p}$ oscillations are oscillating in space ($s$) and time ($t$) (travelling wave ansatz, see Eq. (166)) the total differential $\mathrm{d}/\mathrm{d}t$ in the $\bar{p}$ equation of motion (160) must be written

$$\frac{\mathrm{d}}{\mathrm{d}t}=\left(\frac{\partial}{\partial t}+\frac{\partial}{\partial s}\dot{s}\right). \tag{171}$$

Inserting the travelling wave ansatz (166) yields

$$\frac{\mathrm{d}\bar{y}}{\mathrm{d}t} = \left(-i\omega+i\frac{n}{R}\dot{s}\right)\bar{y} = i(-\omega+n\omega_0)\bar{y},$$

$$\frac{\mathrm{d}^2\bar{y}}{\mathrm{d}t^2} = -(n\omega_0-\omega)^2\bar{y}. \tag{172}$$

Similarly, we get

$$\frac{\mathrm{d}^2\bar{y}_i}{\mathrm{d}t^2} = -\omega^2\bar{y}_i. \tag{173}$$

Using these relations in (169) and (170) yields

$$\left[-\frac{(n\omega_0-\omega)^2}{\omega_0^2} + (Q_0^2+Q_c^2)\right]\bar{y} = Q_c^2\bar{y}_i, \tag{174}$$

$$\left[-\frac{\omega^2}{\omega_0^2} + q_c^2\right]\bar{y}_i = q_c^2\bar{y}. \tag{175}$$

Eliminating $\bar{y}$ and $\bar{y}_i$ yields an equation for the angular frequency $\omega$ of the coherent oscillation. Introducing the reduced frequency $w = \omega/\omega_0$ the resulting equation may be written

$$(q_c^2 - w^2)[(Q_0^2+Q_c^2) - (n-w)^2] - q_c^2Q_c^2 = 0. \tag{176}$$

In this equation, $n$, $q_c$, $Q_c$ and $Q_0$ are the parameters and $w$ is the unknown. Stable solutions occur if $w$ becomes real, i.e. if $\omega$ becomes real. If $w$ is complex the solutions come in pairs, one with a negative imaginary part corresponding to a damping of the oscillations and one with a positive imaginary part corresponding to a growing (anti-damping) of the oscillations which means instability!

Since $Q_c \ll Q_0$, we can ignore it in the sum $(Q_0^2+Q_c^2)$ or slightly shift the value of $Q_0$ by introducing $Q^2 = (Q_0^2+Q_c^2)$. Unstable values (complex $w$) can occur if $q_c$ is close to a sideband frequency $(n-Q)$, i.e. $q_c \cong (n-Q)$ and $w \cong (n-Q)$. Replacing $w$ by $w = (n-Q)+\delta$ yields an equation quadratic in $\delta$,

$$\delta^2 + [(n-Q)-q_c]\delta + \frac{q_c^2Q_c^2}{4q_cQ} \cong 0. \tag{177}$$

The solution reads

$$\delta = -\frac{(n-Q)-q_c}{2} \pm \sqrt{\left(\frac{(n-Q)-q_c}{2}\right)^2 - \frac{q_c^2Q_c^2}{4q_cQ}}. \tag{178}$$

Thus, the equation yields complex solutions if

$$|(n-Q)-q_c| < \frac{q_cQ_c}{\sqrt{q_cQ}}. \tag{179}$$

This equation defines a band $\delta Q$ for $q_c$ in the vicinity of $(n-Q)$,

$$\delta Q = \frac{q_cQ_c}{\sqrt{q_cQ}}, \tag{180}$$

where instability can occur, i.e. where the solution $\omega = Re(\omega) + iIm(\omega)$ has a positive imaginary part.

The fastest growth rate occurs in the center of the band where $|(n-Q)-q_c| = 0$. There, we get $Re(\omega) = (n-Q)\omega_0$ and $Im(\omega) = (\omega_0/2)(q_cQ_c)/\sqrt{q_cQ}$. Thus. the fastest growth rate reads

$$\frac{1}{\tau} = \frac{\omega_0}{2}\frac{q_cQ_c}{\sqrt{q_cQ}}. \tag{181}$$

### 18.3 Landau damping of coherent instabilities

The coherent instability can be suppressed by Landau damping. We denote the $\bar{p}$ tune spread by $\Delta_{\bar{p}}$ and the ion oscillation tune spread $\Delta_i$. Landau damping works if the following three conditions are fulfilled simultaneously,

$$\Delta_{\bar{p}} > \left|\frac{Q_{sc}^2}{Q}\right|, \tag{182}$$

$$\Delta_i > \left|\frac{q_{sc}^2}{q}\right|, \tag{183}$$

$$\Delta_{\bar{p}}\Delta_i > \left|\frac{q_c^2 Q_c^2}{qQ}\right|. \tag{184}$$

Here, the space charge effects are taken into account in the definition of the betatron tune $Q$ and the ion bounce frequency $q$, $Q^2 = Q_0^2 + Q_c^2 - Q_{sc}^2$ and $q^2 = q_c^2 - q_{sc}^2$. We emphasize that the suppression of the two-beam instability requires that the product of the two tune spreads is larger than the right side of Eq. (184).

Including also the possibility of quadrupole modes, it is found that the risk of transverse instabilities exists in a band around the resonance line $(n - Q)$ given by

$$\delta Q = p\frac{q_c Q_c}{\sqrt{q_c Q}}, \tag{185}$$

where $p = 1$ for a dipole mode, $p = 1/2$ for a symmetric ($\zeta = \xi$) quadrupole mode and $p = 1/4$ for an antisymmetric ($\zeta = -\xi$) quadrupole mode. The width of this band reflects the risk of instability. It is proportional to $Q_c$, i.e. to the square root of the averaged neutralization $\sqrt{\langle\eta/[\sigma_y(\sigma_x + \sigma_y)]\rangle}$ (see Eq. (163)). It is narrower for quadrupole modes than for dipole modes. Including the possibility of quadrupole modes, the necessary condition for Landau damping reads

$$\Delta_{\bar{p}} > p\left|\frac{Q_{sc}^2}{Q}\right|, \tag{186}$$

$$\Delta_i > p\left|\frac{q_{sc}^2}{q}\right|, \tag{187}$$

$$\Delta_{\bar{p}}\Delta_i > p^2\left|\frac{q_c^2 Q_c^2}{qQ}\right|. \tag{188}$$

### 18.4 Numerical results

The HESR tune is $Q \cong 7.6$ ($Q_x = 7.5995$ and $Q_y = 7.6216$). For $n = 8$ we get the smallest value of $(n - Q_x)$ as 0.4005 which defines the 'tune number' $q_{c,x}$ where instability can occur. For $n = 9$, $n = 10$, etc. we get $(n - Q_x)$ as 1.4005, 2.4005, etc.. Similarly, for $n = 8$ we get the smallest value of $(n - Q_y)$ as 0.3784 which defines the 'tune number' $q_{c,y}$ where instability can occur. For $n = 9$, $n = 10$, etc. we get $(n - Q_y)$ as 1.3784, 2.3784, etc..

The occurrence of coherent oscillations depends critically on the neutralization of the beam by trapped ions. The coupling between beam and ions is determined by $Q_c^2$ which depends on the neutralization $\eta$ (see Eq. (163)). In the following we calculate the characteristic quantities taking the assumptions on $\eta(s)$ as in the top panel of Fig. 22, see Sect. 13.. The characteristic

quantities i.e. the ring-averaged 'tune numbers' $q = \sqrt{q_c^2 - q_{sc}^2}$ and $Q_c$ of ion and $\bar{p}$ bounce frequencies, the bandwidth $\delta Q$ and the difference $\Delta = |(8 - Q) - q_c| - \delta Q$ are listed in Tables 22-25 for $H^+$ and $H_2^+$ ions and four beam momenta. The danger of an unstable coherent oscillation is given in regions where $q_c$ is near a resonance line $(8 - Q)$. Then, the difference $|(8 - Q) - q_c|$ can be very small. The risk of instability is given if $q_c$ lies within the resonance band $(8 - Q) \pm \delta Q$, i.e. if $\Delta = |(8 - Q) - q_c| - \delta Q$ is negative. This occurs in our example for $q_x$ and $H^+$ ions near 3.825 GeV/c and for $q_x$ and $H_2^+$ ions near 8.889 GeV/c.

Table 22: Ring-averaged 'tune numbers' $q = \sqrt{q_c^2 - q_{sc}^2}$ and $Q_c$ of ion and $\bar{p}$ bounce frequencies, the bandwidth $\delta Q$ and the difference $\Delta = |(8 - Q) - q_c| - \delta Q$ for **coherent $H^+$ oscillations in $x$-direction** assuming $N_{\bar{p}} = 1.0 \cdot 10^{11}$, $\eta(s)$ as in top panel of Fig. 22, a beam-free gap of 10 % and the standard optics.

| $p$ (GeV/c) | $q_x$ | $Q_{c,x}$ | $\delta Q_x$ | $\Delta_x$ |
|---|---|---|---|---|
| 1.50 | 0.282 | 0.0662 | 0.0128 | 0.106 |
| 3.82 | 0.393 | 0.0618 | 0.0141 | -0.00615 |
| 8.89 | 0.582 | 0.0614 | 0.0170 | 0.165 |
| 15.0 | 0.754 | 0.0616 | 0.0194 | 0.334 |

Table 23: Ring-averaged 'tune numbers' $q = \sqrt{q_c^2 - q_{sc}^2}$ and $Q_c$ of ion and $\bar{p}$ bounce frequencies, the bandwidth $\delta Q$ and the difference $\Delta = |(8 - Q) - q_i| - \delta Q$ for **coherent $H^+$ oscillations in $y$-direction** assuming $N_{\bar{p}} = 1.0 \cdot 10^{11}$, $\eta(s)$ as in top panel of Fig. 22, a beam-free gap of 10 % and the standard optics.

| $p$ (GeV/c) | $q_y$ | $Q_{c,y}$ | $\delta Q_y$ | $\Delta_y$ |
|---|---|---|---|---|
| 1.50 | 0.401 | 0.0722 | 0.0166 | 0.00597 |
| 3.82 | 0.558 | 0.0674 | 0.0182 | 0.162 |
| 8.89 | 0.829 | 0.0669 | 0.0221 | 0.428 |
| 15.0 | 1.07 | 0.0671 | 0.0252 | 0.669 |

Table 24: Ring-averaged 'tune numbers' $q = \sqrt{q_c^2 - q_{sc}^2}$ and $Q_c$ of ion and $\bar{p}$ bounce frequencies, the bandwidth $\delta Q$ and the difference $\Delta = |(8 - Q) - q_c| - \delta Q$ for **coherent $\mathbf{H_2^+}$ oscillations in $x$-direction** assuming $N_{\bar{p}} = 1.0 \cdot 10^{11}$, $\eta(s)$ as in top panel of Fig. 22, a beam-free gap of 10 % and the standard optics.

| $p$ (GeV/c) | $q_x$ | $Q_{c,x}$ | $\delta Q_x$ | $\Delta_x$ |
|---|---|---|---|---|
| 1.50 | 0.199 | 0.0662 | 0.0107 | 0.190 |
| 3.82 | 0.278 | 0.0618 | 0.0118 | 0.111 |
| 8.89 | 0.412 | 0.0614 | 0.0143 | -0.00299 |
| 15.0 | 0.533 | 0.0616 | 0.0163 | 0.116 |

Table 25: Ring-averaged 'tune numbers' $q = \sqrt{q_c^2 - q_{sc}^2}$ and $Q_c$ of ion and $\bar{p}$ bounce frequencies, the bandwidth $\delta Q$ and the difference $\Delta = |(8 - Q) - q_i| - \delta Q$ for **coherent $\mathbf{H_2^+}$ oscillations in $y$-direction** assuming $N_{\bar{p}} = 1.0 \cdot 10^{11}$, $\eta(s)$ as in top panel of Fig. 22, a beam-free gap of 10 % and the standard optics.

| $p$ (GeV/c) | $q_y$ | $Q_{c,y}$ | $\delta Q_y$ | $\Delta_y$ |
|---|---|---|---|---|
| 1.50 | 0.283 | 0.0722 | 0.0139 | 0.0810 |
| 3.82 | 0.395 | 0.0674 | 0.0153 | 0.000933 |
| 8.89 | 0.586 | 0.0669 | 0.0186 | 0.189 |
| 15.0 | 0.759 | 0.0671 | 0.0212 | 0.359 |

### 18.5 Risk of coherent instabilities

The risk of instability depends on the beam neutralization $\eta$. This is due to fact that the coupling strength $Q_c^2$ and the resulting band width $\delta Q$ for unstable oscillations depend on the neutralization $\eta$. We mention that instabilities at low sideband frequencies are the most unstable modes because the frequency spreads are low. Thus, it is difficult to fulfill the conditions for the Landau damping of those instabilities [17]. Therefore, dipole instabilities driven by $H^+$ ions and $H_2^+$ ions occur already at very low neutralization levels ($\eta < 0.01$). It has been observed that the neutralization from a single trapped-ion pocket created by a localized vacuum chamber enlargement, may be sufficient to drive an instability [17, 36].

### 18.6 Damping of instabilities using feedback systems

Finally, we note that instabilities caused by ions can be effectively damped by transverse feedback systems using a highly sensitive resonant pick-up tuned at the frequency of the single unstable mode [16, 17]. At the cooler synchrotron COSY a broad band feedback system has been developed in order to damp transverse instabilities of electron cooled beams [37, 38]. The effect of the damping system can be measured by it's damping time $\tau$. An oscillation with an initial amplitude $A$ will be damped by the damper system as $A \exp(-t/\tau)$. As long as the damping time $\tau$ is less than the growing time of the instability, the beam can be stabilized [16].

## 19. Beam Shaking

The beam shaking can be used in order to decrease the neutralization $\eta$ and the coupling strength $Q_c^2$ for coherent oscillations in regions where the clearing electrodes cannot remove trapped ions sufficiently. The $\bar{p}$ beam is shaken using an RF electric field and the $\bar{p}$ beam shakes the ions. This method works if the shaking frequency is close to one of the sideband frequencies $(n-Q)\omega_0$ ('slow wave' frequency) or $(n+Q)\omega_0$ ('fast wave' frequency) and close to the ion bounce frequency $q_c\omega_0$. This condition corresponds to the resonance condition for coherent oscillations of beam and trapped ions as discussed in Sect. 18.2.

### 19.1 Formalism

We start with the coupled equations of motion (160) and (161) of beam and trapped ions in Sect. 18.2. We extend this equation by adding the force term of the shaking kicker $F\exp[-i\omega t]$,

$$\frac{1}{\omega_0^2}\frac{\mathrm{d}^2 y}{\mathrm{d}t^2} + Q_0^2\, y - Q_{sc}^2(y-\bar{y}) + Q_c^2(y-\bar{y}_i) = F\exp[-i\omega t]. \tag{189}$$

$$\frac{1}{\omega_0^2}\frac{\mathrm{d}^2 y_i}{\mathrm{d}t^2} - q_{sc}^2(y_i-\bar{y}_i) + q_c^2(y_i-\bar{y}) = 0. \tag{190}$$

The force term $F$ on the r.h.s of (189) represents the shaking kicker assumed to be a $\delta$ function in azimuth. The integrated electric field $E_0\Delta s\exp[-i\omega t]$ enters as

$$F\exp[-i\omega t] = \frac{eE_0\Delta s\exp[-i\omega t]}{m_{\bar{p}}\gamma\omega_0^2}\,\delta(s) = \frac{\Delta s}{C}\frac{eE_0}{m_{\bar{p}}\gamma\omega_0^2}\sum_{n=-\infty}^{n=+\infty}\exp[in\frac{s}{R}-i\omega t]. \tag{191}$$

Only the resonant harmonic with $\omega \approx (n\pm Q)\omega_0 \approx q_c\omega_0$ is retained yielding

$$F = \frac{\Delta s}{C}\frac{eE_0}{m_{\bar{p}}\gamma\omega_0^2}\exp[in\frac{s}{R}]. \tag{192}$$

We are interested in the resonant excitation of coupled oscillations of the beam centers $\bar{y}$ and $\bar{y}_i$. As in Sect. 18.2, we make the following ansatz for the coupled motion of the beam and ion centers,

$$\bar{y} = a\exp[i\,(k\,s-\omega\,t)] = a\exp[i\,(n\,\frac{s}{R}-\omega\,t)] \tag{193}$$

$$\bar{y}_i = a_i\exp[-i\omega t], \tag{194}$$

The substitution of $\bar{y}$ and $\bar{y}_i$ from (193) and (194) into (189) and (190) yields two equations,

$$[-(n\omega_0-\omega)^2 + (Q_0^2+Q_c^2)\omega_0^2]\,\bar{y} - Q_c^2\omega_0^2\bar{y}_i = \omega_0^2 F\exp[-i\omega t], \tag{195}$$

$$(-\omega^2+q_c^2\omega_0^2)\,\bar{y}_i - q_c^2\omega_0^2\bar{y} = 0. \tag{196}$$

Using these relations and defining $Q^2=(Q_0^2+Q_c^2)$, we get the equations of the forced oscillation of two coupled oscillators,

$$\bar{y} = \frac{-\omega^2+q_c^2\omega_0^2}{[-(n\omega_0-\omega)^2+Q^2\omega_0^2](-\omega^2+q_c^2\omega_0^2)-q_c^2Q_c^2\omega_0^4}\omega_0^2 F\exp[-i\omega t], \tag{197}$$

$$\bar{y}_i = \frac{q_c^2\omega_0^2}{[-(n\omega_0-\omega)^2+Q^2\omega_0^2](-\omega^2+q_c^2\omega_0^2)-q_c^2Q_c^2\omega_0^4}\omega_0^2 F\exp[-i\omega t]. \tag{198}$$

Introducing the reduced frequency $w = \omega/\omega_0$ these equations may be written

$$\bar{y} = -\frac{w^2 - q_c^2}{(w^2 - q_c^2)[(n-w)^2 - Q^2] - q_c^2 Q_c^2} F \exp[-i\omega t], \tag{199}$$

$$\bar{y}_i = \frac{q_c^2}{(w^2 - q_c^2)[(n-w)^2 - Q^2] - q_c^2 Q_c^2} F \exp[-i\omega t]. \tag{200}$$

It is interesting to note that the denominator in those equations is equal to the l.h.s. of the important equation (176). Shaking works if the amplitude of $\bar{y}_i$ becomes large, i.e. when the denominator approaches zero. Here, we must consider the non-linear detuning and the condition for the so-called 'lock-on' of the ions onto the resonance. With increasing amplitudes the bounce frequency $q_c$ of the ions decreases. Thus, $(w^2 - q_c^2)$ is positive and increases. As a consequence, in order to achieve a denominator approaching zero, $[(n-w)^2 - Q^2]$ must also be positive and the condition for $\bar{y}_i$ becoming large may be written

$$(w^2 - q_c^2) > 0, \tag{201}$$

$$(n-w)^2 - Q^2 > 0. \tag{202}$$

That means for the excitation near a slow wave sideband frequency with $\omega \approx (n-Q)\omega_0$ and positive $n$ with $n > Q$,

$$w < n - Q, \tag{203}$$

i.e. the excitation frequency $\omega$ must be slightly below the resonance frequency $(n-Q)\omega_0$. For the excitation near a fast wave sideband frequency with $\omega \approx (n+Q)\omega_0$ and negative $n$ with $n > -Q$,

$$w > n + Q, \tag{204}$$

i.e. the excitation frequency $\omega$ must be slightly above the resonance frequency $(n+Q)\omega_0$.
Finally, we note the relation between $\bar{y}$ and $\bar{y}_i$

$$\bar{y} = -\frac{\omega^2 - q_c^2\omega_0^2}{q_c^2\omega_0^2}\bar{y}_i = -\frac{w^2 - q_c^2}{q_c^2}\bar{y}_i. \tag{205}$$

Since $\omega \approx q_c\omega_0$, the amplitude of the beam oscillation is very small compared to the large amplitude of the ion oscillation.

### 19.2 Experimental observations

Here, we cite some important observations during shaking experiments at the CERN Antiproton Accelerator (CERN AA) which are reported by Alain Poncet [15].

The effects of neutralization have been considerably reduced by exciting vertical coherent oscillations with a transverse kicker in the CERN AA. The shaking system has been permanently implemented. It has the following parameters:
shaking: vertical
shaking frequency: 490 kHz
sideband frequency: 480 kHz
length of kicker electrodes: 0.6 m
kicker field: $\sim 20$ V/cm
The experimental observations can be summarized as follows:

1. Beam shaking works best when applied vertically. A possible reason is that neutralization is high in dipole fields due to the low ion drift velocity. In addition the ions can oscillate freely along the vertical magnetic field lines.
2. The beam shaking relies on the longitudinal motion of the ions. Due to changing beam dimensions, the ion 'bounce frequency' is not constant. But the frequency of the shaking kicker defines the positions in the ring where the bounce frequency is in resonance with the kicker frequency. Thus, ions must move longitudinally to the resonance positions. Therefore, beam shaking works best in conjunction with clearing electrodes which provide a low level of neutralization. Then, the ions can be accelerated by the longitudinal gradients of the beam potential towards the resonance positions.
3. Beam shaking depends on the non-linearity of the space-charge field. This allows the 'lock-on' of the sweeping ions onto the resonance. There, they keep large oscillation amplitudes and their density is reduced in the beam center.
4. Beam shaking is efficient even with low RF fields of only 10 V/cm, provided it is applied close to a beam betatron sideband whose frequency lies close to the ion bounce frequency. In this case, the beam resonant response yields sufficiently large non-linear forces on the ion. Experimentally, it is found that for a weakly exciting RF field, shaking works best above a band $(n + Q)$ or below a band $(n - Q)$. This observation of asymmetry of weak resonant shaking is important in that it validates the non-linear character of the ion motion and the 'lock-on' conditions.

### 19.3 Resonant transverse shaking of the HESR beam

The HESR ring is an energy variable machine yielding beam momenta between 1.5 and 15.0 GeV/c. Thus, the revolution frequencies $f_0 = \omega_0/(2\pi)$ are not constant but depend on the beam momentum. The betatron tunes amount to $Q_x = 7.5995$ and $Q_y = 7.6216$. In Table 26 we list the corresponding slow-wave sideband frequencies $(n - Q)f_0$ for $n = 8$ and the fast-wave sideband frequencies $(n + Q)f_0$ for $n = -7$.

Table 26: Slow- and fast-wave sideband frequencies.

| $p$ (GeV/c) | $f_0$ (kHz) | $(8 - Q_x)f_0$ (kHz) | $(8 - Q_y)f_0$ (kHz) | $(Q_x - 7)f_0$ (kHz) | $(Q_y - 7)f_0$ (kHz) |
|---|---|---|---|---|---|
| 1.500 | 441.9 | 177.0 | 167.2 | 264.9 | 274.7 |
| 3.825 | 506.2 | 202.7 | 191.5 | 303.5 | 314.7 |
| 8.889 | 518.3 | 207.6 | 196.1 | 310.7 | 322.2 |
| 15.00 | 520.2 | 208.3 | 196.8 | 311.9 | 323.4 |

If we assume $1.0 \cdot 10^{11}$ antiprotons in the HESR ring the 'tune numbers' $q_x$ and $q_y$ of $H^+$ and $H_2^+$ ions coincide at many places with one of the sideband tunes $(8 - Q_x) = 0.4005$, $(8 - Q_y) = 0.3784$, $(Q_x - 7) = 0.5995$ or $(Q_y - 7) = 0.6216$, see Figs. 27 - 34. The 'tune numbers' are proportional to $\sqrt{N_{\bar{p}}/[\sigma_{x,y}(\sigma_x + \sigma_y)]}$. For $N_{\bar{p}} = 1.0 \cdot 10^{10}$ all 'tune numbers' decrease by a factor $\sqrt{10^{1/5}} = 1.26$. Resonant transverse shaking is not all possible for heavier ions like $CO^+$ ions. Even for $N_{\bar{p}} = 1.0 \cdot 10^{11}$ the 'tune numbers' of $CO^+$ oscillations are below the sideband tunes.

The possible shaking frequencies are in the range of about 165-330 kHz. A broad-band kicker covering this frequency range with field strengths of about 20 V/cm would be sufficient for resonant transverse shaking of the most critical $H^+$- and $H_2^+$-ions.

Summarizing, we note that beam shaking alone is not sufficient to remove trapped ions. Clearing of trapped ions by shaking is only possible under certain conditions at discrete specific positions in the ring and for light ions like $H^+$ and $H_2^+$. Heavier ions cannot be removed by beam shaking. Therefore, clearing of trapped ions in the HESR ring should be mainly done with the aid of clearing electrodes.

Finally, we mention that beam shaking deteriorates the transverse beam quality. This fact must be taken into account when applying beam shaking in the HESR ring.

## 20. Beam-free Time Gap

In this section, we summarize the effects of the beam-free time gap with respect to the production and clearing of trapped ions. The barrier-bucket mode of operation produces a long bunch of antiprotons with $t_1 = 0.9\,T$ which is interrupted by a short beam-free time gap $t_2 = 0.1\,T$. Here, $T = 1/f$ is the revolution time of the antiproton beam. Taking 500 kHz as typical revolution frequency the beam-free time gap amounts to about 0.2 $\mu$s.

### 20.1 Extraction of trapped ions during the beam-free time gap

Taking only the mean thermal velocities into account (see Table 3), the trapped ions cannot escape the potential well of the antiproton beam during the short beam-free time gap. For instance the mean thermal velocity $\bar{v}_{\parallel}$ of $H_2^+$ ions amounts to 889 m/s yielding a mean distance of only 0.18 mm within 0.2 $\mu$s.

In principle it should be possible to extract trapped ions using high transverse electric fields during the beam-free time gaps. To this end high transverse electric fields could be switched on during the beam-free time gaps. A quick estimate shows that transverse electric fields of about 50 kV/m are needed in order to extract $H_2^+$ ions within a time period $t_2$ of about 0.2 $\mu$s. However the switch-on and switch-off time would be extremely short (about 0.01 $\mu$s). For heavier ions like for instance $CO^+$ ions the necessary transverse electric fields of 700 kV/m would be unrealistically high.

### 20.2 Instability of ion oscillations

Sect. 16. deals with the problem of instabilities of ion oscillations. Positive ions perform oscillations during the long time period $t_1$ in the negative potential well of the antiproton beam, see Sect. 18.1. During the short beam-free time gap $t_2$ the ions move freely in the direction of their momentary transverse velocity. But the ions cannot escape within 0.2 $\mu$s. The only possibility to escape is that the ion oscillation amplitudes increase steadily, i.e. that the ion oscillation becomes instable due to the beam-free time gap. Instabilities occur if the 'tune numbers' $q_{x,y}$ of the ion oscillations are located in certain specific intervals, for instance $0.50 < q_{x,y} < 0.55$. As shown in Sect. 16. the oscillations of $H_2^+$ ions become instable at a few localized positions in the ring if $1.0 \cdot 10^{11}$ antiprotons are circulating. Ions with larger mass like for instance $CO^+$ or $N_2^+$ ions perform always stable oscillations since the focusing strengths are nearly an order of magnitude lesser.

Summarizing, the trapped ions perform mostly stable oscillations in the negative potential well of the antiproton beam. The beam-free time gap causes instable oscillations of $H_2^+$ ions only at a few localized positions in the ring and only for $1.0 \cdot 10^{11}$ antiprotons in the ring. Heavier ions are not affected at all. Thus, the benefit of detrapping ions by instable ion oscillations is negligibly small.

## 21. Diagnostic Tools and Measurements of Trapped Ion Effects

### 21.1 Current measurements at clearing electrode

An important diagnostic tool is the measurement of the clearing currents at the clearing electrodes. To this end each clearing electrode should be equipped with a Pico-Amperemeter. All clearing electrodes should be computer controlled such that one can adjust individually the clearing voltages and measure the clearing currents down to picoamps. Then, the electrode clearing currents can be measured as a function of the electrode voltages in order to verify the required maximum voltage for full clearing. The clearing current will saturate if a sufficiently high voltage is reached.

Additional information about neutralization and trapped ion pockets can be obtained by individually switching on and off, and by reversing the applied voltage from negative to positive. The Pico-Amperemeter should be fast enough to allow the measurement of time dependent processes. For instance the longitudinal mobility of trapped ions can be studied by switching off the voltage in one channel of the clearing system and measuring the additional currents at the neighbouring electrodes.

### 21.2 Tune-shift measurements

The HESR Schottky diagnostics can be used in order to study the behavior of the antiproton beam. The signals from the transverse Schottky pickups allow precise tune-shift measurements. The incoherent tune shifts depend on the average neutralization $\eta$ of the beam, see Eqs. (148) and (150). Thus, by measuring the tunes $Q_x$ and $Q_y$ with and without ion clearing one can deduce the average neutralization $\eta$. Similarly, one can study the effectiveness of the clearing electrodes by measuring the residual neutralization as a function of the clearing voltages.

### 21.3 Beam emittance measurements

The power in the bands of the transverse Schottky spectrum can be used in order to deduce information on the beam emittance. Thus, one can study the influence of trapped ion effects on the beam emittance by switching the clearing voltages on and off.

### 21.4 Measurement of the coherent ion-beam oscillations

Pockets of trapped ions can interact resonantly with the beam. As a result coherent oscillations with large amplitudes can occur. Therefore it is necessary to measure the dipole spectrum of the beam at the sideband frequencies $(8 - Q_{x,y})$ and $(9 - Q_{x,y})$. By decreasing the clearing voltage one can study the growth of the dipole modes which is an indication of trapped ion effects.

### 21.5 Measurements of the transverse beam transfer function

The transverse beam transfer function is obtained by exciting the beam with a periodic signal and measuring the response (amplitude and phase) as a function of the frequency. Measurements at the the Fermilab Antiproton Accumulator [39] showed a double peak structure of the amplitude response at the beam dipole resonance frequency $(2 - q)f_0$ ($q$ is here the fractional part of the betatron tune) due to the presence of trapped ions. The double peak structure seems to be caused by the non-linearity of the ion motion in the antiproton beam.

## 22. Summary and Conclusion

The phenomenon of ion trapping in the future HESR antiproton storage ring is studied in the present report. Outside of the PANDA target region the UHV vacuum pressure amounts to about $1.0 \cdot 10^{-9}$ mbar yielding full neutralization of the negative beam potential within about 7 s. Near the PANDA target the pressure rises up to about $6.0 \cdot 10^{-5}$ mbar yielding full neutralization within about 0.1 ms. The positive ions (mainly $H_2^+$ ions) are trapped by the negative beam potential and perform quasi-harmonic oscillations in the potential well. The central beam potential is calculated assuming the standard optics of the HESR ring. The local minima of the potential are especially dangerous since they act as trapped ion pockets.

The positive ions can be extracted out of the beam using clearing electrodes with sufficiently high electric fields. We recommend to install as many electrodes as possible at least one electrode every 5 m in the two long straight sections. In the arcs clearing electrodes should be located in the 2 m long straight sections at the entrance and exit of the dipole magnets.

The danger of a high neutralization in the region of dipole magnets has been discussed in Subsect. 10.4. Ion clearing by mean cross-field drift velocities is not sufficient if the residual gas pressure amounts to about $1.0 \cdot 10^{-9}$ mbar. In order to solve this problem three different suggestions are discussed: (i) Continuous vertical clearing electrodes inside the beam pipes in order to extract the trapped ions along the magnetic field lines in the vertical direction (see Subsect. 10.5). (ii) Continuous horizontal clearing electrodes inside the beam pipes in order to achieve sufficient cross-field drift velocities in the longitudinal direction (see Subsect. 10.6). (iii) Improvement of the UHV vacuum by about a factor of hundred (see Subsect. 10.7). In view of the difficulty to install continuous clearing electrodes inside of the 4.2 m long beam pipes of a dipole magnet, the optimum solution is to improve the UHV vacuum to a level of about $1.0 \cdot 10^{-11}$ mbar.

In solenoids the ions move freely along the longitudinal direction. Clearing electrodes should be located at the entrance and exit of the solenoids. The problem of trapped ions in the intense electron beam of the electron cooler has been separately discussed in Sect. 14..

A virulent problem represents the huge pressure bump in the neighbourhood of the PANDA target. The ion production rate is so high that without sufficient clearing the antiproton beam can be fully neutralized within 0.1 ms - 10 ms. In addition the produced ions cannot escape in the transverse direction due to the high magnetic field of the solenoid. The special problems of the target region and possible solutions are discussed in Sect. 15..

The effect of the beam-free time gap with respect to ion clearing has been studied in detail. The barrier bucket mode of operation produces a long bunch of length $L_1 = 0.9\,C$ followed by a short beam-free gap of length $L_2 = 0.1\,C$ with $L_1 + L_2 = C$. It has been shown that the positive ions perform mostly stable oscillations in the negative potential well. The stability condition is practically not affected by the short beam-free gap of length $L_2$ which acts ion-optically like a drift space. Instabilities with $TrM_{x,y} > 2$ occur only under certain conditions at a few discrete positions in the HESR ring.

Trapped ions in the beam represent an additional target for secondary reactions with the antiproton beam. However the estimate of the resulting luminosities shows that the secondary reaction rates are negligibly small compared to the primary reaction rates due to the residual gas molecules.

The adverse effects of the trapped ions are due to the additional electric field of the trapped ion clouds. First of all the trapped ions affect the betatron oscillations of the beam yielding

incoherent tune shifts and tune spreads. The tune shifts and spreads have been estimated by taking the beam envelopes around the ring into account and by numerically integrating the corresponding expressions. Simple order of magnitude checks confirm the numerical results. The ion induced tune shifts are about $1.3 \cdot 10^{-4}$ if the mean neutralization is kept at the 3 % level.

The most dangerous effects of trapped ions are coherent instabilities due to the interaction of the antiproton beam with the trapped ions. Numerical calculations of the ion bounce frequencies show that coherent oscillations can be excited by $H^+$ and $H_2^+$ ions at the sideband frequencies $(8 - Q_{x,y})$. The risk of instability depends on the neutralization $\eta$, i.e. on the coupling strength of the ion space charge acting on the $\bar{p}$ beam. Dangerous oscillations can be avoided by keeping the neutralization below $10^{-3}$. Heavier ions like $N_2^+$ and $CO^+$ cannot cause dangerous oscillations. They exhibit bounce frequencies which are below the critical resonance frequencies $(8 - Q_{x,y})$. Coherent instabilities can be suppressed by Landau damping. If necessary, the coherent instabilities can also be damped by transverse feedback systems using highly sensitive resonant pick-up systems tuned at the frequency of the unstable mode.

The possibility of removing trapped ions by beam shaking has also been studied. The $\bar{p}$ beam can be shaken using a broad-band kicker with field strengths of about 20 V/cm. The trapped ions are shaken by the forced oscillation of the $\bar{p}$ beam. The amplitudes of the ion oscillations become very large compared to the small amplitudes of the $\bar{p}$ beam. Thus, the ions are removed by neutralization at the beam pipe. The possible shaking frequencies are in the range of 165-330 kHz. Resonant transverse shaking is possible if the ion bounce frequencies are slightly below the slow-wave sideband frequencies $(8 - Q_{x,y})$ and/or slightly above the fast-wave sideband frequency $(Q_{x,y} - 7)$. Resonant transverse shaking can only be used under certain conditions ($N_{\bar{p}} > 1.0 \cdot 10^{10}$) in order to remove light ions like $H^+$ and $H_2^+$ at discrete positions in the ring. Heavier ions cannot be removed by beam shaking. Therefore, clearing of trapped ions in the HESR should be mainly done using clearing electrodes.

Finally, diagnostic tools and measurements of trapped ion effects are discussed. The current measurements at clearing electrodes are very important. They provide information about neutralization and trapped ion pockets. In addition they help to optimize the clearing voltages. The average neutralization $\bar{\eta}$ of the beam can be measured using tune shift measurements. Measurements of the beam emittances and the coherent ion-beam oscillations give additional information about trapped ion effects.

## 23. Appendix

### 23.1 Magnetron motion and modified cyclotron motion of trapped ions in solenoids

Here, we discuss first the magnetron motion and the modified cyclotron motion of trapped ions in solenoids which is due to the superposition of a radial electric field $\vec{E}$ and a longitudinal magnetic field $\vec{B}$. The magnetron motion and the modified cyclotron motion has been first studied during the invention of the magnetron [28]. These motions have also been analyzed during the development of Penning traps [29]. As to the equations of motion for a Penning trap, we refer to review articles by Brown and Gabrielse [30] and Blaum [31].

The beam envelopes of the antiproton beam are nearly axial symmetric in the region of the solenoids. The resulting radial acceleration by the electric field $\vec{E}$ of the antiproton beam is directed radially towards the central axis. This is in contrast to magnetrons and Penning traps where the radial acceleration is directed off the central axis. This important difference must be taken into account in the solution of the equations of motion.

We use the Cartesian coordinate system $(x, y, z)$ which coincides with the standard coordinate system of accelerator physics $(x, y, s)$. The $z$-axis is oriented along the central axis of the solenoid. We describe the ion motion radially by $\vec{\rho} = (x, y)$ and axially by $z$. The equations of motions read

$$m\ddot{\vec{\rho}} = q(\vec{E}_\rho + \dot{\vec{\rho}} \times \vec{B}), \tag{206}$$

$$m\ddot{z} = qE_z. \tag{207}$$

We first discuss the solution of the radial equation. We assume a linear approximation of an axial symmetric electric field directed towards the central axis,

$$\vec{E_\rho} = -E_0\vec{\rho}. \tag{208}$$

Without loss of generality, we assume a magnetic field $\vec{B}$ oriented in the negative $z$-direction,

$$\vec{B} = -(0, 0, B). \tag{209}$$

Thus, the resulting angular velocity $\vec{\omega}_c$ of the cyclotron motion is directed in the positive $z$-direction. We remember that the angular frequency $\omega_c$ of the free cyclotron motion (i.e. for $\vec{E_\rho} = 0$) is given by

$$\omega_c = \frac{qB}{m}. \tag{210}$$

We introduce the parameter $\omega_b$ in order to take the electric field strength in the following equations into account,

$$\omega_b = \sqrt{\frac{qE_0}{m}}. \tag{211}$$

The parameter $\omega_b$ represents the angular frequency of trapped ion oscillations in the potential well of the antiproton beam for $B = 0$. The radial equation of motion can be solved using the following ansatz

$$\vec{\rho} = \vec{r}_+ + \vec{r}_-, \tag{212}$$

$$\vec{r}_+ = r_+(\cos(\omega_+ t + \alpha_+), \sin(\omega_+ t + \alpha_+)), \tag{213}$$

$$\vec{r}_- = r_-(\cos(\omega_- t + \alpha_-), \sin(\omega_- t + \alpha_-)). \tag{214}$$

Thus, the radial motion of an ion is characterized by two independent motional modes: (i) the modified cyclotron motion with angular frequency $\omega_+$ and radius $r_+$ and (ii) the magnetron motion with angular frequency $\omega_-$ and radius $r_-$. Inserting the ansatz (212) into (206) yields

$$\omega_+ = \frac{\omega_c}{2} + \sqrt{\left(\frac{\omega_c}{2}\right)^2 + \omega_b^2}, , \tag{215}$$

$$\omega_- = \frac{\omega_c}{2} - \sqrt{\left(\frac{\omega_c}{2}\right)^2 + \omega_b^2}. \tag{216}$$

The magnetron motion has not the same direction of rotation as the modified cyclotron motion, i.e. the angular velocity $\vec{\omega}_+$ is directed in the positive $z$-direction whereas the angular velocity $\vec{\omega}_-$ is directed in the negative $z$-direction. This is due to the radially attractive electric potential, see Fig. 12. In this context, we note that $\omega_-$ in Eqs. (214) and (216) is a negative quantity. However, the absolute value of the angular velocity reads

$$|\vec{\omega}_-| = |\omega_-| = -\frac{\omega_c}{2} + \sqrt{\left(\frac{\omega_c}{2}\right)^2 + \omega_b^2}. \tag{217}$$

This fact is important if one tries to find the solution of the equations of motion. The parameters $r_+$, $r_-$, $\alpha_+$ and $\alpha_-$ are constants of integration determined by the initial position and velocity of the ion in the moment of ionization.

### 23.2 Proof

Now, we sketch the proof that the ansatz (212)-(214) with Eqs. (215) and (216) for $\omega_+$ and $\omega_-$ is a solution of the radial equation of motion. We insert $\vec{\rho} = \vec{r}_+ + \vec{r}_-$ into the equation of motion (206),

$$m(\ddot{\vec{r}}_+ + \ddot{\vec{r}}_-) = q(\dot{\vec{r}}_+ + \dot{\vec{r}}_-) \times \vec{B} - qE_0(\vec{r}_+ + \vec{r}_-). \tag{218}$$

Taking into account that

$$\ddot{\vec{r}}_\pm = -\omega_\pm^2 \vec{r}_\pm \tag{219}$$

and

$$\dot{\vec{r}}_\pm = \vec{\omega}_\pm \times \vec{r}_\pm \tag{220}$$

we get

$$-(\omega_+^2 \vec{r}_+ + \omega_-^2 \vec{r}_-) = \frac{q}{m}(\vec{\omega}_+ \times \vec{r}_+ + \vec{\omega}_- \times \vec{r}_-) \times \vec{B} - \frac{q}{m} E_0(\vec{r}_+ + \vec{r}_-), \tag{221}$$

$$-(\omega_+^2 \vec{r}_+ + \omega_-^2 \vec{r}_-) = -\frac{q}{m}|\vec{\omega}_+||\vec{B}|\vec{r}_+ + \frac{q}{m}|\vec{\omega}_-||\vec{B}|\vec{r}_- - \frac{q}{m} E_0(\vec{r}_+ + \vec{r}_-), \tag{222}$$

$$-(\omega_+^2 \vec{r}_+ + \omega_-^2 \vec{r}_-) = -\omega_+\omega_c \vec{r}_+ + |\omega_-|\omega_c \vec{r}_- - \omega_b^2(\vec{r}_+ + \vec{r}_-), \tag{223}$$

$$\vec{r}_+(\omega_+^2 - \omega_+\omega_c - \omega_b^2) + \vec{r}_-(\omega_-^2 + |\omega_-|\omega_c - \omega_b^2) = 0. \tag{224}$$

The last equation holds true because the coefficients of $\vec{r}_+$ and $\vec{r}_-$ are equal to zero, i.e.

$$\omega_+^2 - \omega_+\omega_c - \omega_b^2 = \omega_+(\omega_+ - \omega_c) - \omega_b^2 = 0, \tag{225}$$

which means

$$\left(\frac{\omega_c}{2} + \sqrt{\left(\frac{\omega_c}{2}\right)^2 + \omega_b^2}\right)\left(-\frac{\omega_c}{2} + \sqrt{\left(\frac{\omega_c}{2}\right)^2 + \omega_b^2}\right) - \omega_b^2 = 0, \tag{226}$$

$$-\left(\frac{\omega_c}{2}\right)^2+\left(\left(\frac{\omega_c}{2}\right)^2+\omega_b^2\right)-\omega_b^2=0, \tag{227}$$

and

$$\omega_-^2+|\omega_-|\omega_c-\omega_b^2=|\omega_-|(|\omega_-|+\omega_c)-\omega_b^2=0, \tag{228}$$

which means

$$\left(-\frac{\omega_c}{2}+\sqrt{\left(\frac{\omega_c}{2}\right)^2+\omega_b^2}\right)\left(+\frac{\omega_c}{2}+\sqrt{\left(\frac{\omega_c}{2}\right)^2+\omega_b^2}\right)-\omega_b^2=0, \tag{229}$$

$$-\left(\frac{\omega_c}{2}\right)^2+\left(\left(\frac{\omega_c}{2}\right)^2+\omega_b^2\right)-\omega_b^2=0. \tag{230}$$

### 23.3 Longitudinal motion of trapped ions in solenoids

Finally, the solution of the longitudinal equation of motion (207) yields the third independent motion in $z$-direction. The longitudinal electric field $E_z$ is due to longitudinal variations of the antiproton beam potential $U(s)$. It depends on the longitudinal variations of the beam envelopes and the beam pipe radius (see Sect. 5). The longitudinal electric field yields an unidirectional acceleration of the trapped ions out of the solenoid if the potential minima are located outside of the solenoids. If the electric field component $E_z$ equals to zero the ions move with their constant thermal velocity in the longitudinal direction. An especially dangerous situation occurs if a potential minimum occurs inside a solenoid. Then, the ions start to oscillate longitudinally about the potential minimum. They are trapped radially as well as longitudinally as in a Penning trap. Without clearing the beam is locally neutralized within a very short time.

### 23.4 Magnetron motion and modified cyclotron motion of electrons in solenoids

Now, we discuss the magnetron motion and the modified cyclotron motion of electrons in solenoids which is due to the superposition of a radial electric field $\vec{E}$ and a longitudinal magnetic field $\vec{B}$. The charge $q$ of electrons is negative,

$$q=-|q|. \tag{231}$$

The resulting radial acceleration by the electric field $\vec{E}$ of the antiproton beam is directed radially off the central axis. In addition the angular velocity $\vec{\omega_c}$ of the cyclotron motion is also directed in the opposite direction, i.e. in the direction of the magnetic field $\vec{B}$. The angular frequency of the free cyclotron motion (i.e. for $\vec{E}_\rho=0$) is given by

$$\omega_c=\frac{|q|B}{m}. \tag{232}$$

The parameter $\omega_b$ takes the electric field strength in the following equations into account,

$$\omega_b=\sqrt{\frac{|q|E_0}{m}}. \tag{233}$$

Before going into the details we anticipate that the angular velocities $\vec{\omega}_+$ and $\vec{\omega}_-$ of the modified cyclotron and magnetron motions are directed in the same direction, i.e. both are directed in the direction of the magnetic field $\vec{B}$.

As before, the radial equation of motion (206) can be solved using the ansatz (212)-(214) and the radial motion is characterized by two independent motional modes: (i) the modified cyclotron motion with angular frequency $\omega_+$ and radius $r_+$ and (ii) the magnetron motion with angular frequency $\omega_-$ and radius $r_-$. Inserting the ansatz (212) into (206) yields

$$\omega_+ = \frac{\omega_c}{2} + \sqrt{\left(\frac{\omega_c}{2}\right)^2 - \omega_b^2}, \tag{234}$$

$$\omega_- = \frac{\omega_c}{2} - \sqrt{\left(\frac{\omega_c}{2}\right)^2 - \omega_b^2}. \tag{235}$$

The subtle distinction of this solution is the fact that a minus sign appears in the expression under the square root. The proof that the equations (212)-(214) with (234) and (235) represent the solution of the equation of motion (206) for particles with negative charge $q = -|q|$ goes as before.

**ACKNOWLEDGEMENTS**

I would like to thank Alexander Gruber, Andreas Lehrach, Jürgen Dietrich, Wolfgang Hillert, Bernd Lorentz, Rudolf Maier, Alain Poncet, Dieter Prasuhn, Rolf Stassen, Hans Stockhorst and Raimund Tölle for helpful informations and discussions.

## References


[1] FAIR Baseline Technical Report 2006 (FBTR 2006) GSI Darmstadt, March 2006, see http://www.fair-center.de/fileadmin/fair/publications_FAIR/FAIR_BTR_6.pdf.

[2] Design Work For the High-Energy Storage Ring of the Future GSI Project, A. Lehrach et al., Proceedings of 2005 Particle Accelerator Conference, Knoxville, Tennessee (USA) (2005).

[3] Strong Interaction Studies with Antiprotons, Letter of Intent, PANDA Collaboration, January 2004, see FAIR Baseline Technical Report 2006 (FBTR 2006), http://www.fair-center.de/fileadmin/fair/publications_FAIR/FAIR_BTR_6.pdf.

[4] Antiproton-Proton Scattering Experiments with Polarization, Letter of Intent, PAX Collaboration, January 2004, see FAIR Baseline Technical Report 2006 (FBTR 2006), http://www.fair-center.de/fileadmin/fair/publications_FAIR/FAIR_BTR_6.pdf.

[5] F. Rathmann et al., A Method to Polarize Stored Antiprotons to a High Degree, Phys. Rev. Lett. **94** (2005) 014801.

[6] A Study of Spin-dependent Interactions with Antiprotons, Letter of Intent, ASSIA Collaboration, January 2004, see FAIR Baseline Technical Report 2006 (FBTR 2006), http://www.fair-center.de/fileadmin/fair/publications_FAIR/FAIR_BTR_6.pdf.

[7] P. Zenkevich, O. Boine-Frankenheim and P. Alexeev, Trapped Particle Effects in the HESR Storage Ring, GSI-Acc-Note-2006-03-004 (2006).

[8] P. Zenkevich, Inter-Species Effects in the HESR, Internal HESR Note (2009).

[9] D.G. Koshkarev and P.R. Zenkevich, Resonance of Coupled Transverse Oscillations in Two Circular Beams, Particle Accelerators **3** (1972) 1.

[10] L.J. Laslett, A.M. Sessler and D. Möhl, Nucl. Instr. and Meth. **121** (1974) 517.

[11] E. Keil and B. Zotter, CERN-ISR-TH/79-58 (1979).

[12] Y. Baconnier, Neutralization of Accelerator Beams by Ionization of the Residual Gas, CERN Accelerator School, Gif-sur-Yvette, Paris, 1984, CERN 85-19 (1985).

[13] R. Alves-Pires et al., On the Theory of Coherent Instabilities Due to Coupling a Dense Cooled Beam and Charged Particles from the Residual Gas, Particle Accelerator Conference Chicago 1989, IEEE (1989), CERN/PS/89-14 (AR) (1989).

[14] A. Poncet, Ions and Neutralization, in Frontiers of Particle Beams: Intensity Limits, eds. M. Dienes, M. Month, S. Turner, Springer Verlag LNP, p. 488 (1990).

[15] A. Poncet, Ions Trapping and Clearing, CERN/US CAS (1992), CERN MT/93-01

[16] P. Zhou, A Study of Ion Trapping and Instability in the FERMILAB Antiproton Accumulator, PhD Thesis, Northwestern University (1993).

[17] Y. Baconnier, A. Poncet, and P.F. Tavares, Neutralization of Accelerator Beams by Ionisation of the Residual Gas, CAS Proc. CERN 94-01, p.525 (1994).

[18] A. Poncet, Ion Trapping and Clearing, CAS Proc. CERN 95-06, p.859 (1995).

[19] A. Poncet, Ion Trapping, Clearing, Beam-Ion Interactions, CERN Accelerator School CERN99-05, Snekersen, Denmark, 165 (1999).

[20] D. Neuffer and K.Y. Ng, Thoughts on Ion Trapping Instability in the Recycler, Fermilab Report FERMILAB-TM-2256 (2004).

[21] HESR List of Technical Parameters, compiled by K. Bongardt and R. Tölle, Status July 2011, Internal HESR Homepage, http://www2.fz-juelich.de/ikp//hesr/HesrTechnicalParameters_20110715_approved.pdf (2009), R. Tölle, private communication (e-mail: r.toelle@fz-juelich.de).

[22] A. Gruber: Development of the cluster-jet target and the interaction region of the PANDA detector; Dr.-Thesis, Universität Wien, to be published.

[23] A. Khoukaz, H. Orth, M. Büscher, P. Fedorets, H. Calen, A. Gruber, J. Zmeskal, D. Prasuhn, A. Lehrach, A. Bersani: Technical Design Report for the PANDA Internal Targets: The Cluster-Jet Target and Developments for the Pellet Target, to be published.

[24] A. Poncet, private communication (2010).

[25] J.D. Jackson, Classical Electrodynamics, 2nd edition, Sections 12.4 and 12.5, John Wiley & Sons, New York (1975).

[26] R. Macek and M. Pivi, ExB Drift of the e-cloud in a PSR Quadrupole and Dipole, Technical Note of 3/28/05 posted to the ILC website: http://www-project.slac.stanford.edu/ilc/testfac/ecloud/files/ExB_Drift_of_e-cloud_PSRquad_dipole_v9c.pdf.

[27] P.F. Tavares, Transverse Distribution of Ions Trapped in an Electron Beam, CERN-PS/92-55 (LP) (1992).

[28] A.W. Hull, The Effect of a Uniform Magnetic Field on the Motion of Electrons between Coaxial Cylinders, Phys. Rev. **18** (1921) 31.

[29] F.M. Penning, Physica (Utrecht) **3** (1936) 873.

[30] L.S. Brown and G. Gabrielse, Rev. Mod. Phys. **58** (1986) 233.

[31] K. Blaum, Phys. Rep. **425** (2006) 1.

[32] Technical Design Report for the PANDA Solenoid and Dipole Spectrometer Magnets, The PANDA Collaboration, http://arxiv.org/pdf/0907.0169v1 (2009).

[33] Rudolf Maier, private communication (2011).

[34] HESR-EC Group at Uppsala University, HESR Electron Cooler Design Study, Final Report (2009), see http://www5.tsl.uu.se/hesr/.

[35] Lionel Prost, private communication (2010).

[36] F. Pedersen and A. Poncet, Proton-antiproton instability in the CERN AA, CERN PS/AA/ME Note 81 (1981).

[37] V. Kamerdzhiev, Untersuchung und Verbesserung des Stabilitätsverhaltens eines intensiven elektronengekühlten Teilchenstrahls in COSY, Berichte des Forschungszentrums Jülich 4114, ISSN 0944-2952, Institut für Kernphysik, Jül-4114, D290 (Diss. Dortmund Univ. 2003), e-mail: zb-publikation@fz-juelich.de.

[38] Dieter Prasuhn, private communication (2011).

[39] S.J. Werkema, Control of Trapped Ion Instabilities in the Fermilab Antiproton Accumulator, 16th IEEE Part. Acc. Conf. and Int. Conf. on High-Energy Accelerators, 3397 (1996).

Jül-4343
Oktober 2011
ISSN 0944-2952